Highly-accelerated Diffusion Magnetic Resonance Imaging at Ultrahigh Field

Thesis

for the degree of

doctor rerum naturalium (Dr. rer. nat.)

approved by the Faculty of Natural Sciences of Otto von Guericke University Magdeburg

by M.Sc. Yi-Hang Tung

born on 21 November 1985 in Taichung, Taiwan

Examiner: Prof. Dr. rer. nat. habil. Oliver Speck
Prof. Dr. rer. nat. Matthias Günther

submitted on: 25 March 2024 defended on: 08 October 2024

Abstract

Nuclear magnetic resonance (NMR) has established itself as an accurate and precise tool for measuring molecule self-diffusion and is used in various areas. Significant advances have been made in biology, medicine, and especially neuroscience using diffusion magnetic resonance imaging (dMRI), which enables non-invasive research into the microstructure of the brain. In order to further advance progress, it is necessary to continually improve imaging through higher spatiotemporal resolution and higher diffusion weighting via higher diffusion b-values.

Previous studies have shown that signal enhancement from higher main magnetic field strengths, particularly at ultrahigh fields ($\geq$ 7 Tesla), provides significant benefits in various MRI modalities. Despite these advantages, ultrahigh field strengths pose particular challenges for dMRI. A significant obstacle is the exacerbation of image distortion caused by off-resonance effects, particularly susceptible in fast MRI pulse sequences such as echo planar imaging (EPI). Therefore, there is an urgent need to improve the image fidelity in ultrahigh field dMRI while maintaining the imaging speed and signal-to-noise ratio (SNR) advantage.

This thesis develops a novel rapid pulse sequence that addresses the distortion of EPI while maintaining the SNR advantage for dMRI at the ultrahigh field by combining two EPI variants. These are (i) point-spread function mapping (PSF-EPI) and (ii) view-angle tilting (VAT-EPI). The PSF-EPI has high imaging fidelity but is very time-consuming as a multi-shot approach, while the single-shot VAT-EPI can correct the distortions but has strong image blurring. The merged sequence, VAT-PSF-EPI, accelerates PSF-EPI by four times in correcting distortions caused by brain-air susceptibility differences and fourteen times in eliminating distortion caused by adipose chemical shift. In addition, the eddy current distortion caused by the fast-switching diffusion gradient can be corrected up to b = 3000 s/mm^2 while effectively compensating for the image blur caused by the VAT gradient. VAT-PSF-EPI is the only EPI variant that can simultaneously correct these aberrations in ultrahigh field dMRI. These results are confirmed by theoretical derivation and experimental validation. During the doctorate, two emerging limitations, signal reduction and faint fat artifacts, were successfully addressed, allowing signal recovery while suppressing artifacts. The study demonstrates rapid imaging of VAT-PSF-EPI with 1.4 mm^3 resolution in 15 seconds (5 shots, total acceleration factor 170) and even higher isotropic resolution (1.17 mm^3), as well as dMRI measurements with a very high in-plane resolution (0.7 mm) on a 7-T whole-body human scanner. VAT-PSF-EPI offers a new horizon in ultrahigh field dMRI, a fast and high fidelity imaging without exhausted calibration, modeling, or post-processing computations.

Zusammenfassung

Die Kernspinresonanz (NMR) hat sich als genaues und präzises Werkzeug zur Messung der Selbstdiffusion etabliert und findet in verschiedenen Bereichen Anwendung. In der Biologie, Medizin und insbesondere in den Neurowissenschaften wurden mittels der Diffusions-Magnetresonanztomographie (dMRT) erhebliche Fortschritte erzielt, was die eine nicht-invasive Erforschung der Mikrostruktur des Gehirns ermöglicht. Um den Fortschritt weiter voranzutreiben, ist es notwendig, die Bildgebung durch höhere räumlich-zeitliche Auflösung und höhere Diffusionsgewichtung stetig zu verbessern.

Frühere Studien haben gezeigt, dass eine Signalverstärkung durch höhere Hauptmagnetfelder, insbesondere bei ultrahohen Feldern ($\geq$ 7 Tesla), erhebliche Vorteile bei verschiedenen MRT-Modalitäten bietet. Die effektive Nutzung dieser Vorteile in der dMRT birgt jedoch bei ultrahohen Feldstärken besondere Herausforderungen. Darüber hinaus besteht ein erhebliches Hindernis in der Verschärfung der Bildverzerrung durch Off-Resonanz-Effekte, vornehmlich bei schnellen MRT-Pulssequenzen, wie in der Echo-Planar-Bildgebung (EPI) anfällig sind. Es besteht ein dringender Bedarf, die Bildtreue bei der Ultrahochfeld-dMRT zu verbessern und gleichzeitig die Vorteile der Bildgeschwindigkeit und des Signal-Rausch-Verhältnisses (SNR) beizubehalten.

Diese Doktorarbeit entwickelt eine neuartige schnelle Pulssequenz, die sich mit der Verzerrung von EPI befasst und gleichzeitig den SNR-Vorteil für dMRT auf einem Ultrahochfeld durch die Kombination zweier EPI-Varianten beibehält. Dabei handelt es sich um das Point-Spread-Function-Mapping (PSF-EPI) und das View-Angle Tilting (VAT-EPI). Das PSF-EPI hat eine hohe Abbildungsgenauigkeit, ist aber als Multi-Shot-Methode sehr zeitaufwändig, während das Single-Shot-VAT-EPI die massiven Verzerrungen korrigieren kann, aber eine starke Bildunschärfe aufweist. Die fusionierte Sequenz, VAT-PSF-EPI, beschleunigt PSF-EPI um ein Vierfaches bei der Korrektur starker, durch die Suszeptibilitätsunterschiede im Gehirn verursachter Verzerrungen und um das Vierzehnfache bei der Beseitigung der Verzerrung durch die chemische Verschiebung des Fettgewebes. Darüber hinaus kann die durch den schnell schaltenden Diffusionsgradienten verursachte Wirbelstromverzerrungen bis zu b = 3000 s/mm^2 korrigiert und gleichzeitig die starke Bildunschärfe, die durch den VAT-Gradienten verursacht wird, effektiv kompensiert werden. VAT-PSF-EPI ist die einzige EPI-Sequenz, welche die simultane Korrektur dieser Abbildungsfehler bei Ultrahochfeld-dMRT bewerkstelligen kann. Diese Ergebnisse sind durch theoretische Herleitung und experimentelle Validierung bestätigt. Im Laufe der Promotion konnten zwei auftretende Einschränkungen, Signalreduzierung und schwache Fettartefakte, erfolgreich behandelt werden, was die Signalwiederherstellung bei gleichzeitiger Unterdrückung von Artefakten ermöglicht. Die Studie belegt eine schnelle Bildgebung von VAT-PSF-EPI mit 1,4 mm^3 Auflösung in 15 Sekunden (5 Aufnahmen, Gesamtbeschleunigungsfaktor 170), und noch höherer isotroper Auflösung (1,17 mm^3), sowie dMRT-Messungen mit einer

sehr hohen Flächenauflösung (0,7 mm) bei einem 7-T-Ganzkörperscanner. VAT-PSF-EPI bietet neue Horizonte in der Ultrahochfeld-dMRT, eine schnelle und hohe Bildtreue ohne erschöpfende Kalibrierung, Modellierung und Nachbearbeitungsberechnungen.

Contents

List of Figures

List of Tables

1 Introduction

1.1 Motivation

Diffusion magnetic resonance imaging (dMRI) has garnered significant attention for clinical diagnosis and neuroscience research, particularly in exploring brain microstructures. This interest is primarily attributed to the non-invasive nature of MRI, which excels in soft tissue contrast and comprehensive scan coverage. However, pursuing high spatiotemporal resolution and elevated diffusion b-values in dMRI often results in prolonged scan times and heightened susceptibility to image artifacts, such as distortion in the echo planar image (EPI) sequence. Despite numerous proposed correction methods for EPI distortions, none have successfully addressed the triad of primary distortion sources in dMRI: static off-resonance effects of susceptibility difference and chemical shift and dynamic off-resonance effects of eddy current from fast switching diffusion gradients.

Ultrahigh field MRI, owing to its enhanced signal, presents advantages in many imaging modalities. However, dMRI utilization at ultrahigh fields has been limited due to inherent drawbacks, including the need for extended echo times (TE), leading to signal-to-noise ratio (SNR) loss, heightened static off-resonance effects to main field inhomogeneity, radio-frequency (RF) inhomogeneity, and elevated energy deposition. These challenges have been substantial enough to prompt physicians and researchers to consider scanning other types of images at ultrahigh fields and relocating subjects to lower fields for dMRI. This thesis aims to meticulously investigate and address the significant obstacle of image distortion in EPI, ultimately proposing a novel dMRI sequence to overcome one of the primary challenges of ultrahigh field MRI.

1.2 Purpose

A significant challenge in ultrahigh field diffusion imaging is image distortions, particularly within the EPI sequences. Two sequences that have demonstrated their efficacy in correcting EPI distortions, namely point-spread function mapping (PSF-EPI) in the multishot approach and single-shot view-angle tilting (VAT-EPI), have been of considerable interest. Utilizing a multi-shot approach in PSF-EPI instead of a single-shot multireference approach allows for correcting dynamical eddy current distortion and static susceptibility distortion in each multishift scan. In VAT-EPI, it was evidenced to correct the static susceptibility and chemical shift. However, both approaches have proven less practical, particularly in ultrahigh fields, due to the time-intensive nature of PSF-EPI and the pronounced

image blurring associated with VAT-EPI. The amalgamation of these sequences into VAT-PSF-EPI is anticipated to capitalize on distortion correction capabilities while surpassing the speed limitations of PSF-EPI and mitigating the image-blurring issues inherent in VAT-EPI.

1.3 Organization of the Thesis

The thesis initiates its exploration by delving into the paramount factor in MRI, namely the origination of SNR. Subsequently, the SNR sweet spot at ultrahigh field strengths is comprehensively examined, drawing upon theoretical considerations and empirical values gleaned from existing literature. Following this, a detailed exposition of three potential off-resonance contributors to image distortion in diffusion MRI is presented without the link to the image aberrations yet: susceptibility, chemical shift, and eddy current effects. The subsequent section outlines the two most prevalent sequences employed in dMRI: a literature review of turbo spin echo sequences (TSE) and an exploration of EPI with a specific focus on its sensitivity to the off-resonance. After that, the EPI distortions induced by the mentioned off-resonance sources are simulated, and the corresponding established strategies to address the EPI distortion and the limitations of these methods are described. At the end of this chapter, the mathematical formulations of two sequences crucial for constructing the proposed sequence—PSF-EPI and VAT-EPI—are then explicated, emphasizing their distortion correction properties and why they are said to be impractical at ultrahigh field.

In the primary context of the study, the theory behind the fused VAT-PSF-EPI sequence is first established. Several meticulously designed experiments are conducted to evaluate the sequence's properties, including its efficacy in distortion correction, sequence acceleration, and SNR change. Two prevalent limitations of signal reduction and artifact appearance observed in VAT-PSF-EPI that require mitigation are investigated, along with the corresponding improvements. The study scrutinizes *in vivo* human fast and high-resolution diffusion images and implements above enhancements on a whole-body 7 T scanner. Finally, the thesis concludes with a synthesis of findings and an outlook for future research endeavors.

2 Background

2.1 SNR at Ultrahigh Field

When developing an NMR sequence, signal-to-noise ratio (SNR) is one of the most critical considerations. It is known that ultrahigh field MR imaging is more beneficial from its high SNR than the lower fields. However, the SNR benefits only in certain circumstances. Below is a summary of the physics and MR parameters influencing the field strength B_0. In order to describe SNR dependency with B_0, the MR signal mechanism must be briefly described. The SNR contribution is defined separately from the contribution of magnetization, RF coil, and relaxation.

2.1.1 Magnetization

For the contribution of signal, a spin 1/2 nuclei (e.g., 1H) allowed quantitated spin states are S = ± 1/2. Without an external static field (B_0), there is no spin excess, which means the number of spin-ups (S = +1/2) and downs (S = -1/2) are roughly equal. These spins orientate randomly, and the energy of both spin states is the degenerated energy level.

When a homogenous external field B_0 is exerted on the object, the spins within the object are separated into parallel and anti-parallel, corresponding to spin-up and spin-down states. The number of low-energy state spins is slightly more than the high-energy state spins in the equilibrium, which is known as spin excess. The Zeeman effect can describe the energy difference between two states as

$$\Delta E = \hbar\omega_0 = r\hbar B_0. \tag{2.1}$$

With the appearance of B_0 field, the measuring object's spin density and the nuclear magnetic moment remain the same. Nevertheless, the spin excess is linearly dependent on the resonant frequency (ω_0) when the quantized photon energy is much less than the environmental thermal energy (e.g., at room temperature). The bulk magnetization of spins in the equilibrium under the limit of magnetic moment energy is much smaller than the thermal energy ($E_m = \mu B \ll kT$), which can be written as [1]

$$M_0 \approx \rho_0 B_0 \mu^2/3kT = \rho_0 B_0[g^2\mu_B^2 J(J+1)]/3kT = C B_0/T, \tag{2.2}$$

where ρ_0 is the spin number density, g is the g-factor, μ_B is the Bohr magneton, J is the total angular momentum quantum number (J = S + L, S is the spin angular momentum

quantum number and L is the orbital angular momentum quantum number), and C is the Curie constant for paramagnetism. The approximation of the Curie regime or small polarizations is valid for the common liquid state NMR (μB « kT $\approx 6.6 \times 10^{-6}$ B_0). Both quantum and classic theories give the same M_0 prediction in such a regime. Consider the nucleus of spin 1/2 (e.g., 1H) and neglecting the orbital motion, the equilibrium magnetization is [2]

$$M_0 = \rho_0 B_0 r^2 \hbar^2 / 4kT = (\rho_0 B_0 r\hbar/2kT)(r\hbar/2) = (\rho_0 \hbar\omega_0/2kT)(g\mu_N/2), \tag{2.3}$$

where γ is the gyromagnetic ratio and $\gamma n/2\pi = gn\mu_N/\hbar$. The latter expression is spin excess multiplied by the magnetic moment. The proton magnetic moment is 2.793 μ_N, so the spin excess is roughly 3.3 out of 1 million spins at 1 Tesla. Note that in the spin excess term, the static field dependency can be alternatively written to Larmor (angular) frequency ω_0, i.e., $\omega_0 = \gamma B_0$.

2.1.2 RF Coil

From the above expression, the intrinsic signal of an object in a homogeneously static field B_0 is described by the magnetization M_0. Whenever a small magnetic field (RF field) perturbs the system with Larmor frequency, the M_0 is tipped and precess to the B_0. During the precession, spins tend to be at a low energy state by releasing the energy and returning to the thermal equilibrium. Since the RF signal transmits and receives the object through an RF coil, the NMR SNR is expected to depend highly on the coil. Assuming the RF energy is deposited to the object homogeneously, the SNR can be written as [3, 4]

$$\mathrm{SNR_{coil}} = M_0(\omega_0^2 V_s^2 \beta_1^2 / 4kT\Omega_{\mathrm{eff}} \mathrm{BW_r})^{1/2}, \tag{2.4}$$

where V_s is the sample volume, β_1 is the receiving coil sensitivity, T is the temperature of an object, R_{eff} is the effective resistance, and BW_r is the receiving bandwidth. The numerator and denominator are the signal and noise voltage the coil detects. Specifically, the denominator is the Johnson–Nyquist equation describing the white noise (thermal noise), which is proportional to the environmental temperature. The effective resistance is from the sources of electronics, coils, and the object and can be written as [5]

$$\Omega_{\mathrm{eff}} = (\Omega_{\mathrm{electronics}} + \Omega_{\mathrm{coils}}) + \Omega_{\mathrm{object}} = A\omega_0^{1/2} + C\omega_0^2\beta_1^2, \tag{2.5}$$

where A and C are the measured constants. Because M_0 has a linear B_0 dependent, SNR has roughly the field dependent of B_0 to 7/4 in the relatively low field and linear to the high fields.

A recent study with experiments including 1H MRI at 3 T, 7 T, and 9.4 T human scanners observed a ${\omega_0}^{1.65}$ relationship of SNR [6]. The result may be explained by the

conductivity and electric field generated by the human subject detected (by the coils) having a volume depth with B_0 dependency [7]. It says the object's center has the lowest resistance and highest resistance occurs at the surface. Thus, the SNR increases almost linear with B_0 at the skin and roughly quadratically with B_0 at the center in a human head MR measurement.

2.1.3 Relaxation

Another MR signal mechanism that has a B_0 field dependency is relaxation. Bulk magnetization is parallel to the external main static field in the thermal equilibrium. After the nutation of RF, the parallel component decreases, and the coherent transversal component increases. The former tends to return to the thermal equilibrium, called the longitudinal relaxation, and the latter tends to lose its coherence, called the transversal relaxation. Thus, both components are times-evolved. Bloch modeled the signal relaxation exponentially, where T_1 is used to character the longitudinal relaxation of 63 % of the full signal return, while T_2 is the signal decay to the 37 % of the full signal of the transversal relaxation [1]. The general expression of relaxation with $\pi/2$ excitation RF pulse at TE is

$$M(TE) = M_0(1 - e^{-TR/T_1})e^{-TE/T_2}. \tag{2.6}$$

The mechanism of relaxation is explainable mainly by the dipole-dipole interaction of molecules. The classic explanation for the pure substance is based on the molecule tumbling by the Bloembergen-Purcell-Pound (BPP) theory [8]. Later, the theory was extended to the heteronuclear system, and the paramagnetism system contains electrons or ions, which is the Solomon-Bloembergen-Morgan (SBM) theory [9, 10]. These theories described the signal relaxation as related to the molecule tumbling and characterized by the tumbling frequency ω or the inverse of correction time τ_c. Note that $\omega_t \tau_c = 1$.

In theory, T_1 is the shortest when the tumbling frequency is close to the Larmor frequency, in which the tumbling frequency corresponds to the rotational frequency of molecules. In this situation, longitudinal relaxation is the most effective method. The tumbling frequency of molecules is roughly inverse of their size. Therefore, from the fast to medium tumbling, T_2 changes accompany the T_1. However, the medium to slow tumbling decreases T_2 and is unrelated to the increased T_1. In this case, molecules are tumbling too slowly and do not dispatch the energy effectively to the environment. Since the field fluctuation induced by one dipole is slow enough to become quasi-static, another dipole experiences a different Larmor frequency, and transversal magnetization loses coherence. The phenomenon can be predicted by both quantum theory and its approximation, classic theory.

The molecule tumbling theories predict that the T_1 has field dependency, while the T_2 is generally independent of the field [11, 12]. Figure 2.1 simulates the B_0 dependency of T_1

and T_2 from the SBM theory. It can be seen that the T_1 increases with the field in the human scanner range, especially for the fast to medium tumbling molecules. At the same time, T_2 increases slightly for the medium-tumbling molecules. However, experimental data observed that the T_2 decreases sharply at the ultrahigh field, which is markedly distinct from the theory [13]. The most believed explanation is that the susceptibility increases with the field strength, and the microscopic field deviation leads the diffusion and chemical exchange effects [14, 15]. Thus, the "apparent" T_2 is reduced to the ultrahigh field. Furthermore, the T_1's field dependency on biological tissues is generally less than the asymptotes of theoretical $B_0{}^2$, which is explained by the structure mixture, thus the mixed thumbing rate [16, 17]. The rough estimate of the T_1 filed dependency is B_0 to 0.4 [5, 18, 19].

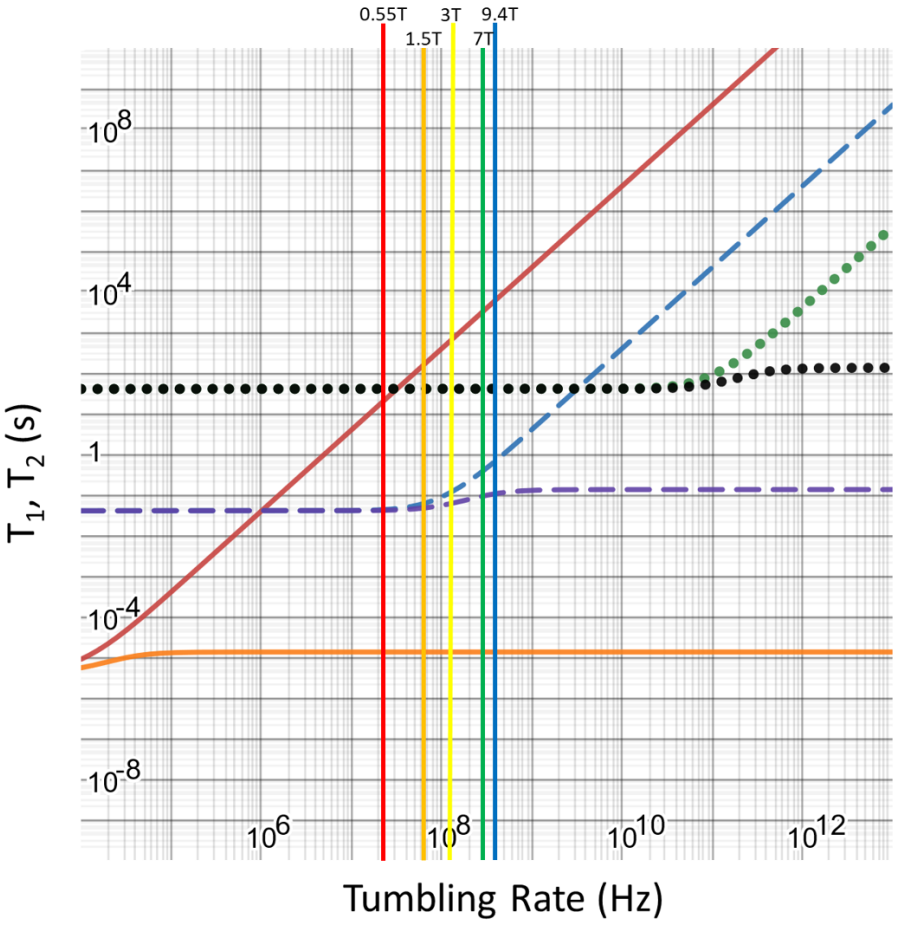

Figure 2.1: Prediction of relaxation time constants in BPP theory. The log-log plot illustrates the relationship between the relaxation time constants (T_1 and T_2) and thumbing rate. Vertical lines are the field strengths of human MRI scanners. Dark red, dark blue, dark green: T_1 relaxation time constants. Dark orange, dark purple, dark blue: T_2 relaxation time constants. Solid lines: τ_c $=10^{-5}$ (solids), Dashed lines: $\tau_c = 10^{-9}$ (viscous fluids), Rounded dot lines: τ_c $= 10^{-12}$ (liquids).

The relations of SNR to B_0 are simulated in Figure 2.2. In Figure 2.2A, B_0 to 1.65 and linear relation are plotted without considering other factors. The SNR gain at ultrahigh fields is significant; the SNR ratio of ${B_0}^{1.65}$ to linear is roughly 1.3 at 1.5 T, 3.5 at 7 T, and 5.7 at 14 T. The Figure 2.2B and 2.2C are the T_1 and T_2 time constants to the B_0 of the *in vivo* human brain tissues from the literature [20, 21]. Specifically, the T_1 of gray matter and white matter are increasing with increasing the B_0, as predicted in the BPP theory. The gray matter is ${B_0}^{0.45}$, and the white matter is ${B_0}^{0.35}$ for the power-law fitting (not shown). At the same time, the T_2 change is not apparent from 0.55 T to 3 T but has a sharp decrease from 3 T to 7 T.

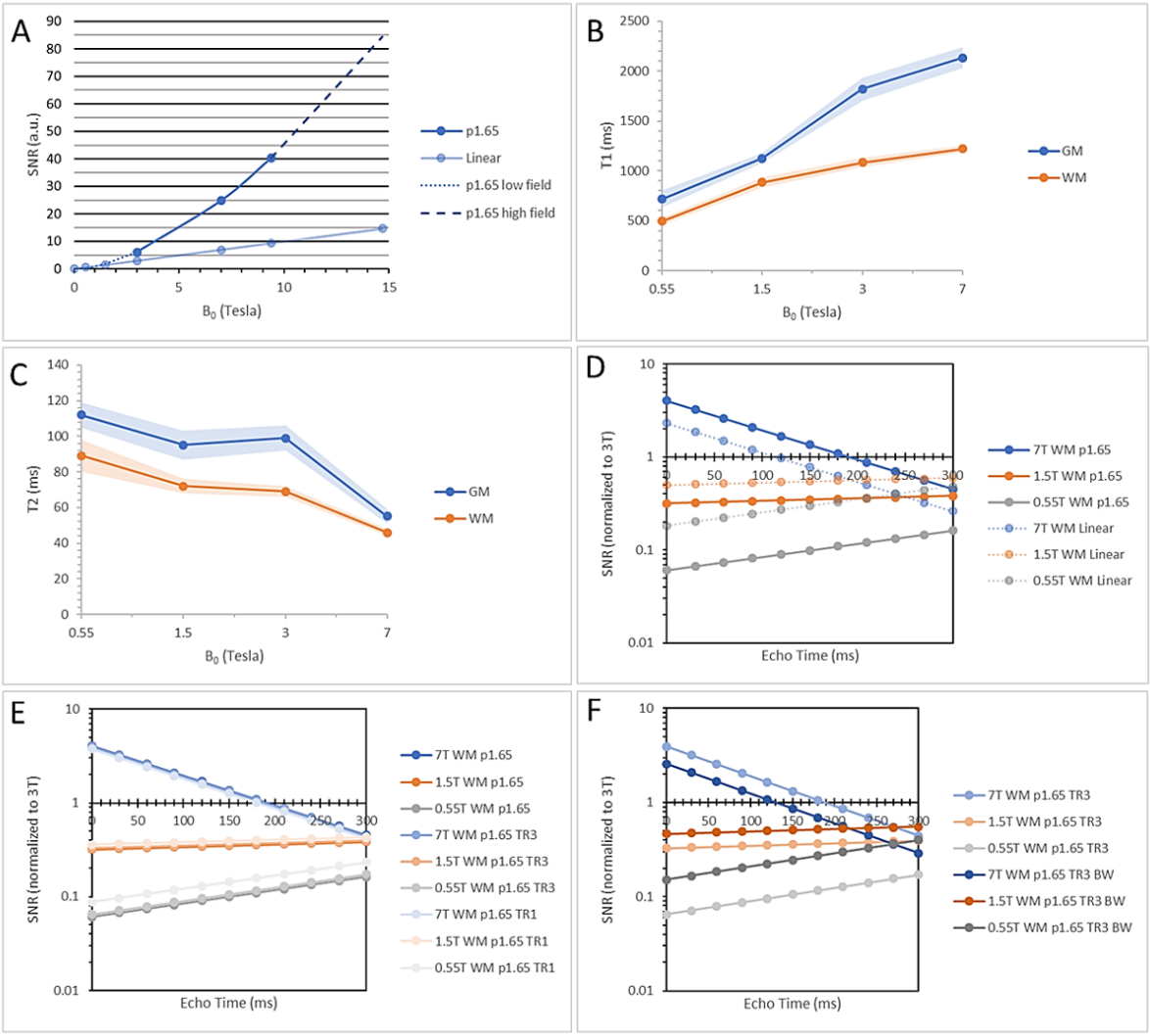

Figure 2.2: SNR change in the typical MRI human scanners with different main magnetic field strengths (B_0). A: SNR change with ${B_0}^{1.65}$ and ${B_0}^{1}$. B, C: T_1 and T_2 time constants of human gray matter (GM) and white matter (WM) change with B_0. D: WM SNR dependency with TE in ${B_0}^{1.65}$ and ${B_0}^{1}$ with different B_0. E: As D and with different TR. F: WM SNR when mitigating the image distortion by increasing the receiving bandwidth.

The bottom row of Figure 2.2 are plots of the SNR to the TE, in which the SNR is normalized to 3 T. The Figure 2.2D plots the SNR of $B_0{}^{1.65}$ and the linear relation. It can be seen that the SNR to the echo time slope at 7 T is huge, which means that at a long TE, the SNR benefit of the ultrahigh field is discarded. As an extreme example of the linear B_0, SNR at 7 T is the same as 3 T when the TE is 120 ms, the same as 1.5 T when the TE is 190 ms, and the same as 0.55 T when the TE is 240 ms. The Figure 2.2E plotted the SNR of different repetition times (TR) of white matter. The TR is defined as the time duration between RF nutation (excitation). The SNR difference from 7 T to 1.5 T is insignificant, with the range of infinite TR to 1.0 sec. In contrast, the short TR has a more significant difference at 0.55 T. Figure 2.2F shows the SNR accounting for the image distortion normalized by the receiving bandwidth. It can be seen that the SNR benefit at 7 T is further shifting to a short TE and is opposite at 0.55 T and 1.5 T.

2.2 Off-resonance Effects

So far, the SNR was described on the on-resonance condition, which means the main magnetic field (B_0 field) and RF perturbed field (B_1 field) are homogeneous, and the spins precess exactly at the Larmor frequency. In other words, there is no field deviation from any other sources. However, field inhomogeneity can happen and lead to signal loss or image artifacts in MRI in reality. The collection of sources that generate field deviation is called off-resonance effects. The following sections describe generally a few of the primary off-resonance effects, which are the major limitations of the fast imaging sequences in MRI. The exact effects of the sequence experiencing the off-resonance effects will be described in Section 2.3.

2.2.1 Chemical Shift

The atomic proton with an unpaired electron (1H, protium) is usually used to describe a simple NMR signal model of a spin 1/2 system. However, most samples or tissues of human MRI contain water molecules (H_2O), which the proton Larmor frequency differs from the protium. It is attributed to the proton in water having a locally higher electron density than in protium. In the molecule, the electron density is related to its chemical structures. The electron surrounding the nucleus is induced by a local magnetic field opposite the external field. This diamagnetism mechanism increases with the nuclear charge number, so it does not change much when the same resonant nucleus is used. The overall magnetic field that the proton experiences is lower than the external field and, thus, is shielded. Typically, the higher electron density increases, the more the shielding effect strengthens. The dimensionless shielding factor σ_s describes the shielding effect. Its relation to the local generating field and the measured Larmor frequency (ν') is

$$\begin{aligned} \nu' &= \gamma/2\pi(\mathrm{B}_0 - B_{\mathrm{local}}) \\ &= (\gamma/2\pi)\mathrm{B}_0(1 - \sigma_s h). \end{aligned} \tag{2.7}$$

The difference in the proton shielding factors in protium and water was determined with several higher-order effects corrections, such as hyperfine structure and the contributions from the electron. At room temperature, the shielding factor of the bound proton in water is roughly 25.69×10^{-6} [22, 23]. It is smaller than the free proton (unshielded) in molecular hydrogen. The shielding factor in water has a tiny temperature dependence of 10.36×10^{-9} /°C from 5 to 45 °C [24]. Further, the shielding factors of molecular (even for water) cannot be calculated accurately. Thus, they are usually determined experimentally.

In general, protons from different substituents of a heteronuclear molecule may have various shielding factors. In the case of homonuclear molecules or heteronuclear molecules with highly symmetric chemical structures, a scalar shielding factor can describe the shifting of the magnetic resonance spectrum well. However, the protons in different locations in 3D space can have various shielding. In such cases, the shielding factor is anisotropic and described by a 3×3 tensor σ [25]. In the current study, however, only the isotropic effect (bulk term) is considered, defined by the mean of the diagonal terms of the shielding tensor. This frequency-shifting effect is known as a chemical shift and is usually compared with a reference molecule

$$\delta = \frac{\nu' - \nu_{\mathrm{ref}}}{\nu_{\mathrm{ref}}} \times 10^6 \text{ ppm}. \tag{2.8}$$

So far, the most used reference molecule is TMS (Tetramethylsilane, $\mathrm{Si(CH_3)_4}$), defined as chemical shift 0 ppm [26]. This is due to TMS's strong singlet signal of NMR spectroscopy and highly shielded nature, which hardly interferes with other substituents. The chemical difference between free proton and TMS is 30.34 ppm. Hence, the TMS has roughly 4.65 ppm lower Larmor frequency (or more shielded) than water. Furthermore, most of the organic compound of the proton is within 15 ppm in contrast to TMS.

The above two equations may be combined to form the relationship of magnetic field perturbation

$$\begin{aligned} \Delta\nu_c &= (\gamma/2\pi)\Delta B_c \\ &= (\gamma/2\pi)\mathrm{B}_0(\sigma_{s,\mathrm{ref}} - \sigma'_s) \\ &= \delta\nu_{\mathrm{ref}}, \end{aligned} \tag{2.9}$$

where $\Delta\nu_{\mathrm{c}} = (\nu\text{' - }\nu_{\mathrm{ref}})$ and $\Delta\mathrm{B_c} = (\mathrm{B'} - \mathrm{B_{ref}})$. It can be seen that the field perturbation has the B_0 dependence. In the current study, an important aspect is the amount of field

perturbation caused by the chemical shift of the imaging nucleus relative to the main resonant chemical compound. For example, the lipid molecule has the main peak of $\delta = 1.3$ ppm in the TMS referencing system, and thus 3.35 ppm differs from water.

2.2.2 Susceptibility

The molecules with different chemical structures lead to the field perturbation for the same resonant nucleus, characterized by the chemical shift in the previous section. However, the macroscopic object present in the main static magnetic field also leads to field perturbations. It has not only the dependence on the object's and medium's magnetic susceptibilities but also the shape and orientation dependence. The effect is called bulk magnetic susceptibility (BMS) shift. The BMS shift can be further divided into homogeneous and inhomogeneous parts. The former has a similar effect to the chemical shift, while the latter has the distance dependence. This section describes the field perturbation of the BMS effect in a few simple object geometries.

In general, the macroscopic magnetic flux density of a uniformly magnetized object in an applied field can be described by $\mathrm{B_{macro}}$ as below [27–29]

$$\begin{aligned} \mathrm{B_{macro}} &= \mu \mathrm{H} \\ &= (1+\chi_i)\mathrm{H} \\ &= (1+\chi_i)(\mathrm{H_0} + \mathrm{H_{in}} + \mathrm{H_{dm}}), \end{aligned} \tag{2.10}$$

where μ is the permeability, χ_i is the volume magnetic susceptibility of the object. The magnetic field H is the summation of applied uniform static field $\mathrm{H_0}$, intrinsic field inhomogeneity $\mathrm{H_{in}}$, and overall demagnetizing field $\mathrm{H_{dm}}$. Specifically, the applied uniform field has a linear relation to the magnetic flux density $\mathrm{B_0}$ of the relationship $\mathrm{H_0} = \mathrm{B_0}/\mu_0$, where μ_0 is the magnetic permeability of free space. The intrinsic field inhomogeneity is due to the imperfect shimming and is as tiny as roughly 0.1 ppm [30]. In comparison, the overall demagnetizing field can be divided into the contribution of the object self-contribution and the surrounding medium [31, 32]. Moreover, the demagnetizing field assumes that the magnetization M is collinear and proportional to the magnetic field H for an ellipsoid object

$$\mathrm{H_{dm}} = -\alpha \mathrm{M}, \tag{2.11}$$

The demagnetizing factor α describes an object's shape and orientation dependencies. Its value is between 0 and 1, and the summation of the three spatial components α_x, α_y, and α_z is 1. The simple shapes can be generally approximated using the symmetry of the ellipsoid [33]. For example, if the main magnetic field is in the z-direction, a sphere and a cube which has its $\alpha_\mathrm{x} = \alpha_\mathrm{y} = \alpha_\mathrm{z} = 1/3$, while an infinite cylinder has the long axis in the

z direction is $\alpha_x = \alpha_y = 1/2$, $\alpha_z = 0$, an infinite plate or circular disk with finite thickness with its normal vector parallel to the z is $\alpha_x = \alpha_y = 0$, $\alpha_z = 1$. Nevertheless, the general form of an ellipsoid is not a simple fraction and needs to be calculated numerically.

For an object resting in the structureless medium, the object demagnetizing field is -$\alpha\chi_i$H, while the medium demagnetizing field is (α - 1)χ_oH. By applying B = μ_0(H + M) and neglecting the intrinsic field inhomogeneity, the general expression of the macroscopic magnetic flux density for an ellipsoid of revolution is [23]

$$B_{macro} = B_0(1 + \chi_i)/(1 + \chi_0 + \alpha(\chi_i - \chi_0)). \tag{2.12}$$

It was found that the local field experienced by the nucleus inside the object is quite different from the macroscopic field of the object. The well-accepted modification of the field is by the concept of the sphere of Lorentz [27, 29, 30, 34]. It is an imaginary sphere carving in the object, where all the resonant nuclei are within the sphere surrounded by the free space. The object with the carved-out sphere has the field on its surface of B_L = -2μ_0/3 M = -2χ/3 [35–37]. This field modification is essential, especially when the object has multiple compartments or is immense in the medium with a magnetic susceptibility far from 0 (free space). The local field shift after the Lorentz modification by keeping only the first-order perturbation with χ « 1 is

$$\begin{aligned} B_{nuc} &= (1 - 2\chi/3)B_{macro} \\ &= (1 - 2\chi/3)(1 + \chi)H \\ &\approx (1 - 2\chi/3 + \chi)H \\ &= (1 + \chi/3)H. \end{aligned} \tag{2.13}$$

Note that the magnetic susceptibility in the MR comparable region is in the range of -10 × 10^{-5} to 10 × 10^{-5}, human soft tissues are in the range of -11 × 10^{-6} to -7 × 10^{-6}, and water is -9.05 × 10^{-6}. Hence, assuming the $\chi \ll 1$ to have the first-order approximation is reasonable. The above expression is for both the magnetic flux density of the resonant nucleus experiencing inside and outside objects. However, the exact expression can be solved by assuming the magnetic flux density outside the object is a uniform field plus a dipole field originating at the object's center. Moreover, the boundary conditions are set to the B-field, which is continuous at the pole of an object, and the H-field is continuous at the object's equator. The analytic solutions of the total field in objects with simple geometry are listed in Table 2.1. In the calculation, the common MR convention of the main magnetic field in the z-direction is used [3, 28, 38]. In Table 2.1, a polar coordinate (r, θ) is used for the spherical object, with the angular coordinate as the angle between the applied field and the radius R. The cylindrical object uses the cylindrical coordinate (r, ϕ), and the θ is the angle between the long axis of the cylinder and the applied field

with the radius R. For the disk object, the polar coordinate (r, θ) is used, and the angle θ is between the normal vector of the disk and the applied field.

Table 2.1: The total magnetic field of a homogeneous object with common simple geometries placed in a homogeneous medium.

Total field	**Inside the object**	**Outside the object**
Sphere	B_0 (1 + χ_0/3)	B_0 (1 + χ_0/3 + (χ_i - χ_0)/3·(R/r)^3(3cos$^2\theta$ - 1))
Infinite cylinder	B_0 (1 + χ_0/3 + (χ_i - χ_0)/6·(3cos$^2\theta$ - 1))	B_0 (1 + χ_0/3 + (χ_i - χ_0)/2·(R/r)^{2}sin$^2\theta$(2cos$^2\phi$ - 1))
Infinite disk	B_0 (1 + χ_0/3 - (χ_i - χ_0)/3·(3cos$^2\theta$ - 1))	B_0 (1 + χ_0/3)

Furthermore, the BMS shift can be further distinguished into homogeneous and inhomogeneous parts. The homogenous BMS shift is essential for the chemical shift measurement as a correction [25, 39]. This shift is expressed for the sphere or the "magical angle" (θ = 54.74°) cylinder or disk as below, with the BMS shift inside the object being 0 and outside with the medium of free space

$$\delta_m = (1/3 - \alpha)(\chi_i - \chi_0) \times 10^6 \text{ ppm}. \tag{2.14}$$

For the inhomogeneous parts of BMS shift, it has the distance dependence, e.g., r^3 for a sphere and r^2 for a cylinder. The extreme values of the field perturbation of inhomogeneous BMS ΔB_{0z} can be estimated by a range with respect to the angle between the object and B_0 (θ), in which the maximum values are related parallel ($\theta = 0°$). In contrast, the minimum values are perpendicular to the main magnetic field ($\theta = 90°$).

Table 2.2 summarizes the field perturbation of the simple geometries by separating the homogeneous BMS terms with chemical shift and inhomogeneous BMS terms. It can be seen that magnetic susceptibility contributed to the field shifting, similar to the chemical shift. The extreme values are at the object surfaces for the inhomogeneous BMS shifting. Note that the maximum and minimum shift difference is $\Delta\chi$, with either magnitude less than $\Delta\chi$. Finally, the homogenous and inhomogeneous shifts are proportional to the magnitude of the main field B_0.

Table 2.2: General expressions of off-resonance fields by the chemical field and object shape-dependent susceptibility with the shapes in Table 2.1. Note $\Delta B_z = B_z$ - B_0.

Field perturbation	**Homogeneous shift**	**Inhomogeneous shift**
Sphere	ΔB_z = (-σ + χ_o/3) B_0	(-$\Delta\chi$/3 + χ_o/3) B_0 < ΔB_z < (2$\Delta\chi$/3 + χ_o/3) B_0
Infinite cylinder (∥)	ΔB_z = (-σ + χ_i/3) B_0	0
Infinite cylinder (⊥)	ΔB_z = (-σ - χ_i/6 + χ_o/2) B_0	(-1/2$\Delta\chi$ + χ_o/3) B_0 < ΔB_z < ($\Delta\chi$/2 + χ_o/3) B_0
Infinite disk (∥)	ΔB_z = (-σ - 2χ_i/3 + χ_o/2) B_0	0
Infinite disk (⊥)	ΔB_z = (-σ + χ_i/3) B_0	0

2.2.3 Eddy Current

Besides the two static off-resonance sources mentioned in the previous subsections, there are also dynamic off-resonance sources. In MRI, time-varying magnetic fields produce the gradient field (dB/dr), which enables spatial encoding and imaging contrasts. The latter is frequently used for motion-sensitizing encoding, including diffusion weighting and flow encoding. Among the above applications, diffusion gradient typically uses nearly the full power of the gradient system, e.g., 95 % or higher of the maximum gradient amplitude in less than 1 ms. In contrast, the imaging gradient is lower, with the highest being 1/3 to 2/3 of the maximum amplitude. The flow encoding is usually lower, depending on the target flow velocity. The electric current is provided to the gradient coil during the gradient field switching. At the same time, an eddy current is generated according to Lenz's law, which creates the magnetic field perturbation. In general, the magnetic field generated by eddy current is time and space-dependent and can be written as below with the notations adapted from Bernstein et al. [40]

$$\mathrm{B_e}(\mathbf{r}, t) = \mathrm{B_0}(t) + \mathbf{r} \cdot \mathbf{B'}(t) + \text{higher order spatial terms}, \tag{2.15}$$

These spatial expansion terms in order are called $\mathrm{B_0}$ eddy current, linear eddy current ($\mathbf{B}$'(t) = d$\mathbf{B}$(t)/d$\mathbf{r}$ = $\mathbf{g}$(t)), and higher order eddy current terms. The eddy current generation may be modeled approximated to an inductive-resistive circuit

$$g(t) = -\frac{dG_{\mathrm{app}}}{dt} * \epsilon(t), \tag{2.16}$$

where $*$ is convolution, $\mathrm{G_{app}}$ is the applied gradient waveform, ϵ(t) is the eddy current impulse response and is the sum of mono-exponential with different decay constants

$$\epsilon(t) = \Sigma_n \alpha_n e^{-t}/\tau_{c,n}. \tag{2.17}$$

In the above presentation, the eddy current amplitude α can be either positive or negative and has to be measured by each scanner in nth time constants τ_{c}. It is usually divided into different constant ranges to distinguish their effects on the MR measurement. At the same time, the eddy current amplitude is usually expressed as the ratio to the applied magnetic field. For the modern magnet, the eddy current is roughly 5 % [41, 42]. For the well-active shielding and pre-emphasis adjustment, the eddy current can be reduced by approximately as an order of each [43]

$$G_{\mathrm{applied}}(t) = G_0 t/\tau_{\mathrm{ramp}}, 0 \leq t \leq \tau_{\mathrm{ramp}} \tag{2.18}$$

$$g(t) = -G_0/\tau_{\mathrm{ramp}} \cdot \alpha\tau_c(1 - e^{-t/\tau_c}), 0 \leq t \leq \tau_{\mathrm{ramp}}, \tag{2.19}$$

where G_0 is the gradient amplitude during the gradient plateau. The long-time constants that do not naturally decay to zero before the imaging encoding ends are considered in the current study and will be described later, leading to image distortion in EPI sequences. To the first-order approximation, the eddy current residual at the end of gradient field switching can be expressed as

$$g(t = \tau_{\text{ramp}}) \approx -G\alpha. \tag{2.20}$$

It means the maximum built-up eddy current field depends on the amplitude of the applied gradient and eddy current but is independent of time constants, slew rate (G/τ_{ramp}), and the main magnetic field.

Following the above model, eddy current is only generated during gradient switching or at ramps. After the ramp, the eddy current field is assumed to decay exponentially. The eddy current residual is the summation of the series of gradient ramps and is expressed as

$$B'_e(t) = g_e(t) = \Sigma_i \mp G_0\alpha e^{-(t-t_i)/\tau_c}, \tag{2.21}$$

where t_i is the time of the ith gradient switching. The contribution of eddy current during ramps is relatively minor and is neglected.

Table 2.3 summarizes examples of the eddy current residual calculation relative to a single gradient ramp. The calculated waveforms are the combinations of tripoidal gradient and are illustrated in Figure 2.3. It can be seen from the Taylor expansion that the eddy current residuals are functions of gradient duration (δ_g) and gradient delay (δ_{RF}). The third-order Taylor expansion calculates the residuals of each waveform, and the final residual is determined right after the last gradient ramp. The gradient delay in the last two dual bipolar waveforms is left to the RF allocation. Since the current study focuses on image distortion correction, a long-time constant is considered compared to the image readout ($\geq$ 100 ms). Also, for the same purpose, a long gradient duration simulates the largest eddy current scenario in MRI, i.e., diffusion gradient. Therefore, the gradient duration is set to 10 ms, the gradient delay is 10 ms, and the Eddy current constant is 100 ms.

Table 2.3: Analytical expression and numerical estimation of eddy current residuals correspond to the waveform in Figure 2.3.

	Gradient waveforms	**Eddy current residual $g_e(t)$**	**Relative residual (10 ms)**
	Gradient ramp	$-G\alpha e^{-t/\tau_c}$	1.0
(a)	Trapezoidal	$-G\alpha e^{-t/\tau_c}(\delta_g/\tau_c + 1/2\times\delta_g{}^2/\tau_c{}^2 + 1/6\times\delta_g{}^3/\tau_c{}^3 + 4\text{th} + \dots)$	0.105
(b)	Single bipolar	$-G\alpha e^{-t/\tau_c}(\delta_g{}^2/\tau_c{}^2 + 3\delta_g{}^3/\tau_c{}^3 + 4\text{th} + \dots)$	0.013
(c)	Even dual bipolar	$-G\alpha e^{-t/\tau_c}(\delta_g{}^2\delta_{\text{RF}}/\tau_c{}^3 + 4\text{th} + \dots)$	0.001
(d)	Odd dual bipolar	$-G\alpha e^{-t/\tau_c}(2\delta_g{}^2/\tau_c{}^2 + (6\delta_g{}^3 + \delta_g{}^2\delta_{\text{RF}})/\tau_c{}^3 + 4\text{th} + \dots)$	0.026

In a close look, the Taylor expansion expression is not restricted to any time constant. For the single trapezoidal gradient pulse, the eddy current residuals built during ramp-up

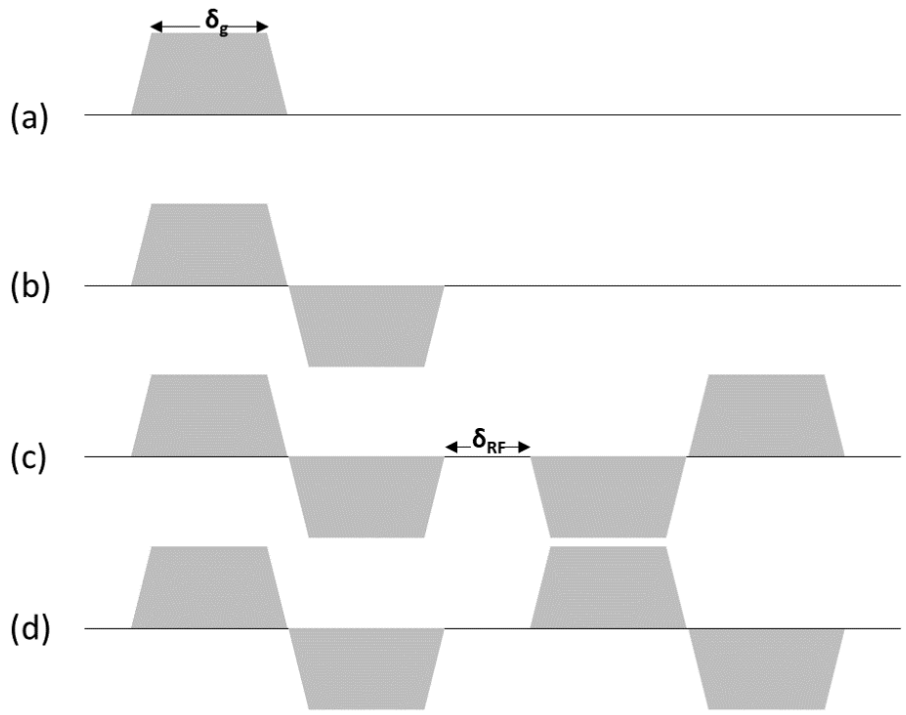

Figure 2.3: Common trapezoidal waveform combination in MRI. The analytical expression and numerical estimation of eddy current residuals corresponding to the waveforms are summarized in Table 2.3.

and down are partially canceled by each other due to the 0-order term elimination. A particular case for a single trapezoidal waveform without gradient duration is a triangular gradient pulse with zero eddy current residual, e.g., the blipped phase-encoding gradient in the blipped EPI (Figure 3.1, for example). In addition, the dual trapezoidal waveforms (e.g., Stejskal–Tanner gradient waveform) used in diffusion MRI are roughly doubled to the single trapezoidal waveform (Figure 2.4). In the signal bipolar waveform, the first-order terms are eliminated, so the residual is again significantly reduced. For the even-order dual bipolar, the pure gradient duration-dependent terms are eliminated, so the residuals are minimal. The last odd-order dual bipolar has roughly doubled residual to the single bipolar, similar to the relation of the Stejskal–Tanner gradient waveform to the signal trapezoidal waveform. Moreover, the EPI readout gradients are pairs of single bipolar, and the eddy current residuals are multiplied by the number of pairs. However, it is much smaller than those generated by diffusion gradient because of a smaller amplitude and natural cancellation.

2.3 Imaging Speed and Geometrical Fidelity of MR Sequences

The off-resonance effects described in Section 2.2 are general aspects and are unnecessary to lead image artifacts or signal loss to all sequences. In the aiming dMRI sequence of the current thesis, the most used signal type is SE because the SE is less sensitive to the off-resonance effects caused by artifact or signal loss than gradient echo-based sequences (GRE) and inherently doubled signal strength than the stimulated echo-based sequences (STE). Three sequences with distinctly different image encoding approaches for SE may be worth introducing before moving forward. They are constant time imaging (CTI) [44], conventional frequency-encoded spin-echo imaging (CSE) [44, 45], and single-shot echo-planar imaging (ss-EPI) [46]. The sequence order is by the sensitivity to the off-resonance effects from high to low and the imaging speed from low to high simultaneously.

The CTI is also called single-point imaging (SPI) [47] because the sequence acquires single-point data at each RF excitation. It is immune to the off-resonance effects in all physical directions compared to conventional frequency-encoded imaging. Because the complete spatial information of each spatial point is encoded independently, the unwanted phase errors do not accumulate at the next point. Thus, neither signal variation nor image distortion after the Fourier transform appears in the reconstructed image. On the contrary, the off-resonance phase accumulates to the readout (x) in CSE because the linear frequency-encoding gradient is applied, i.e., a readout line is acquired with each RF excitation instead of a point. However, the CTI has a significant disadvantage regarding low-resolution results from the long scan time. In an earlier experiment, 3D images with the exact sample sizes (533) showed that CSE took 14 minutes, whereas CTI took 5.75 hours, 25 times longer. If every scan parameter remains the same, then the CTI scan time will be proportional to the number of readout samples compared to the CSE.

Moreover, the fast 2D imaging sequence ss-EPI can have images with the same sample size as the other two sequences within seconds. The high speed of ss-EPI is via the complete in-plane (x, y) data acquired with an RF excitation. It is faster than the CSE by the number of phase encoding. However, the off-resonance effects in ss-EPI accumulate in each readout (x) and continuously accumulate in the echo train along phase-encoding (y). As a result, ss-EPI is primarily vulnerable to signal variation and geometric distortion in phase encoding (y) and a similar amount in readout (x) as in CSE.

The CTI and CSE are still used whenever high image fidelity is needed. However, *in vivo* human imaging, scanning with these two sequences is impractical. The succeeding subsection describes a general approach for imaging acceleration that can be applied to all these sequences.

2.3.1 Parallel Imaging

An approach to accelerate all SE sequences mentioned in Section 2.3 is parallel imaging (PI). Parallel imaging uses multiple RF receiving coils to replace the physical gradients for spatial encoding duty. The phase encoding steps are reduced via skipping several phase encoding lines in the k-space or, equivalently, reducing the FoV in the image space. A typical k-space skipped pattern in parallel imaging is skipped R_{PE} - 1 lines for every R_{PE} phase-encoding line. The R_{PE} is called a parallel imaging acceleration factor. However, according to the Nyquist theorem, direct Fourier inversion to data that skips k-space lines may result in an aliasing artifact. Specifically, the Nyquist theorem states that the sampling FoV must be larger than twice the size of the imaged object.

Typical methods that deal with parallel imaging aliasing are divided into image space-based methods (e.g., SENSE (sensitivity encoding [48]) and k-space-based methods (e.g., GRAPPA (generalized auto-calibrating partial parallel acquisition [49]). SENSE utilizes coil sensitivity (signal) information to unfold the aliased image in the image space. The sensitivity data is typically acquired with a low-resolution 3D image with extensive spatial coverage. By contrast, GRAPPA utilizes calibration data to calculate and refill the missing k-space to avoid image aliasing after Fourier inversion. The calibration data in GRAPPA is called autocalibration signal (ACS) and is typically acquired with a small amount of full phase-encoding sampled data ($R_{PE} = 1$) covering the k-space center.

The RF coil design largely determines the acceleration capacity of parallel imaging. This is because the original phase difference for spatial encoding added by the physical gradients is replaced with the information provided by the receiving coil. The ideal coil design is that the receiving signals from different coils partially overlap with each other and the overall extensive spatial coverage. The partial overlapping of the receiving coils creates signal weighting from different physical positions. As a result, parallel imaging has enough information to calculate the missing data and reconstruct the image with full FoV. An ideal coil with many spatially even distributed coils is a phased-array coil. The phased array receiving coil was initially proposed to increase the image signal by replacing a large volume coil with multiple small surface coils. In PI, the phased array coil also plays an essential role in acceleration capacity and increasing signal. The typical applicable acceleration factors of parallel imaging are 2 to 4 in one physical direction. This limitation is due to the extra noise generated from the unfolded FoV in SENSE or refilled k-space data in GRAPPA. The noise amplification is spatially variant and has a coil geometry dependency, thus called a geometric factor (coil g-factor). The coil g-factor is defined by the image noise amplification (more generally, SNR) from the full phase-encoding sampled image (SNR_{full}) to the accelerated image (SNR_{PE}) with accounting for the SNR change due to scan time reduction R_{PE} [48]

$$g_{\text{coil}} = \frac{1}{\sqrt{R_{PE}}} \frac{SNR_{\text{full}}}{SNR_{\text{PE}}}. \tag{2.22}$$

The geometry of the phased-array coil influences the coil g-factor, thus influencing the available acceleration. The physical size and number of coils, the coil placement in space, and the distance between the coil and the object are typically considered when developing a PI-compatible phase-array coil. A simulation study showed that the SNR in the current phased-array design for the human head has a distribution to different relative locations of the coil [50]. Together with the simulation results, the SNR increases linearly at the object surface relative to the number of coils, and the coil g-factor reduces with the B_0 increases. The $R_{PE} = 4$ at 7 T with a 32-channel coil is considered the maximum available acceleration in a single direction with an acceptable small coil g-factor 1.1. For an acceleration of PI factor 4, the scan time of SE sequences can be effectively reduced by four times. Thus, PI is almost standardized for ultrahigh-field human imaging and will be used throughout this study.

2.4 Diffusion MRI

Diffusion is a phenomenon of particle transport due to different spatial concentrations. Fick described the particle transport by a partial differential equation called the diffusion equation or Fick's second law [51]

$$\frac{\partial y}{\partial t} = \frac{\partial}{\partial x}(D\frac{\partial y}{\partial x}). \tag{2.23}$$

From the diffusion equation, the term within parentheses is the particle flow and is called Fick's first law

$$J = -D\frac{\partial y}{\partial x}, \tag{2.24}$$

where y(x, t) is the particle concentration, D is the proportional constant, and the negative sign represents the direction of particle flow.

In Fick's law of diffusion, the flow direction of particles is from high to low concentration, and its general solution is an exponential function. Einstein linked Stoke's law of dragging force [52] to diffusion equation to explain the spontaneous random walk of molecules (Brownian motion) [53]. By using particle conservation, with N particles starting to move at time 0 from x = 0 and assuming no interaction between particles, the solution of the diffusion equation is a normal function (Gaussian) with zero mean and 2Dt variance

$$y(x,t) = \frac{n}{\sqrt{4\pi Dt}} e^{-\frac{x^2}{4Dt}}. \tag{2.25}$$

Since the solution of the diffusion equation is in the form of a Gauss function, it is called

Gaussian diffusion. Einstein estimated the molecules' displacement by the root-mean-squared of variance ($\sqrt{2Dt}$). It is proportional to the squared root of time elapsing t and the self-diffusion coefficient D. The mean squared displacement becomes 6Dt when expanding the relation from 1D to 3D space.

A classic method of measuring self-diffusion uses isotropic tracers, which assume the tracer does not affect molecule isotropy. NMR spectroscopy and MRI provide another method without the need for a tracer. Holz et al. measured the water self-diffusion coefficient in varying temperatures by 1H NMR and compared it with the isotropic tracer method [54]. In order to encode the diffusion, time-varying diffusion gradients are added to the pulse gradient CSE. Results show a good agreement with an error of 1 %.

The essential diffusion sequence is adding a pair of motion-sensitized gradients before and after the refocusing RF in SE for diffusion encoding and decoding pulse accordingly (see Figure 2.4), in which the applied diffusion gradient can be defined with a vector $\mathbf{q}$(t)

$$\mathbf{q}(t) = \gamma \int_0^t \mathbf{g}(\tau)\, d\tau, \tag{2.26}$$

where the gradient g varies with different strengths and directions in a duration t. Commonly, the diffusion gradient pair is symmetric for most applications. Under this condition, static spins have no signal change after the end of decoding. In contrast, diffusion spins have signal attenuation due to incomplete phase cancellation. Since the diffusion encoding is usually on the order of tens milliseconds, the essential image contrast is T_2W in the *in vivo* 1H dMRI. Therefore, the signal in DWI needs to be carefully interpreted to avoid confusion with the T_2W signal.

In principle, the accurate signal change of DWI must be calculated using the Bloch-Torrey equation [55]. However, for this thesis's purpose and simplicity, an approximation of the Stejskal-Tanner equation [56] is used for calculating the signal attenuation instead. In addition, the relaxation and B_0 inhomogeneity are also omitted. With such conditions, the signal attenuation is written as

$$S = S_0 e^{-D \int_0^{\Delta+\delta_g} \mathbf{q}^2(t)\, dt}, \tag{2.27}$$

where δ_g is the duration of diffusion gradient, and Δ is the duration between diffusion encoding and decoding gradients. It is common to define a parameter b to represent the integral

$$b \equiv \int_0^{\Delta+\delta_g} \mathbf{q}^2(t)\, dt, \tag{2.28}$$

and is referred to as diffusion b-value.

In practice, diffusion generally becomes anisotropic in an environment of complications, e.g., biological tissue. This means the measured diffusion is not pure isotropic self-diffusion. Instead, perfusion and tissue microstructure also contribute to the diffusivity. Therefore,

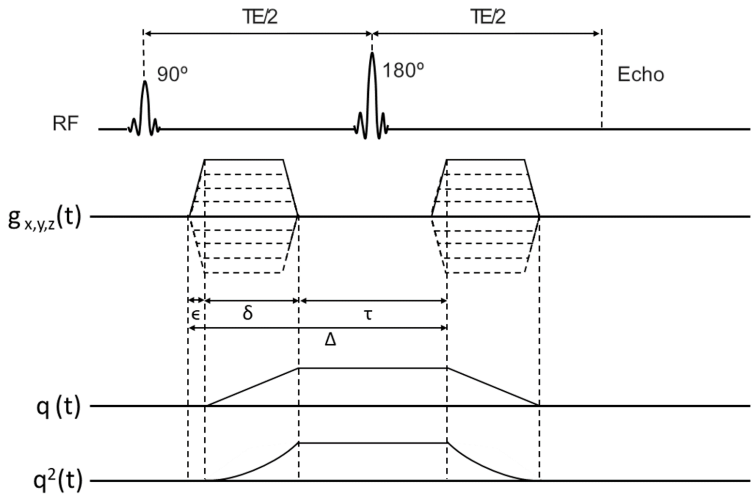

Figure 2.4: Stejskal-Tanner diffusion method. Two monopolar diffusion gradients are inserted before and after the spin-echo refocusing RF pulse to encode and decode the diffusion signal. Different diffusion gradient directions are manipulated by combining different gradient strengths g(t) in three physical directions (x, y, z). In addition, q(t) is the time integral of the diffusion gradient, and the commonly used parameter b is defined by $q^2(t)$.

the diffusion coefficient measured in MRI by the signal attenuation in tissue is termed the apparent diffusion coefficient (ADC) [57].

For the most used monopolar trapezoidal waveforms with spin echo sequence (Stejskal-Tanner method), the diffusion b-value for describing the signal attenuation in DWI can be generally expressed as below [58, 59]

$$b = \sigma^2\gamma^2\delta_g^2 g^2(\Delta - \frac{\sigma\delta_g}{3} + \frac{\epsilon^3}{30\sigma^2\delta_g^2} - \frac{\epsilon^2}{6\sigma\delta_g}), \tag{2.29}$$

where σ_e is the shape efficiency factor and is defined as

$$\sigma_e = \frac{1}{\delta_g g}\int_0^{\delta_g} G(t)\,dt, \tag{2.30}$$

where G(t) is the gradient shape. For a trapezoidal waveform, σ = 1 - ϵ/δ_g, i.e., the maximum efficiency is rectangular 1.

For analyzing and interpreting the dMRI data, each DWI with a different gradient direction shows a structure-dependent weighting pattern. At the same time, two DWIs with different b-values can be used to calculate the ADC. However, to eliminate the directional dependency, at least a set of orthogonal DWI (three DWIs) is used to calculate the directional independent DWI and ADC (see Figure 2.5), which are usually referred to as trace weighted image (TrWI) and mean diffusivity (MD) (see Figure 2.6), respectively

$$S_{\mathrm{TrWI}} = (S_x S_y S_z)^{1/3} = S_0 e^{-(b_x D_x + b_y D_y + b_z D_z)} \tag{2.31}$$

$$MD = (D_x + D_y + D_z)/3. \tag{2.32}$$

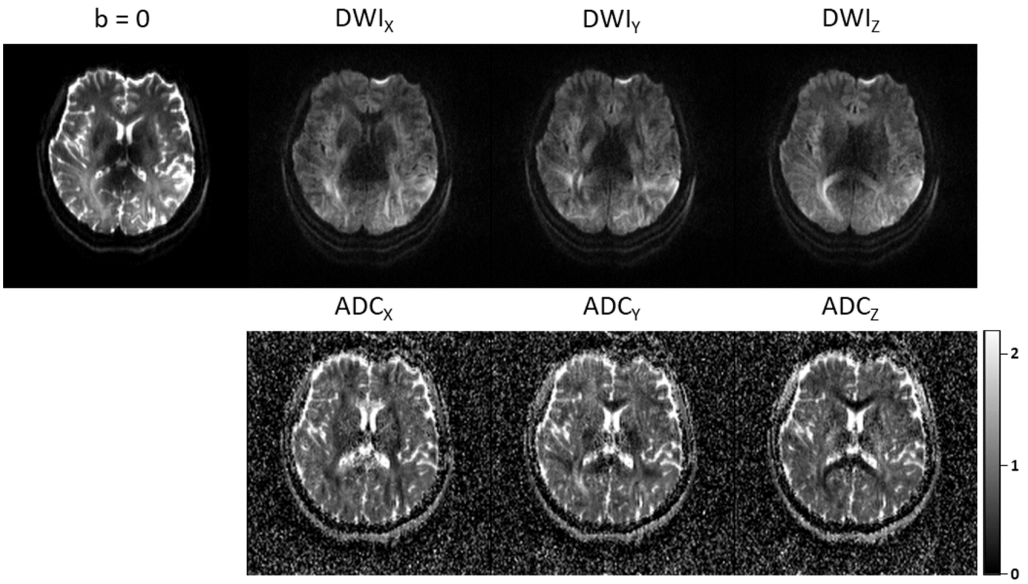

Figure 2.5: Diffusion images using the Stejskal-Tanner diffusion method with single-shot EPI image encoding. Each DWI and ADC encoded by the physical x, y, and z gradient directions has a directional dependency. The b-value of DWIs is 1000 s/mm^2. The imaging resolution is 1.4 mm^3.

Besser et al. proposed using a 3 × 3 diffusion tensor (**D**) to describe diffusion in the 3D spatial space [60, 61]. The signal equation can be expressed below

$$S = S_0 e^{-\sum_{i=x,y,z}^{3} \sum_{j=x,y,z}^{3} b_{ij} \mathbf{D}_{ij}}. \tag{2.33}$$

Using the symmetry property of the matrix, a minimum of 6 DWIs and one b = 0 image can solve the tensor to get three eigenvectors and three eigenvalues. Under diffusion tensor imaging, the diffusion displacement of each voxel is generally displayed by an ellipsoid, where the isotropic diffusion is a sphere. In the diffusion ellipsoid, the long axis is usually used to express the direction of the voxel as the fastest diffusion or least restriction. Two of the most used representations are fractional anisotropic (FA) and color-coded FA (col-FA) [62] (see Figure 2.7)

$$FA = \frac{1}{\sqrt{2}} \times \sqrt{\frac{(\lambda_1 - \lambda_2)^2 + (\lambda_2 - \lambda_3)^2 + (\lambda_3 - \lambda_1)^2}{\lambda_1^2 + \lambda_2^2 + \lambda_3^2}}. \tag{2.34}$$

The FA map is a voxel-wised anisotropic map, where one means the diffusion is only in a

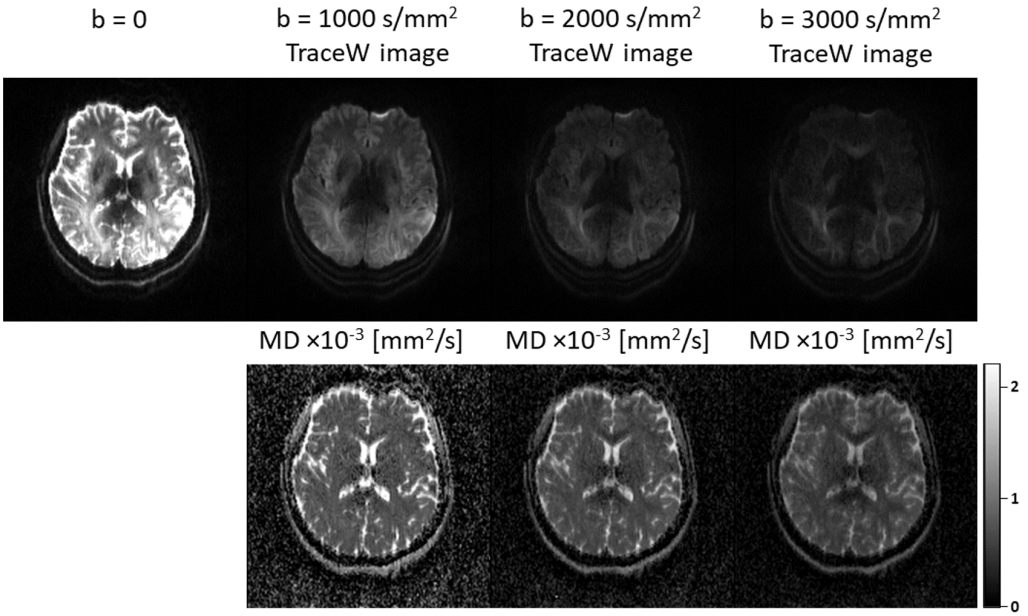

Figure 2.6: Diffusion images and maps derived from three orthogonal DWIs with different b-values (1000, 2000, and 3000 s/mm^2). Compared to DWI and ADCs in Figure 2.5, trace-weighted images (TrWI) and their mean diffusivity (MD) have no directional dependencies. Image intensity of TrWI and MD decreases with b-value with the rate CSF > gray matter > white matter because of the tissue microstructure and non-Gaussian diffusion of tissues. The imaging resolution is 1.4 mm^3.

specific direction while 0 means the isotropic diffusion (free diffusion). The color-coded FA represents the anisotropy index and the main diffusion direction simultaneously.

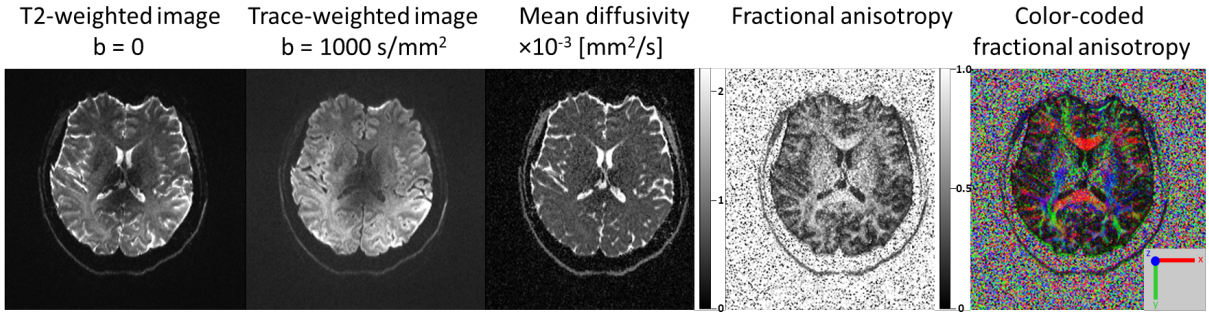

Figure 2.7: Diffusion images derived from the 6-directions DTI with b = 1000 s/mm^2. With three more non-colinear and non-coplanar DWIs, voxel-wised fractional anisotropy (FA) and the principal eigenvector (with the largest eigenvalue) color-coded FA can be derived. The imaging resolution is 1.0 mm^3.

Further dMRI analysis includes diffusion tractography [63], non-gaussian diffusion (hindered or restricted diffusion) [64], and perfusion [65]. As an extension of FA, diffusion tractography is the voxel-wise estimation of the connection of FA. It is used to analyze the structure connections. Gaussian diffusion of water is typically in the range of 200

$< b < 1500$ s/mm^2. In comparison, the perfusion is measured in the low b-value ($b <$ 200 s/mm^2) by the methods of intravoxel incoherent motions (IVIM) or pseudo-diffusion. Finally, non-gaussian diffusion usually needs a high b-value ($b > 1500$ s/mm^2).

Although CSE has very high image fidelity, in the *in vivo* dMRI, SE-EPI is the most used sequence because of its fast acquisition speed. The imaging speed for CSE is the number of readout encoding times faster than CTI. At the same time, the EPI is the number of phase-encoding times faster than the CSE, as mentioned in Section 2.3. For example, for 2D imaging of the matrix size of readout and phase-encoding (160, 160) with the same TR of 3 seconds, the acquisition time is more than 21 hours for CTI, 8 minutes for CSE, and 3 seconds for EPI.

However, since the analysis of dMRI needs to be calculated from the images of different diffusion b-values, image fidelity is also essential to yield the correct results. The off-resonance effects of chemical shift, susceptibility, and eddy currents from diffusion gradient are the biggest obstacles in dMRI whenever using EPI. Among the three major effects, the first two effects have B_0 dependencies, as mentioned in Sections 2.2.2 and 2.2.1. The effects are scaling with the B_0, thus very pronounced in the ultrahigh field MRI.

In addition, since diffusion encoding is accompanied by signal attenuation, it is important to maintain the SNR to obtain meaningful dMRI data. As mentioned in Section 2.1, compared to the lower field, the SNR at the ultrahigh field is only beneficial when the TE is short. In Figure 2.8, the relative TE for b-values ($b = 0$ to 10 s/mm^2), spatial resolution (2.5 mm^3 to 0.88 mm^3), and parallel imaging factors (1 to 4) for the vendor SE-EPI in a relatively high-performance clinical gradient system with maximum gradient strength 70 mT/m and slew rate 200 T/m/s at a human 7 T scanner are showed. From a cutoff TE of 75 ms, a b-value of 3500 s/mm^2 is feasible for the relatively low resolution (> 2.0 mm^3), 2500 s/mm^2 is possible for the moderate-high resolution (1.4 mm^3), 2000 s/mm^2 is feasible for the high resolution (1.17 mm^3 to 1.0 mm^3), and 1000 s/mm^2 for the very high resolution (< 0.88 mm^3).

2.5 Common Sequence Groups for *in vivo* Diffusion MRI

Although CSE has a very high image fidelity, acquiring one DWI generally takes a dozen minutes, especially when the resolution goes high, even with the PI. Therefore, dMRI sequences with further speeding up are desired for *in vivo* measurement. The modern accelerated dMRI sequences evolved from the CSE can be divided into echo-train sequences EPI [44,66,67] and TSE [68] groups. The following sections describe both methods in detail with their strength, applicability, and limitations in the ultrahigh field. In particular, EPI is sensitive to both B_0-dependent (susceptibility and chemical shift) and independent (eddy current) off-resonance effects, which leads to image distortion. In contrast, TSE has much higher energy deposition and is sensitive to the non-CPMG (Carr-Purcell-Meiboom-Gill),

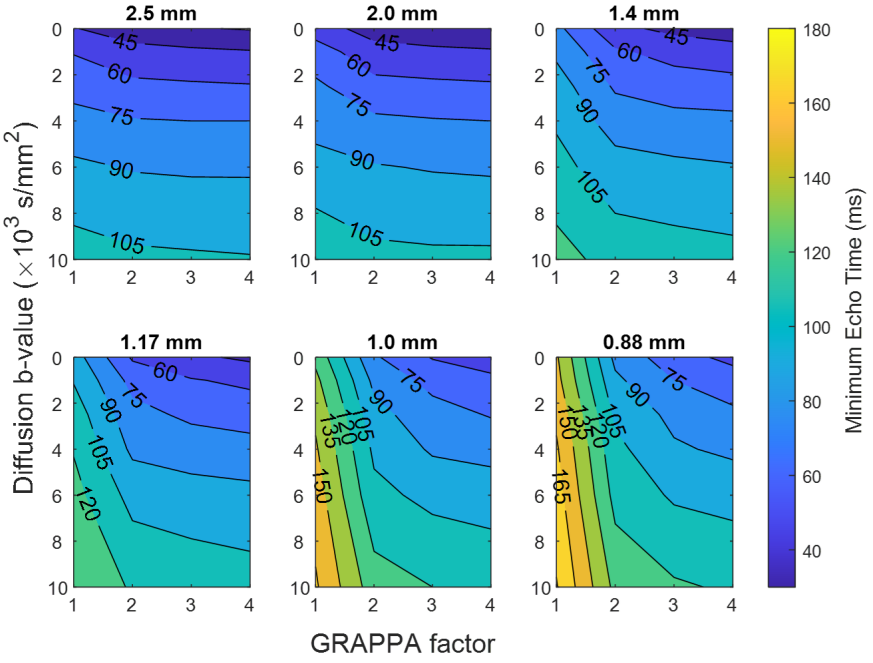

Figure 2.8: Minimum available TE of ss-EPI with varying GRAPPA factor and b-value in different (in-plane) imaging resolutions. The gradient system in the current study (70 mT/m, 200 T/m/s) is comparable to the modern high-performance clinical MRI scanner. Imaging SNR in dMRI is closely related to the TE, especially at the ultrahigh field: short TE is desired. Note that the TE is measured on the scanner with the Stejskal-Tanner diffusion method and partial Fourier 6/8.

which causes signal loss and artifact.

2.5.1 Turbo Spin Echo

TSE is an echo-train sequence, meaning multiple echoes (readout lines) are acquired in an RF excitation (90°). It employs various pairs of 180° refocusing RF pulse and phase-encoding gradients before each echo. The number of echoes acquired per RF excitation is called echo train length (ETL) or a turbo factor. The typical use of ETL is from 4 to 32. Compared to CSE, TSE is faster by the factor of ETL. Unless with the imperfection of the 180° refocusing pulse, TSE generally meets the CPMG condition; thus, there is high SNR and no non-CPMG artifacts [69, 70]. In addition, TSE has almost identical geometrical fidelity to CSE. This is because the TSE has no phase accumulation along the phase-encoding direction. Therefore, the image geometrical distortion is mainly in the readout direction, the same as CSE.

However, the higher turbo factor TSE toward single-shot is limited mainly because of tissue warming and image blurring *in vivo* MRI, especially in the ultrahigh field with desired high-resolution imaging. The echo train can be very long (> 100) in high-resolution

imaging to achieve the feasible scanning time. Consequently, the tissue warming resulting from the energy deposition of the RF pulses can be very high. It is measured in the specific absorption rate (SAR) with the watt per kilogram units. The SAR is squarely proportional to the applied RF pulse flip angle and linearly proportional to the numbers of the RF pulses and imaging slices. The SAR value is very high since the TSE has a series of 180° refocusing pulses. In addition, the energy deposition is related to the B_0 with a square proportionality. Thus, using TSE at the ultrahigh field is difficult, and it requires the rigorous compromise of imaging speed, in-plane resolution, and the number of slices. Although reducing the refocusing flip angle can mitigate the SAR limitation, it can also make the TSE susceptible to deviating from the CPMG condition, leading to signal loss and non-CPMG artifacts [71, 72]. A study comparing the available number of slices limited by TSE, multi-shot EPI, and single-shot EPI at 7 T human scanners showed that a maximum of 6 slices can be acquired with TSE and 32 slices with EPIs in the same TR (1.2 mm in-plane resolution, ETL 15, constant 120° refocusing pulses, and TR 4 sec) [73].

One particular imaging artifact in TSE is image blurring. The image blurring in TSE is in the phase-encoding direction, mainly because of the signal decay during the long echo train. Applying 180° refocusing pulse in TSE makes the echo train have T_2 decay instead of T_2* decay, which differs from the EPI. Thus, unlike EPI, there is no susceptibility artifact or chemical shift in the phase-encoding direction or intravoxel dephasing. The length of T_2 decay is relative to the total echo train duration, which is linearly proportional to echo spacing (ESP). The ESP is defined by the duration between echoes with the msec units. In TSE, the primary contributor to ESP is the duration of refocusing pulses. Each slice-selective 180° refocusing pulse needs a few milliseconds, so the TSE echo spacing is typically from 4 to 10 ms. It is relatively long compared to EPI, which typically has an ESP from 0.6 to 1 ms for modern gradient systems. As a result, the signal in the last echoes of TSE is significantly reduced. Since the peripheral components in a k-space are responsible for high spatial resolution or fine structures in the image after Fourier inversion, the signal decay in the lateral echoes makes the image blurring. In addition, a sharp signal decay after the k-space center can lead to image smearing, especially for the material with short T_2. The non-selective RF pulse may be used with 3D imaging to shorten ESP and thus reduce T_2 blurring in TSE. However, the imaging time may be prolonged.

In addition to the limitations of SAR and T_2 blurring, the imperfect 180° refocusing pulse and magnetization transfer (MT) also lead to signal loss in echoes, which is worse for the sequence with repetitive 180° pulses like TSE [74]. The refocusing pulse imperfection may be due to the non-ideal RF shape or the B_1 inhomogeneity. The latter is also higher in the ultrahigh field. Regarding MT, it refers to the protons bonded in different tissues at different spatial locations that are excited other than the initial designed excitation. Those protons in the different slices with short T_2 are saturated and do not contribute to

the initially excited slice, leading to a signal decrease. The MT effect becomes apparent when the slice number increases. As a result, signal loss due to MT is also more at the ultrahigh field due to a shorter T_2.

Despite the abovementioned limitations, TSE is still the workhorse in MRI scanners for morphological and relaxometry measurements, mainly due to its higher speed and compatible geometrical fidelity than CSE. In addition, similar to accelerating the other SE sequences, PI can be combined with the echo train MR sequences to make the imaging sequence faster. In TSE, the PI is used to reduce the scan time, and the T_2 blurring and SAR can be reduced. Therefore, further applications of TSE are desired. For example, functional MRI measures neuron activity, and dMRI measures microstructure. However, TSE has roughly a quarter of BOLD sensitivity and a half of BOLD contrast compared to the typically used GRE-EPI, making it less used in fMRI [75]. In dMRI, the applied motion-sensitized diffusion gradient makes TSE violate the CPMG condition, leading to additional signal loss and non-CPMG artifacts. Nevertheless, several methods have tried to overcome the non-CPMG limitation of TSE-DWI.

Applying diffusion gradient (DG) makes the TSE deviate from the CPMG condition, mainly because the directional motion sensitizes to the unknown phases after the diffusion module. It leads to the spins being mixed with CPMG and non-CPMG conditions, and the later condition makes the signal decay very quickly, primarily when refocusing below 180° . In addition, the inference of SE and STE with spins with different phases leads to signal non-smoothly decay along the echo train, creating artifacts. Thus, the typical non-CPMG behavior of TSE-DWI is a low signal, signal void, and spurious signal image in addition to the T_2 blurring. These can lead to errors in the dMRI analysis.

A straightforward method to overcome CPMG violation is to use only the CPMG signal by strictly keeping all refocusing pulses 180° . Thus, no non-CPMG component can degrade the echo signal. However, the method is challenging in the ultrahigh field due to the SAR limitation and the higher B_1 inhomogeneity. Also, the number of imaging slices that can be imaged by this method is very limited, even at the lower fields [76,77]. The rest of the methods can be divided into three categories: using a partial signal pathway [78], separating the signal pathways [79], and the full signal pathway with RF quadratic phase cycling [80]. Although all methods have been shown to have high geometrical fidelity and mitigate non-CMPG issues, the SNR has been reduced. In principle, for the partial pathways, a strong crusher gradient is used to eliminate half of the pathway, thus signal loss with a factor of 2. Despite the signals from different pathways being combined later, acquiring separated echo images doubled bandwidth for the splitting pathways methods, resulting in a signal loss with a square root of 2. The quadratic RF phase recycling can keep all signals without loss of signal. However, the required flip angle is relatively high compared to the other two methods.

In practice, the SNR reduction seems more than in theory for the latter two methods,

especially in the ultrahigh field. In an early implementation of the splitting signal method at 7 T, informative research was done by Sigmund and Gutman in which the EPI and TSE-DWI are compared at 3 T and 7 T. For the SNR comparison with counting for the difference in MR parameters, the SNR ratio of TSE to EPI is 50 % at 3 T and 30 % at 7 T [76] (see Figure 2.9). Moreover, the SNR gain from 3 T to 7 T is 1.71 for EPI and almost no gain (1.02) for TSE. A recent study of the (multi-shot) quadratic phase recycling method showed only a 30 % SNR increase compared to the partial pathway method at 3 T due to the SAR limitation [81]. This is because a high flip angle above 150° is needed to keep the method working. The study also commented that a 2-fold SNR increase at the lower field is feasible. However, it also indicates that the method may reduce more SNR than partial pathway methods at ultrahigh field. In addition, typical image blurring and smearing are still found in these methods [76, 77, 81–83].

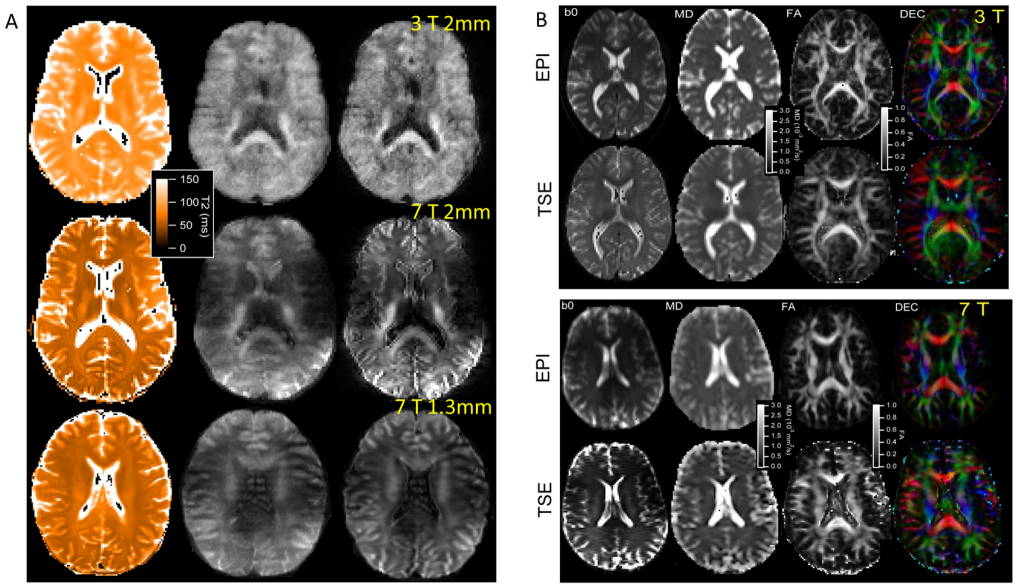

Figure 2.9: TSE-DWI at 3 T and 7 T scanners, b = 1000 s/mm^2. A: TSE-DWI deblurring. The structure boundaries are sharper after the deblurring correction (right column) than before (central column) by using a T_2 map (left column). However, the blurring cannot be fully corrected with the correction errors showing up. At the same time, banding artifacts and signal loss due to non-CPMG remain. B: Comparison of TSE-DWI and EPI-DWI. The non-CPMG artifacts in TSE-DWI pass to the dMRI analysis, leading to analysis errors despite no image distortion and less T_2* blurring than those from EPI-DWI. The figure adapted from Magnetic Resonance Imaging [76].

The abovementioned long ETL-related issues may be alleviated by combining multi-shot TSE to acquire shorter ETL with multiple RF excitations. The method compromises imaging speed by the number of shots. However, the object motion between shots leads to the phase difference, resulting in the ghosting artifact. Such motion artifacts can be

corrected by collecting extra low-resolution data at the k-space center to measure the phase changes. The acquired correction data is called navigator data. Thus, the method is called the navigator method. Moreover, it was shown that the non-diffusion rotating TSE (propeller-TSE) with a radial-like trajectory has an excellent correcting effect, in which the k-space center is scanned multiple times to be the navigator data [84]. However, propeller-TSE needs a 1.5 more k-space sweep than the conventional Cartesian trajectory to fulfill the Nyquist criterion, thus fundamentally reducing the imaging speed.

Furthermore, propeller-TSE uses MLEV RF phase cycling, which differs from CPMG and quadratic phase cycling and is thus not robust for long echo trains [80]. It was also found that the motion correction in the propeller-TSE-DWI is less efficient than propeller-TSE [85]. Later, the EPI signal replaced part of the TSE echoes to alleviate ETL issues further [86, 87]. However, it is then further compromised with imaging speed to the motion and geometric robustness.

In summary, the TSE sequence group in dMRI has many limitations that are particularly unsuitable for ultrahigh fields. In addition to the artifacts and high SAR, the non-CPMG nature makes the signal gain from the ultrahigh field easily reversed, which is on top of the shortened apparent T_2 issue mentioned in Section 2.1. Hence, the TSE-DWI was not selected as the topic for the current study. However, due to its high geometrical fidelity, non-diffusion TSE will be used as the reference images for the current study.

2.5.2 Echo-planar Imaging

EPI is also an echo-train sequence. Similar to TSE, it acquires multiple echoes in a single RF excitation. When it comes to the SE signal (SE-EPI), it has only one RF refocusing before completing the whole k-space traversal, and thus, SAR is relatively low, which is the major difference from TSE. As a result, the typical usage of EPI is a single-shot EPI (ss-EPI), which means it fills the full 2D k-space in one excitation. Consequently, EPI is generally much faster than TSE but is more sensitive to the off-resonance effects.

The iconic presentation of off-resonance effects in EPI is image distortion, which is the primary flaw when EPI is used in dMRI. This is because most of the analyses in dMRI require multiple DWIs to calculate results voxelwisely. Image distortion in dMRI does not only lead to the inaccuracy of spatial information but can also lead to misleading interpretation. It will be seen later that the image distortion in EPI is severe in the phase-encoding direction and becomes worse in the high-resolution imaging (see Figure 3.2A). Moreover, the distortion from certain off-resonance effects are scaling with B_0 and thus are particularly critical in the ultrahigh field.

In the following subsections, image distortion of EPI that came from off-resonance effects will be explicitly derived. The off-resonance effects are represented by the field deviation ΔB from the on-resonance Larmor frequency, which is the summation from Section 2.2. Later, two very different methods used in the current thesis to correct the image distortion

from the off-resonance effects will also be derived explicitly as the foundation of the proposed sequence described in the next section. Note that the following derivations are for a general aspect of EPI, not restricted to the SE-EPI or dMRI.

2.5.2.1 Image Distortion in EPI

Consider a 2-D Cartesian blipped EPI signal equation with off-resonance effects induced field deviation ΔB(x,y) in both readout and the phase-encoding directions. If ignoring the relaxation effects and the blurring sources, the signal equation may be written as

$$S(k_x, k_y) = \int_x \int_y \rho(x,y) e^{-2\pi i(k_x \cdot x + k_y \cdot y)} e^{-2\pi i(k_x \cdot \frac{\pm \Delta B(x,y)}{G_x})} e^{-2\pi i(k_y \cdot \frac{\Delta B(x,y) T_{\text{esp}}}{\overline{G}_y \tau})} \, dx \, dy, \qquad (2.35)$$

where the $\rho(x,y)$ is the physical spin density (object) being imaged, k_{x} and k_{y} represent 2D Fourier imaging encodings, G_{x} is the amplitude of readout gradient, $\bar{\text{G}}_{\text{y}}$ is the averaged amplitude of phase-encoding blips with duration τ, and T_{esp} is the effective EPI echo spacing. The estimated spin density of EPI can be obtained by the inverse Fourier transform and is written as

$$\begin{aligned}
\hat{\rho}(x,y) &= \int_{k_x} \int_{k_y} S(k_x, k_y) e^{+2\pi i(k_x \cdot x + k_y \cdot y)} \, dk_x \, dk_y \\
&= \int_{k_x} \int_{k_y} \{ \int_{x'} \int_{y'} \rho(x',y') e^{-2\pi i(k_x \cdot x' + k_y \cdot y')} e^{-2\pi i(k_x \cdot \frac{\pm \Delta B(x',y)}{G_x})} e^{-2\pi i(k_y \cdot \frac{\Delta B(x,y') T_{\text{esp}}}{\overline{G}_y \tau})} \, dx' \, dy' \} \\
&\quad e^{+2\pi i(k_x \cdot x + k_y \cdot y)} \, dk_x \, dk_y \\
&= \int_{x'} \int_{y'} \rho(x',y') \, dx' \, dy' \int_{k_x} e^{-2\pi i(k_x \cdot \{x' + \frac{\pm \Delta B(x',y)}{G_x} - x\})} \, dk_x \\
&\quad \int_{k_y} e^{+2\pi i(k_y \cdot \{-y' - \frac{\Delta B(x,y') T_{\text{esp}}}{\overline{G}_y \tau} + y\})} \, dk_y \\
&= \int_{y'} \int_{x'} \rho(x',y') \, dx' \, dy' \delta(x' + \frac{\pm \Delta B(x',y)}{G_x} - x) \delta(y' + \frac{\Delta B(x,y') T_{\text{esp}}}{\overline{G}_y \tau} - y) \\
&= \rho(x - \frac{\pm \Delta B(x,y)}{G_x}, y - \frac{\Delta B(x,y) T_{\text{esp}}}{\overline{G}_y \tau}) \\
&= \rho(x,y) * \delta(x - \frac{\pm \Delta B(x,y)}{G_x}, y - \frac{\Delta B(x,y) T_{\text{esp}}}{\overline{G}_y \tau}),
\end{aligned} \qquad (2.36)$$

where * is the convolution operator, and δ function is the Dirac delta function. The definition of the Dirac function and its three Fourier properties used for deriving the equations are described in Appendix A.

In the above derivation, the estimated spin density of the EPI signal (EPI image) is the physical spin density that convolves with a spatial varied impulse function or a shifted delta

point spread function (PSF) in both x (readout) and y (phase encoding) axes, representing the in-plane image distortion.

It can be seen that the amount of distortion $\Delta B(x,y)/G_x$ in readout and $\Delta B(x,y)T_{esp}/\bar{G}'_y\tau$ in phase-encoding are inversely proportional to the gradient amplitude on each axis. From the expression, it can define the amplitude of the normalized phase-encoding gradient ($\bar{G}'_y=\bar{G}_y\cdot\tau/T_{esp}$). Thus, the higher the gradient amplitude, the lower the image distortion. When FoV is fixed, the encoding-gradient amplitude is proportional to the sampling bandwidth, i.e., BW = $\gamma/2\pi\cdot$FoV$\cdot$G. Unlike the readout bandwidth controllable in EPI (or more general in MRI), the phase encoding bandwidth varies corresponding to the readout bandwidth via T_{esp}, which is the number of readout samples multiplied by the dwell time (1/BWr). As a result, a typical high readout bandwidth is preferred to minimize T_{esp}, reducing distortion in the phase-encoding direction. Moreover, the increase of spatial resolution of EPI elongated the T_{esp}, thus increasing distortion.

For example, in a 1.4 mm^3 resolution EPI without PI (GRAPPA 1), the readout gradient amplitude without ramp-sampling is 30.84 mT/m. The normalized phase-encoding gradient amplitude is 0.1305 mT/m (gradient system: maximum strength 70 mT/m, maximum slew rate 200 T/m/s). The normalized phase-encoding gradient amplitude is 236 times smaller than the readout, resulting in a dramatic image distortion in the phase-encoding direction than in the readout. In addition, the readout amplitude in EPI is often larger than the conventional frequency-encoded sequences. As a result, the distortion correction in the EPI readout may be omitted.

PI can also be used in EPI. In addition to reducing imaging time, the unwanted phase of off-resonance accumulation during the echo train leads to image artifacts like distortion and blurring that can be reduced owing to the reduction of T_{esp}. Moreover, the TE in EPI may also be shortened to increase image SNR by using PI. Since T_2* and apparent T_2 are reduced with increasing main magnetic strength, PI is attractive to the ultrahigh field MRI. The current study will combine parallel imaging with the proposed sequence to further pursue high spatiotemporal resolution imaging.

The EPI is selected to be studied for the ultrahigh-field dMRI in the current thesis because its main flaw in the ultrahigh field is the increased image distortion from the static off-resonance effects. Compared to the TSE, there were more strategies to deal with the existing challenges in the lower fields. Combining some strategy to form a new EPI sequence with no image distortion in the ultrahigh-field dMRI may be realizable. In the following subsections, three major off-resonance effects that lead to image distortion of EPI in dMRI will be introduced, with illustrations, the corresponding established correcting methods, and their limitations.

2.5.2.2 EPI Distortion due to Susceptibility Difference

The typical highest susceptibility difference in human MRI is the air-tissue of ≈ 9 ppm. Following by the example in Section 2.5.2.1, a ss-EPI with 1.4 mm isotropic resolution and 22.4 cm FoV has a readout bandwidth of 1838 Hz/px and a phase-encoding bandwidth of 7.8 Hz/pixel (echo-spacing 0.8 ms) for the conventional whole-body gradient system (70 mT/m, 200 T/m/s). The position errors range from 0.5-1.5 mm in the readout direction and 121-363 mm in the phase-encoding direction. In converting the unit to the pixel number, the distortion is 0.34-0.94 in readout and 76-227 in phase-encoding. From the estimation, distortion smaller than 1.0 pixels in readout can be ignored. However, the phase-encoding distortion needs to be corrected. Modern human MRI at high fields (≥ 3 T) are typically equipped with a high number of receiving coils (≥ 8 coils) that allow using of parallel imaging acceleration (e.g., GRAPPA). The in-plane GRAPPA acceleration can increase the effective phase-encoding bandwidth to reduce signal variation and distortion. In the applications of fMRI and dMRI at the ultrahigh field (≥ 3 T), high GRAPPA factors are preferable to reduce distortion, T_2*/ T_2 blurring, and TE. A simulation of susceptibility distortion is shown in Figure 2.10 to illustrate its B_0 field-dependent nature and localized effect. The off-resonance is 9.05 ppm, and the effective EPI echo spacing is 0.4 ms. It can be seen that the susceptibility distortion is changing along the phase-encoding direction. The susceptibility distortion is localized, which means it is severe at the center of off-resonance sources and decreases quickly with distance. This mimics the severe susceptibility distortion at boundaries with adjacent substances with different susceptibility *in vivo*, e.g., tissue and air. In addition, the strength of distortion is linearly scaling with the B_0 field, which is minor at 0.55 T and massive at 7 T. The susceptibility distortion can lead to the difficulty of misregistration in the data analysis and may lead to inaccurate and misinterpreting results.

The commonly established methods to correct or reduce EPI susceptibility distortion can be divided into correcting during or after scanning. The most common methods of reducing during scans are the multishot EPI methods [88]. These methods reduce the number of samples in each RF excitation to make the T_{esp} smaller, resulting in smaller distortion. The limitations of these methods are the increase in scan time to the number of shots and the inability to correct the susceptibility distortion fully. View-angle tilting (VAT) [89, 90] is a less commonly used method to correct susceptibility distortion during the scan, which will be introduced in detail in Section 2.5.4. The after-scan correct (post-processing) method typically acquires extra information to calculate the pixel shift map for later to correct the distortion. The common post-processing methods are field mapping [91], EPI with different phase encoding directions [92], and multi-reference methods [93]. The former two methods are usually unable to correct distortion when the distortion is relatively large, e.g., at an ultrahigh field, resulting in artifacts and blurring. As a multi-reference correcting

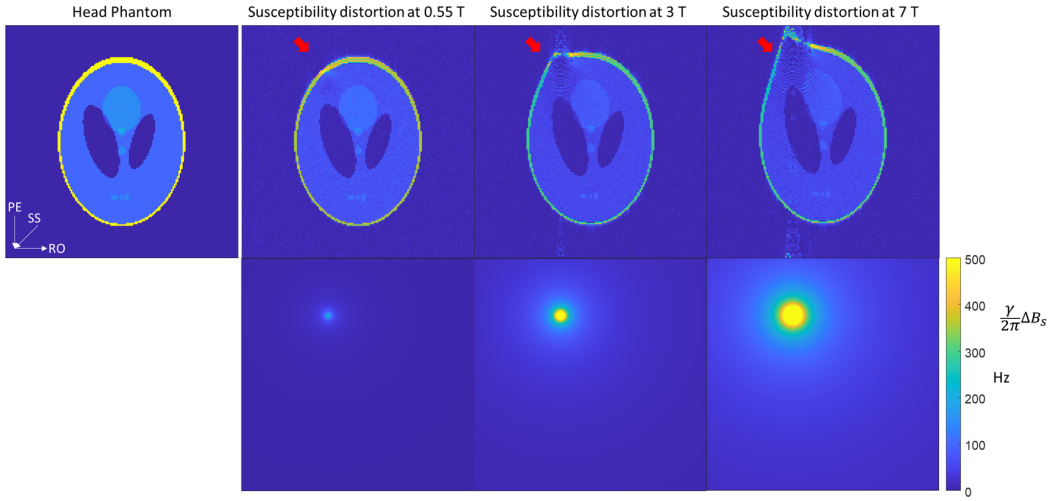

Figure 2.10: Simulation of image distortion in EPI due to susceptibility difference. The head phantom and its images simulated from EPI with three B_0 fields, 0.55 T, 3 T, and 7 T, are shown on the top row. On the bottom row, the off-resonance is expressed in Hertz, corresponding to the different B_0 fields. The simulated off-resonance is 9.05 ppm at the center and decreases with the square of the distance (cylinder), and the EPI effective echo spacing is 0.4 ms. In EPI, the red arrow indicates the distortion. It mainly changes (stretching, compressing, and scaling) along the phase-encoding direction and is severely close to the off-resonance center. In addition, the strength is linearly scaled with the B_0 field. RO: readout. PE: phase encoding. SS: slice selection. ΔB_S: susceptibility off resonance.

approach, the latter can robustly correct a more considerable distortion, e.g., point-spread function mapping EPI (PSF-EPI). The details of PSF-EPI will be described later in the Section 2.5.3. Moreover, these methods are limited because they are sensitive to dynamic field change due to subject movement between scans or eddy currents generated from changing diffusion gradients. The dynamic field change will also lead to artifacts and blurring in the corrected images.

2.5.2.3 EPI Distortion due to Chemical Shift

In conventional frequency-encoded imaging, the frequency difference from chemical shift leads to spatial mismapping in the frequency encoding (readout) direction. For a set 260 Hz/px receiving bandwidth, the fat-water chemical has 0.30 pixels shift at 0.55 T, 1.69 at 3.0 T, and 3.85 at 7 T. In contrast, no pixel shift is caused by the chemical shift in the phase encoding direction. The bulky shift of fat signal is relatively small, even at 7 T. In comparison, the chemical shift in EPI is mainly in the phase encoding direction. This is because the receiving bandwidth in the frequency encoding is often larger than 1000 Hz/px and less than 10 Hz/px effectively in the phase-encoding, similar to the susceptibility off-resonance. The effective bandwidth is still limited even with parallel imaging techniques.

For example, a 1.4 mm resolution EPI brain imaging with GRAPPA 2 at 7 T has a 14.2 Hz/px effective bandwidth, thus a 70-pixel shift of fat and water. As an illustration, the chemical shift in EPI is simulated with a head phantom, as shown in Figure 2.11. It assumes the only off-resonance is the outer ring, mimicking the subcutaneous fat of the scalp, and the rest of the phantom has homogeneous fields mimicking other tissues. In the simulation, the chemical shift off-resonance is 3.35 ppm between fat and water, and the effective echo spacing is 0.4 ms. It can be seen that the fat signal overlaps on the tissues and the shift scales with the B_0 field. Unlike susceptibility off-resonance, the chemical shift does not change its geometry in the image, thus maintaining high intensity to the entire structure extent. Since fat signals and other tissues have very different relaxometry and diffusivity, chemical shifts can lead to misinterpretation of the data and confounding with pathological signals when the fat signal is much brighter than other tissues, e.g., in dMRI. Moreover, the chemical shift pattern is messy when combined with other EPI artifacts like Nyquist ghosting, parallel imaging artifacts, and other off-resonance effects. In that circumstance, the fat signal folds many times in the image and thus usually worsens in the ultrahigh field.

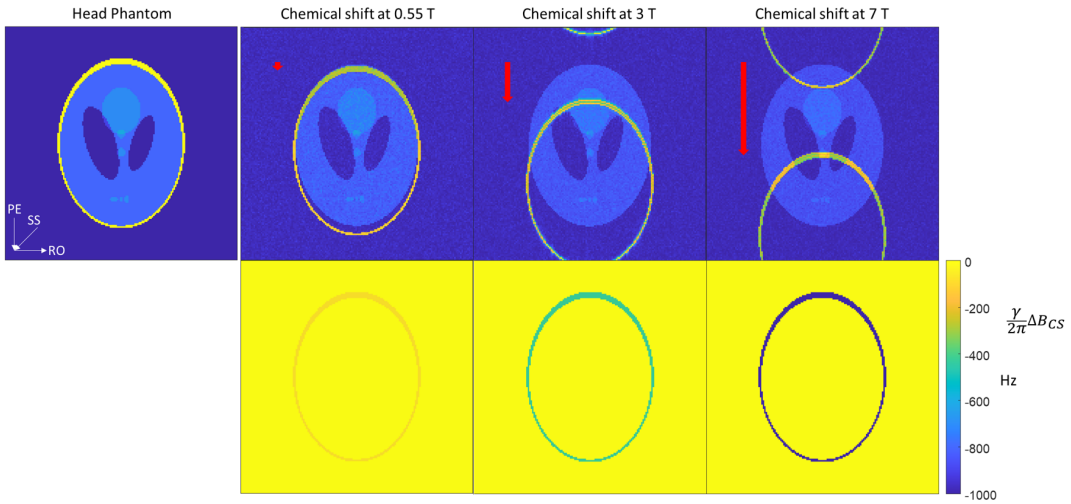

Figure 2.11: Simulation of image distortion in EPI due to chemical shift. The head phantom and the simulated EPI with chemical shift in three B_0 fields, 0.55 T, 3 T, and 7 T, are shown on the top row. On the bottom row, the chemical shift off-resonance of 3.35 ppm is expressed in Hertz with different B_0 fields. The EPI has an effective echo spacing of 0.4 ms, and the red arrow indicates the chemical shift strength. Similar to susceptibility off-resonance, the chemical shift changes along the phase-encoding direction, and the strength is linearly scaled with the B_0 field. However, the signal of chemical shift does not decrease with distance, e.g., in the extent of the scalp. RO: readout. PE: phase encoding. SS: slice selection. ΔB_{CS}: chemical shift off-resonance.

The primary methods of dealing with chemical shifts can be sorted into a few categories [94], and all of them can apply to EPI. The first category is the fat suppression methods,

including the most commonly used spectral fat suppression, differentiated inversion recovery, and a combination. Methods in the second category are similar to those in the first, except the sophisticated RF series excites water signals instead of suppressing fat. The third category is the fat-water separation methods (e.g., Dixon [95, 96]), which use the nature of the chemical shift to acquire the water-fat in-phase and out-of-phase images and calculate the separated fat and water images. The fourth category is mainly for spin-echo sequences, including excitation-refocusing gradient inversion and transmitting bandwidth differentiation [97]. The last method is VAT [89, 90], which can correct the shifted fat signal.

In the abovementioned methods of dealing with chemical shift in MRI, the first three methods are the spectral methods, which need to determine the off-resonance frequency to be suppressed or excited and thus are sensitive to the B_0 and B_1 field inhomogeneities, which increases the correcting difficulties at ultrahigh fields. The Dixon methods are slightly less sensitive to the field inhomogeneity. However, they need to model the desired frequency difference to be separate, and usually, only one frequency difference is possible to separate the signal ideally. As a result, a more robust and general method for correcting the chemical shift is desired in ultrahigh fields. The more general correcting method VAT and its advantages and disadvantages will be introduced in Section 2.5.4.

2.5.2.4 EPI Distortion due to Eddy Current

In addition to the susceptibility and chemical shift, the gradient switching in MRI generates spatiotemporal dependent eddy current (see 2.2.3) as a dynamic off-resonance. The time-varying eddy currents create extra magnetic fields, leading to unwanted image distortion in fast imaging sequences, especially in EPI. In the presence of diffusion gradients, strong and long diffusion gradients can have very high eddy current residuals even after the system optimization. The temporal dependency of eddy current residual can be modeled to multiexponential decay, which has different decay time constants. For a modern MRI, a trend to use high parallel imaging factors (three to four) makes the EPI readout on the order of a hundred milliseconds. By comparing the duration of the EPI readout train, eddy current decay time constants can be sorted using a different time constant range. The featured time scales are ultra-short time constants ($\leq$ 1 ms), intermediate time constants (10 to 100 ms), and long time constants ($\geq$ 100 ms). The ultra-short time constants are responsible for the Nyquist ghost, which can be corrected well in the conventional gradient system (the ghost-to-noise ratio is usually much less than 10 % with GRAPPA $\geq$ 1). Meanwhile, the intermediate time constants that vary during EPI readout cause small image blurring. The longer intermediate- and long-time constant act as background encoding gradients and contribute to the image distortion of shearing, scaling, and shifting. In Figure 2.12, the effects of the eddy current residual are simulated in EPI by adding the eddy current residual from the orthogonal directions (x, y, z). The shearing, scaling, and

shifting are generated correspondingly from the eddy current residual of readout, phase encoding, and slice selection directions. As a result, the derived information from the images with eddy current off-resonance is inaccurate, even with the basic syntheses image of averaging. In practical dMRI applications, more diffusion b-values and directions are usually desired. Since the diffusion directions are realized by combining gradient strength and the three physical gradient directions, the distortion becomes complicated, especially when other off-resonance effects join.

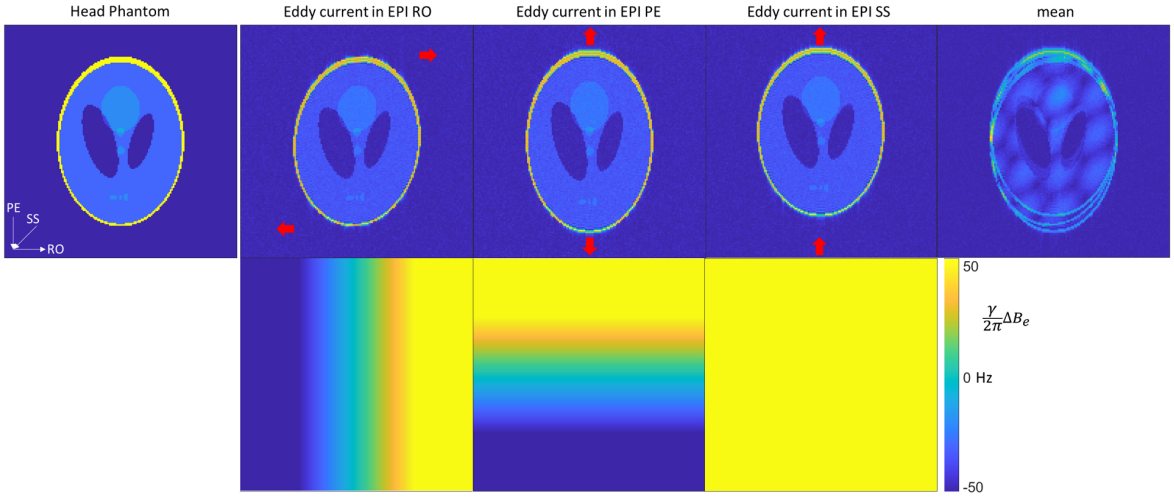

Figure 2.12: Simulation of image distortion in EPI due to eddy current. The head phantom and the simulated EPI with the appearance of a long-time constant eddy current in the readout (x), phase encoding (y), and slice selection (z) are shown on the top row. In addition, the average of the three distorted EPIs is also shown to mimic the commonly used mean DWI. On the bottom row, the simulated eddy current off-resonance of 100 Hz is shown in the corresponding directions. The EPI effective echo spacing is set to 0.4 ms, and the red arrows indicate the directions of eddy current distortion or shifting. The readout, phase encoding, and slice selection eddy current are responsible for the EPI distortion of shearing, stretching, and shifting, respectively. The mean distorted image cannot give accurate information if the eddy current off-resonance is not corrected well. Moreover, unlike susceptibility and chemical shift off-resonances, the eddy current is independent of the B_0 field, thus the distortion is not scaling with the B_0 field strength. RO: readout. PE: phase encoding. SS: slice selection. ΔB_e: eddy current off-resonance.

There are many approaches to reduce or correct eddy current distortion, which can be sorted into a few categories. The first category is hardware design to break eddy current, for example, active shielding and interrupt current loop [98, 99]. Although the amount of eddy current is largely reduced, the small residual still distorts ss-EPI. The second is to characterize eddy current via additional measurements and then correct distortion via modifying pre-emphasis [100] or post-processing [43]. The measurements either need a long measurement time to improve the accuracy, need assumptions or need

extra equipment [101]. The assumptions, for example, are that distortion has an axial symmetry of gradient that has an opposite polarity or that the eddy current characteristic does not change as time passes. However, these assumptions may not be valid if the scanning environment changes, e.g., the change of imaging protocol, subject, or other interferences. In such a situation, the calibration needs to be performed again. The third category is changing diffusion gradient waveform to cancel or null eddy current residual, e.g., TRSE [41]. Although these methods may largely reduce the eddy current residual, its primary null time constant must be empirically determined to optimize the performance. This increases the difficulty of optimization for common users. In addition, usually, only one primary time constant can be selected to be optimized. The method needs a trade-off selection for multiple time constants with comparably large residuals. Moreover, the total duration will be increased due to the usually lower diffusion efficiency of these waveforms than Stejskal-Tanner. As a result, the TE increases, which leads to the SNR reduction, particularly in ultrahigh fields. Fourth, EPI in-plane parallel imaging or multi-shot sequences can reduce distortion by lowering effective echo spacing. These approaches hardly eliminate eddy current distortion and either reduce SNR with high parallel imaging or much longer scan time with many shots.

In summary of EPI distortion, in order to improve the accuracy of ultrahigh-field dMRI, it is urgent to develop a fast method that can simultaneously correct the image distortion from the abovementioned off-resonances. To make the new method robust, a method that can correct the distortion during scan without complex modeling, dedicated calibration, and time-consuming post-processing calculation is desired. In the following sections, two candidate methods are selected to be described in detail for use in the proposed method in the next chapter.

2.5.3 Point Spread Function Mapping EPI

As shown in the previous section, image distortion in EPI due to off-resonance effects is straightforward to derive from the Fourier encoding and inversion as in Equations 2.35 and 2.36. For a close look, the off-resonance effects lead to the unwanted phase of spins accumulating point-by-point over time, resulting in the encoded frequency being different from the physical position. If the phase information of individual points can be recorded before forming the image, the distortion can be characterized and corrected. Point spread function mapping is a method that can record the phase evolution in MRI [102]. It applies an extra constant-time phase-encoding gradient (called PSF encoding), identical to the CTI phase encoding, to the sequence of an axis to be corrected. The image distortion can be later corrected in the image domain (see Figure 3.2B).

As shown in Section 2.5.2.1, the distortion amount in EPI is relatively tiny in the readout direction, so the PSF encoding is only added to the EPI phase-encoding dimension in the following derivation [93, 103]. The method is abbreviated as PSF-EPI. An EPI echo

train follows each PSF phase-encoding step in the PSF-EPI's sequence loop. Each applied PSF phase-encoding step has the same amount of y-dependent phase accumulation to each EPI blip when there is no in-plane under-sampling, e.g., GRAPPA. As a result, the phase evolution of EPI phase encoding can be recorded faithfully. Starting from the signal equation of EPI before performing the Fourier inversion, a constant-time phase-encoding gradient representing PSF encoding applies to the y-axis. The signal equation of PSF-EPI can be formulated as

$$S(k_x, k_y, k_{y_1}) = \int_x \int_y \rho(x,y) e^{-2\pi i(k_x \cdot x + (k_y + k_{y_1}) \cdot y)} e^{-2\pi i(k_y \cdot \frac{\Delta B(x,y) T_{\text{esp}}}{\overline{G}_y \tau})} \, dx \, dy. \tag{2.37}$$

By performing the inverse Fourier transform with respect to k_{x}, k_{y} and k_{y_1}„ the estimated spin density can be obtained:

$$\begin{aligned}
\hat{\rho}(x,y,y_1) &= \int_{k_{y_1}} \int_{k_y} \int_{k_x} S(k_x, k_y, k_{y_1}) e^{+2\pi i(k_x \cdot x + k_y \cdot y + k_{y_1} \cdot y_1)} \, dk_x \, dk_y \, dk_{y_1} \\
&= \int_{k_{y_1}} \int_{k_y} \int_{k_x} \{ \int_x \int_y \rho(x',y') e^{-2\pi i(k_x \cdot x' + (k_y + k_{y_1}) \cdot y')} e^{-2\pi i(k_y \cdot \frac{\Delta B(x',y') T_{\text{esp}}}{\overline{G}_y \tau})} \, dx' \, dy' \} \\
&\quad e^{+2\pi i(k_x \cdot x + k_y \cdot y + k_{y_1} \cdot y_1)} \, dk_x \, dk_y \, dk_{y_1} \\
&= \int_{k_y} \int_{y'} \int_{x'} \rho(x',y') \int_{k_x} e^{+2\pi i(k_x \cdot (-x' + x))} \, dk_x \, dx' \int_{k_{y_1}} e^{+2\pi i(k_{y_1} \cdot (-y' + y_1))} \, dk_{y_1} \\
&\quad e^{+2\pi i(k_y \cdot (-y' - \frac{\Delta B(x',y') T_{\text{esp}}}{\overline{G}_y \tau} + y)} \, dy' \, dk_y \\
&= \int_{k_y} \int_{y'} \rho(x,y') e^{+2\pi i(k_y \cdot (-y' - \frac{\Delta B(x,y') T_{\text{esp}}}{\overline{G}_y \tau} + y)} \delta(y' - y_1) \, dy' \, dk_y \\
&= \int_{k_y} \rho(x,y_1) e^{+2\pi i(k_y \cdot (-y_1 - \frac{\Delta B(x',y_1) T_{\text{esp}}}{\overline{G}_y \tau} + y)} \, dk_y \\
&= \rho(x,y_1) \delta(y - y_1 - \frac{\Delta B(x',y_1) T_{\text{esp}}}{\overline{G}_y \tau}).
\end{aligned} \tag{2.38}$$

This is a 3D complex imaging space (x, y, y_1), which is the multiplication of a phase-encoding undistorted image (CTI) and a delta PSF. The delta PSF has no width but a shift with respect to the distortion in connecting the y and y_1 axes. In order to form 2D in-plane images, operations needed to be done, which are described as follows.

2.5.3.1 Reconstructing 2D Images from PSF-EPI

Specific information can be extracted from the 3D PSF-EPI data: 2D distorted image (EPI), 2D undistorted image (CTI), and the PSF. This thesis aims to achieve the undistorted image, while the distorted image is the original EPI image. In addition, the PSF describes the relation between distorted and undistorted images. In EPI, the PSF can be approximated

by a delta function and represents the image pixel shift if the relaxation effects are neglected. An inhomogeneous pixel shift in an image leads to the image distortion. The measured PSF can be used to correct the image distortion in EPI.

The operations to obtain the distorted image, undistorted image, and the PSF are derived below. Distorted and undistorted images can be obtained via the integration operations to the 3D PSF-EPI data. The distorted image at the $k_{\mathrm{y_1}}$ center ($k_{\mathrm{y_{1,c}}}$) can be obtained with the integration along the PSF phase encoding ($\mathrm{y_1}$):

$$\begin{aligned}\hat{\rho}(x, y, k_{y_{1,c}}) &= \int_{y_1} \hat{\rho}(x, y, y_1) dy_1 \\ &= \int_{y_1} \rho(x, y_1) \delta(y - y_1 - \frac{\Delta B(x, y_1) T_{\mathrm{esp}}}{\overline{G}_y \tau}) dy_1 \\ &= \rho(x, y - \frac{\Delta B(x, y) T_{\mathrm{esp}}}{\overline{G}_y \tau}).\end{aligned} \tag{2.39}$$

The obtained image shows the convolution of the physical spin density of a shifted delta PSF on the y-axis, which is exactly the estimated spin density in EPI (2.36), with the x-axis off-resonance omitted. On the other hand, by integrating along the EPI phase encoding (y), a 2D undistorted image can be obtained at the k_{y} center ($k_{\mathrm{y_{1,c}}}$).

$$\begin{aligned}\hat{\rho}(x, k_{y_c}, y_1) &= \int_{y} \hat{\rho}(x, y, y_1) dy \\ &= \int_{y} \rho(x, y_1) \delta(y - y_1 + \frac{\Delta B(x, y_1) T_{\mathrm{esp}}}{\overline{G}_y \tau}) dy \\ &= \rho(x, y_1) \cdot \mathrm{const.}\end{aligned} \tag{2.40}$$

This image is formed with the EPI readout x and the CTI phase-encoding $\mathrm{y_1}$, so there is no distortion. The constant is from the integral of the delta function. Finally, the PSF can be obtained by calculating the central mass of the delta PSF in either the y or $\mathrm{y_1}$ space.

2.5.3.2 PSF-EPI Sequence Acceleration along PSF Encoding y1

Acquiring 3D PSF-EPI data with the full PSF encoding is time-consuming. It requires $\mathrm{N_{y1}} \times$ TR of the ss-EPI, which is 8 minutes for the 160 PSF phase encodings and a 3 sec of TR. The sequence acceleration of PSF-EPI can be achieved by under-sampling the PSF encoding steps, which is similar to the in-plane parallel imaging acceleration PI. Because the under-sampled manner is skipping lines in the k-space, it results in the FoV reduction in the image space. As a result, the method is referred to as the reduced FoV (rFoV) acceleration. The acceleration capacity of rFoV is related to the PSF, thus the amount of distortion in EPI. Specifically, the minimum FoV in the PSF encoding dimension must be larger than the PSF to avoid aliasing artifacts:

$$FoV_{y_1} \geq \frac{2\Delta B(x,y_1)T_{\text{esp}}}{\overline{G}_y\tau} = \frac{\gamma}{2}\cdot FoV_y \cdot 2\Delta B(x,y_1)T_{esp}. \tag{2.41}$$

According to the equation, the FoV must be larger than the image distortion. Otherwise, an image aliasing shows up, similar to the Nyquist ghosting. Because the full FoV in the PSF phase encoding is set to the same as EPI phase encoding, the above condition can be rewritten to the maximum acceleration $\mathrm{R_{y_1}}$ as

$$R_{y_1} \equiv \frac{FoV_{y_1,full}}{FoV_{y_1}} \leq \frac{2\pi}{\gamma\cdot 2\Delta B(x,y_1)T_{esp}}. \tag{2.42}$$

Thus, the acceleration capacity of PSF-EPI is limited by the product of off-resonance and EPI echo spacing. The relation may also be written by the more straightforward relations in the unit of frequency or number of pixels

$$R_{y_1} \leq \frac{N_{y_1,full}BW_y}{2\delta f_{y_1}} = \frac{\delta y}{2N_{y_1,full}}, \tag{2.43}$$

where $\mathrm{N_{y1,full}\ BW_y = 1/T_{esp}}$ is the total receiving bandwidth in the EPI phase encoding, $\mathrm{N_{y1,full} = N_{y,full}}$ is the full phase-encoding sampling size, and the $\mathrm{\delta f_{y_1}}$ and $\mathrm{\delta f_y}$ are the off-resonance effects in the units of Hz or number of pixels. For example, the fat-water chemical shift has a 3.35 ppm spectrally difference in 1H MRI. Thus, the off-resonance effect is roughly 1 kHz at 7 T. For an EPI with an echo spacing of 0.8 ms, its total bandwidth in the EPI phase encoding is 1.25 kHz. As a result, the allowed PSF phase-encoding acceleration is 0.625, which is less than one; thus, no acceleration is available. Using an EPI in-plane GRAPPA factor of 4, the total bandwidth becomes 5 kHz, resulting in the maximum PSF acceleration of 2.5 or 64 PSF phase encoding steps (shots) without aliasing artifacts.

In the original multireference approaches, the measured PSF was used to correct the distortion in repetitive EPI imaging, e.g., in fMRI applications. The correcting performance of accelerated PSF-EPI was evidenced at 1.5 T to 7 T for the static off-resonance effects, e.g., 1.5 T for the water-fat chemical shift and air-tissue susceptibility [102], and at 3 T [103] and 7 T [104] for the air-tissue susceptibility. Correcting hundreds of EPI images using a 64-shot PSF-EPI reference scan that takes a few minutes is not a major issue in such an application.

However, when the PSF-EPI is used in the dMRI application, an extra dynamic off-resonance effect contributed by the eddy current must be accounted for. This is because DWI from different diffusion directions is achieved by varying the amplitudes of the physical gradients, and EPI is sensitive to the eddy current, producing extra distortions (see Section 2.5.2.4. As a result, the PSF-EPI reference scan needs to be acquired in each DWI with different diffusion directions. The long scan time of multiple PSF-EPI reference scans could be unrealistic if many b-values and directions are required.

2.5.4 View Angle Tilting EPI

VAT is a method to correct severe image distortion from static off-resonance effects. It applies a VAT gradient at the normally accessible z-axis simultaneously with the encoding gradient at the direction where the distortion is desired to be corrected. The VAT gradient can correct the off-resonance during sampling before the image forms (see Figure 3.2C). Thus, the image has no distortion.

VAT was originated to correct the distortion from air-tissue susceptibility and fat-water chemical shift in CSE at 1.5 T. Later, VAT was also evidenced to TSE to correct the severe image distortion of metal-tissue susceptibility in TSE at 3 T and fat-water chemical shift in EPI at 3 T. However, VAT-EPI has a fatal flaw of image blurring. The blurring was very severe, so it was used very little, even though it has a great capacity for distortion correction. Below, the principle and the amount of blurring generated by VAT-EPI will be derived. Because the blurring of VAT-EPI is critically related to the capacity of acceleration in the proposed sequence, the quantity must be known.

Starting from the 2D Cartesian blipped EPI signal equation with the off-resonance effects ΔB(x,y) appearance, as in the Section 2.5.2. For simplicity, the readout off-resonance term is again omitted due to the typical use of high readout bandwidth in EPI. The compensation VAT gradient G_{VAT} is applied to EPI along the z dimension, making its timing and duration identical to the EPI blipped phase-encoding gradient $\bar{G}_y$. Then, the signal equation of VAT-EPI may written as

$$\begin{aligned} S(k_x, k_y) = \int_x \int_y \int_{z+L_c(x,y)} \rho(x,y,z) e^{-2\pi i (k_x \cdot x + k_y \cdot y + \frac{\gamma}{2\pi} G_{VAT} \tau \cdot z)} \\ e^{-2\pi i (k_y \cdot \frac{\Delta B(x,y) T_{esp}}{\bar{G}_y \tau})} \, dx \, dy \, dz, \end{aligned} \tag{2.44}$$

where L_c(x,y) is the slice position variation due to off-resonance effects. Changing the variable z = z' - L_c(x,y) = z' - ΔB(x,y)/G_z is equivalent to transforming the slice plane to an off-resonance corrected plane [89, 90]. The signal equation of VAT-EPI may be rewritten as

$$\begin{aligned} S(k_x, k_y) &= \int_x \int_y \int_{z*} \rho(x,y,z' - \frac{\Delta B(x,y)}{G_z}) e^{-2\pi i (k_x \cdot x + k_y \cdot y + \frac{\gamma}{2\pi} G_{VAT} \tau \cdot (z' - \frac{\Delta B(x,y)}{G_z}))} \\ &\quad e^{-2\pi i (k_y \cdot \frac{\Delta B(x,y) T_{esp}}{\bar{G}_y \tau})} |J(x,y)| \, dx \, dy \, dz' \\ &= \int_x \int_y \int_{z*} \rho(x,y,z' - \frac{\Delta B(x,y)}{G_z}) e^{-2\pi i (k_x \cdot x + k_y \cdot y + k_y \cdot \frac{\Delta B(x,y)}{\bar{G}_y} (\frac{G_{VAT}}{G_z} - \frac{T_{esp}}{\tau}))} \\ &\quad e^{-2\pi i (\frac{\gamma}{2\pi} G_{VAT} \tau \cdot z')} |J(x,y)| \, dx \, dy \, dz'. \end{aligned} \tag{2.45}$$

If the VAT gradient is optimized to $G_{VAT} = G_z T_{esp}/\tau$, the off-resonance term along EPI

phase-encoding can be eliminated. Thus, there is no image distortion in VAT-EPI. Note that Jacobian J(x,y) = ∂z/∂z' = 1, the above equation can be further simplified as

$$\begin{aligned} S(k_x, k_y) &= \int_x \int_y \int_{z*} \rho(x, y, z' - \frac{\Delta B(x,y)}{G_z}) e^{-2\pi i(k_x \cdot x + k_y \cdot y + \frac{\gamma}{2\pi} G_{VAT} \tau \cdot z')} \, dx \, dy \, dz' \\ &= L \cdot SINC(\gamma G_{VAT} \tau \frac{L}{2}) \int_x \int_y \rho(x, y, z'_0 - \frac{\Delta B(x,y)}{G_z}) e^{-2\pi i(k_x \cdot x + k_y \cdot y)} \, dx \, dy, \end{aligned} \tag{2.46}$$

where SINC is the (unnormalized) sinc function and is defined as SINC(x) = sin(x)/x. It can be readily seen that the VAT gradient voids the EPI phase-encoding off-resonance term and adds a new SINC term. However, if $G_{VAT} \neq G_z T_{esp}/\tau$, the off-resonance effects remain with the amount is proportional to $|G_{VAT} - G_z T_{esp}/\tau|$. This means that the optimized VAT gradient amplitude is not a lower limit but an exact value. Equivalently, it says that if $G_{VAT} > G_z T_{esp}/\tau$, the off-resonance will not be minimized but rise again with an opposite polarity.

As in previous sections, the estimated spin density of VAT-EPI with an optimal VAT gradient can be obtained via the Fourier inversion of the signal equation

$$\begin{aligned} \hat{\rho}(x, y) &= \int_{k_x} \int_{k_y} S(k_x, k_y) e^{+2\pi i(k_x \cdot x + k_y \cdot y)} \, dk_x \, dk_y \\ &= \rho(x, y, z' - \frac{\Delta B(x,y)}{G_z}) * \int_{k_x} \int_{k_y} L \cdot SINC(2\pi k_y \frac{G_{VAT}}{\overline{G}_y} \frac{L}{2}) e^{+2\pi i(k_x \cdot x + k_y \cdot y)} \, dk_x \, dk_y \\ &= \rho(x, \frac{1}{\frac{G_{VAT}}{\overline{G}_y} \frac{L}{2}} RECT(\frac{y}{\frac{G_{VAT}}{\overline{G}_y} \frac{1}{2}}), z_0^* - \frac{\Delta B(x,y)}{G_z}) \\ &= \rho(x, y, z_0^* - \frac{\Delta B(x,y)}{G_z}) * \frac{1}{\frac{G_{VAT}}{\overline{G}_y} \frac{1}{2}} RECT(\frac{y}{\frac{G_{VAT}}{\overline{G}_y} \frac{L}{2}}), \end{aligned} \tag{2.47}$$

where the RECT function is the rectangular function, which is defined as

$$A \cdot RECT(x/W) = \begin{cases} A, & \text{for } |x| \leq W/2 \\ 0, & \text{otherwise} \end{cases}, \tag{2.48}$$

with amplitude A and width W. The convolution of in-plane distortion-corrected spin density with RECT PSF leads to blurring in the y dimension of VAT-EPI but no distortion. Note that the delta PSF in the ordinary EPI is $\delta(y - \Delta B(x,y) T_{esp}/\bar{G}_y \tau)$. The blurring of VAT-EPI may be characterized by

$$\frac{G_{VAT}}{\overline{G}_y} \frac{L}{2} \text{ in length or } \frac{G_{VAT}}{\overline{G}_y} \frac{L/2}{\Delta y} \text{ in pixel,} \tag{2.49}$$

where Δy is the spatial resolution in the VAT-EPI phase-encoding dimension.

A property of the RECT PSF is that whenever the width of a rectangular function goes to zero, it becomes a Dirac delta function without shift

$$\delta(x) = \lim_{W \to 0} A \cdot RECT(\frac{x}{W}). \tag{2.50}$$

Thus, with a smaller PSF width generated from VAT, the estimated spin density can be approximated to the undistorted image and not blur as CTI. Recall the relation of VAT gradient and slice thickness $G_{VAT} = G_z T_{esp}/\tau \propto BW_z T_{esp}/L\tau$. A thin slice was said to lead to a high VAT gradient amplitude due to the high slice-selective gradient amplitude when the RF bandwidth is fixed [90]. However, the PSF width is a product of the VAT gradient ratio and slice thickness from the above derivation. Thus, the contribution of slice thickness is canceled, and no extra blurring is produced from the slice thickness change. Another property of the RECT PSF is that the signal is proportional to the slice thickness but not the VAT gradient ratio (i.e., G_{VAT}/G_y) because of the cancellation of the outside and inside the RECT parentheses (see Equation 2.47).

Instead of applying the VAT gradient to the phase encoding in VAT-EPI, the VAT gradient is applied to the readout direction for VAT-CSE or VAT-TSE. As a result, the gradient ratio (G_z/G_{RO}) is ≈ 1.0, and the image blurring is minor. However, the gradient ratio in VAT-EPI is ($G_z/G_{y'}$). The ratio is generally greater than 1.0 and can be as large as more than 10. Thus, VAT-EPI suffers from image blurring. This means the signal strength of VAT-EPI is not changed by the VAT gradient amplitude but by the slice thickness, as EPI. It was evidenced that the PI can reduce the image blurring due to the reduction of T_{esp}. However, there was no attempt at the ultrahigh field because of the considerable blurring.

Combining VAT-EPI and PSF-EPI is intriguing for the current thesis because both methods can effectively correct severe image distortion. In addition, although not described, the PSF-EPI can also correct the neglected small image blurring from T_2* in EPI. Knowing if the PSF-EPI can correct the even worse blurring in VAT-EPI may be desired. On the other hand, completely correcting the distortion in VAT-EPI may accelerate the PSF-EPI further. In the following chapter, the theory of the combined method will be derived, and the experiments will be done to evaluate the performance at a whole-body 7 T human scanner, which will eventually be applied to the dMRI.

3 View-angle Tilting Point-spread Function Mapping EPI

The work presented in this chapter has been partly published in the following articles:

1. **Y.-H. Tung** and O. Speck, "Distortion correction at the ultrahigh field: Benefit of deviation from "best" VAT," ESMRMB, 2023.
2. **Y.-H. Tung** and O. Speck, "VAT: Harnessing Eddy Currents to Correct Distortions in EPI," DS-ISMRM, 2023.
3. **Y.-H. Tung**, M.-H. In, S. Ahn, O. Speck, "Rapid Geometry-Corrected Echo-Planar Imaging at Ultra-High Field - Fusing View Angle Tilting and Point-Spread Function Mapping," Magnetic Resonance in Medicine, 2022.
4. **Y.-H. Tung**, M,-H. In, O. Speck, "Isotropic High-Resolution DIADEM-VAT at UHF," ESMRMB, Rotterdam, Netherlands, 2019.
5. **Y.-H. Tung** et al., "Accelerated Distortion-Free Diffusion Imaging at 7T - by Fusing PSF and VAT," ISMRM-ESMRMB, Paris, France, 2018.

The previous chapter explicitly discussed two EPI variations, PSF-EPI and VAT-EPI, that will be fused to form a new sequence: VAT-PSF-EPI. On the one hand, the connection between CTI and EPI through a PSF is in the phase-encoding direction in which PSF-EPI was derived. The PSF is used to correct image distortion in EPI, resulting in high imaging fidelity similar to CTI. However, the imaging speed of PSF-EPI is limited at the ultrahigh field due to its dependency on PSF displacement. On the other hand, VAT-EPI is a technique that corrects EPI in-plane image distortion without showing B_0 dependency. It can correct severe distortion from different static off-resonance sources but is limited by image blurring. As a whole new sequence aiming for ultrahigh field dMRI, the sensitivity of VAT-PSF-EPI to major sources of off-resonance effects needs to be studied.

In MRI, placing an object into the static magnetic field (B_0 field) will lead to the field deviation from the original uniform field. The spins that proceed with the RF-excited Larmor frequency are called on-resonant spins. Whenever an effect produces field perturbation that adds an extra field to the spin, the spin can deviate from the Larmor

frequency. The effect is called the off-resonance effect (see also Section 2.2 for more detail). It can be imagined that whenever the spins' spatial locations are frequency encoded, the off-resonance effects lead spins to experience frequency change. Suppose the field deviation is not adequately dealt with, and the image is reconstructed straightforwardly with the Fourier transform. In that case, the spins will end up in a different location than the actual physical location, resulting in image signal variation (signal loss or pile-up) and geometric distortion. Magnetic field perturbation sources can be divided into static and dynamic off-resonance effects. The static off-resonance effects do not change if the imaging sequence runs repeatedly. They include slice-selective gradient nonuniformity, object-independent field inhomogeneity, susceptibility variation, and chemical shift. In contrast, the dynamic off-resonance effects change dynamically during repeated imaging. The object-magnet relative movement and the diffusion gradients induced eddy current are included. This thesis will focus on correcting the signal variation and geometric distortion on the most common static and dynamic off-resonance effects in dMRI by proposing the fast sequence VAT-PSF-EPI. In addition, the gradient nonuniformity and object-magnet relative movement are excluded from the current study.

The susceptibility variation is one of the major static off-resonance effects in dMRI at the ultrahigh field and should be dealt with by the proposed sequence. It changes linearly with the main magnetic field strength, making them especially pronounced at the ultrahigh field (see Section2.2.2) and thus producing noticeable image distortion in EPI (see Section 2.5.2.3). Among the susceptibility variation in the human 1H MRI, air-tissue susceptibility has the most significant difference, e.g., $\Delta\chi$ (sinus-tissue) = $+9.2 \pm 1.3$ ppm in the head. The susceptibility variation is hardly eliminated even after the higher-order B_0 field shimming. For a more realistic estimation, the susceptibility is shape-dependent and can be modeled as an ellipsoid for human subjects. The maximum field deviation of $3/4{\cdot}\Delta\chi$ at the poles and $1/4{\cdot}\Delta\chi$ at the equator are taken. Therefore, the general position error can be varied from the range of $1/4{\cdot}\Delta\chi$ to $3/4{\cdot}\Delta\chi$ depending on the position of the ellipsoid. From the above estimate, the position error range is from 674 Hz to 2023 Hz due to the air-tissue susceptibility effect of 1H MR imaging at 7 T. In practice, however, the signal from the highest position errors are very localized to a few pixels and are possibly not excited correctly in the slice selection due to the finite RF bandwidth. As a result, these pixels are mostly dephased and not shown in the image of EPI. Nevertheless, it should first be tested to determine whether the VAT-PSF-EPI can correct the susceptibility distortion at the ultrahigh field with the available acceleration. The produced undistorted image will be compared with EPI, VAT-EPI, and PSF-EPI.

In many circumstances, there is not only one chemical substance within the object. If more than one chemical substance has a proton resonance signal, those protons' resonance frequencies may differ. This frequency difference is called a chemical shift (see Section 2.2.1). The chemical shift is measured in the ppm and is independent of the applied magnetic

field. For example, one of the frequent proton chemical shifts in human measurement is the fat-water chemical shift. Fat (more generally, lipid) has 10 proton resonance frequencies. The most prominent signal comes from the methylene protons group, which has the absolute chemical shift of 1.31 ppm, where 0 ppm is referenced to the TMS. In contrast, protons in water have the same absolute chemical shift of 4.65 ppm. Thus, fat and water's chemical shift difference ($\delta_{\text{fat -water}}$) is 3.35 ppm. The frequency difference between fat and water is a scaling of the main magnetic field. As a result, the fat-water chemical shift at 1.5 T ($\omega_0 \approx 64$ MHz) is 220 Hz, at 3.0 T ($\omega_0 \approx 128$ MHz) is 440 Hz, and at 7 T ($\omega_0 \approx 300$ MHz) is 1000 Hz, thus the position error is huge in EPI (see Section 2.5.2.3). It is interesting to know whether the VAT-PSF-EPI can simultaneously correct the susceptibility and chemical shift, similar to VAT-EPI at 3 T [90], but without image blurring.

The eddy current distortion must be evaluated when EPI applies diffusion gradient in dMRI. In principle, eddy currents generated with positive and negative polarities of gradient switching have chances to cancel each other (see Section2.2.3). However, with more gradients involved, eddy current's multiple-time constant delays and residual cancellation characteristics are complex. Fortunately, the behavior of eddy current residual can be simulated numerically. With the target MR system's knowledge, the required total diffusion time and eddy current residual for given b-values can be realized. In particular, the simplest diffusion gradient waveform (Stejskal-Tanner [56]) contains two unipolar gradients has a larger residue that produces apparent distortion in EPI (see 2.5.2.4). It needs to compare with the commonly used eddy current null sequence twice refocusing spin echo (TRSE) [41] at 3 Tesla and below. TRSE is the combination of dual bipolar gradients [105] and an additional refocusing RF pulse. The added second refocusing RF pulse with unequal gradient durations makes TRSE possible to null a chosen eddy current time constant and to increase the diffusion weighting efficiency.

It is desired to know how much image distortion in EPI and VAT-PSF-EPI is related to the system-specific eddy current simulation. In particular, the TRSE produces a much smaller residual than the Stejskal-Tanner waveform. However, the TRSE needs a much longer diffusion time than Stejskal-Tanner, i.e., around 20 ms more with EPI partial Fourier 6/8. Long TE is particularly undesired at ultrahigh fields due to the shorter apparent T_2 relaxation time. In addition, using the second refocusing RF leads TRSE to be prone to the B_1 sensitivity and SAR increase. Therefore, Stejskal-Tanner combined with post-processing is the common approach in the ultrahigh field. For comparison, VAT-PSF-EPI is combined with Stejskal-Tanner to keep the low TE benefits and examine its performance in correcting the higher eddy current residual.

The overall performance of VAT-PSF-EPI in the capacity of acceleration, correcting distortions, and blurring in dMRI is fascinating and will finally be tested *in vivo* at an ultrahigh field. Although no other method has been able to correct all these artifacts in

EPI so far, it is interesting to compare the proposed sequence with the other established methods of partial correction, such as the common multi-shot EPI and the post-processing distortion correction methods.

The study observed two primary limitations of the proposed VAT-PSF-EPI as a dMRI sequence: SNR and the faint fat signal from EPI Nyquist ghost and through-plane distortion. Specifically, the SNR reduction mechanism and its optimization will be described in detail. Meanwhile, the fat artifacts described have had no method to deal with them. To avoid confounding the pathological effects of human DWI, a method to suppress these fat artifacts needs to be investigated. Since the VAT-PSF-EPI is robust in correcting all spectral ranges of EPI in-plane distortion, a general approach is desired instead of the spectral approaches described in Section 2.5.2.3. One approach that may be compatible with VAT-PSF-EPI is the differencing RF method [97], which uses different RF bandwidths for spin-echo excitation and refocusing pulses. The method can select a desired resonance frequency range to be refocused. The original approach either extends the excitation or refocusing duration to reach the desired fat suppression effect. In the current study, a reduction of RF duration is desired rather than an extension to reduce the TE.

This chapter will be configured by establishing the theory of VAT-PSF-EPI and experimenting with correcting the air-tissue susceptibility at a whole-body 7 T human scanner. Three experiments containing partially overlapping VAT gradient amplitude (view-tilting angles) are firstly designed to separate MR parameters' contributions in VAT-EPI. Each experiment measures the full PSF sampling to characterize the image distortion and blurring in VAT-EPI and compare those with EPI. Because the acceleration of the distortion-corrected sequence VAT-PSF-EPI is closely connected to the VAT-EPI, the maximum applicable acceleration factor of VAT-PSF-EPI is examined by retrospective simulation and finally compared the image quality and accelerations with PSF-EPI.

Next, the performance of chemical shifts on top of susceptibility distortion will be studied in phantom and *in vivo* T_2W images. The image blurring shall also be corrected. The effectiveness and robustness of correction via VAT-PSF-EPI will be examined with its acceleration capacity and compared with traditional PSF-EPI *in vivo* T_2W images.

After that, the eddy current residual with the common Stejskal-Tanner and eddy current nulled TRSE diffusion gradient waveforms will be numerically simulated and evaluated experimentally in EPI. Stejskal-Tanner VAT-PSF-EPI will be tested with a series of b-values by up to 3000 s/mm^2 and compared with the established distortion correction methods qualitatively and quantitatively, which are TRSE ss-EPI and Stejskal-Tanner ss-EPI with post-processing correction methods.

Moreover, VAT-PSF-EPI will be examined *in vivo* high-resolution dMRI. By far, no EPI method has been evidenced to correct air-tissue susceptibility-induced distortion, fat-water chemical shift, and high b-value diffusion gradient-induced in-plane distortion at once. The VAT-PSF-EPI aims to address these issues. The image fidelity and imaging speed

of VAT-PSF-EPI will be compared to PSF-EPI, VAT-EPI, and other available partial correcting methods.

Finally, the limitations of VAT-PSF-EPI will be investigated, and improvements will be made to perform the even faster high-resolution *in vivo* dMRI without the artifacts.

3.1 Theory

The signal equation of VAT-PSF-EPI may be formed by adding the PSF encoding k_{y_1} to the y-axis of the VAT-EPI signal equation in Equation 2.46:

$$S(k_x, k_y, k_{y_1}) = L \cdot SINC(\gamma G_{VAT} \tau \frac{L}{2}) \int_x \int_y \rho(x, y, z_0^* - \frac{\Delta B(x,y)}{G_z}) e^{-2\pi i (k_x \cdot x + (k_y + k_{y_1}) \cdot y)} \, dx \, dy. \tag{3.1}$$

Rewriting the SINC term with respect to EPI phase-encoding k_y (i.e., $k_y = \int_0^\tau \overline{G}_y \, dt$), the estimated spin density of VAT-PSF-EPI can be obtained by applying a 3D inverse Fourier transform with respect to k_x, k_y and k_z

$$\begin{aligned}
\hat{\rho}(x, y, y_1) &= \int_{k_{y_1}} \int_{k_y} \int_{k_x} S(k_x, k_y, k_{y_1}) e^{+2\pi i (k_x \cdot x + k_y \cdot y + k_{y_1} \cdot y_1)} \, dk_x \, dk_y \, dk_{y_1} \\
&= \int_{k_{y_1}} \int_{k_y} L \cdot SINC(2\pi k_y \frac{G_{VAT}}{\overline{G}_y} \frac{L}{2}) \int_{k_x} \{ \int_{y'} \int_{x'} \rho(x', y', z_0^* - \frac{\Delta B(x', y')}{G_z}) \\
&\quad e^{-2\pi i (k_x \cdot x' + (k_y + k_{y_1}) \cdot y')} \, dx' \, dy' \} e^{+2\pi i (k_x \cdot x + k_y \cdot y + k_{y_1} \cdot y_1)} \, dk_x \, dk_y \, dk_{y_1} \\
&= \int_{k_y} L \cdot SINC(2\pi k_y \frac{G_{VAT}}{\overline{G}_y} \frac{L}{2}) \int_{y'} \int_{x'} \rho(x', y', z_0^* - \frac{\Delta B(x', y')}{G_z}) \\
&\quad \int_{k_x} e^{+2\pi i (k_x \cdot (x - x'))} \, dk_x \int_{k_{y_1}} e^{+2\pi i (k_{y_1} \cdot (y_1 - y'))} \, dk_{y_1} e^{+2\pi i (k_y \cdot (y - y'))} \, dx' \, dy' \, dk_y \\
&= \int_{k_y} L \cdot SINC(2\pi k_y \frac{G_{VAT}}{\overline{G}_y} \frac{L}{2}) \int_{y'} \int_{x'} \rho(x', y', z_0^* - \frac{\Delta B(x', y')}{G_z}) \\
&\quad \delta(x' - x) \delta(y' - y_1) e^{+2\pi i (k_y \cdot (y - y'))} \, dx' \, dy' \, dk_y \\
&= \rho(x, y_1, z_0^* - \frac{\Delta B(x, y_1)}{G_z}) \int_{k_y} L \cdot SINC(2\pi k_y \frac{G_{VAT}}{\overline{G}_y} \frac{L}{2}) e^{+2\pi i (k_y \cdot (y - y_1))} \, dk_y \\
&= \rho(x, y_1, z_0^* - \frac{\Delta B(x, y)}{G_z}) \frac{1}{\frac{G_{VAT}}{\overline{G}_y} \frac{1}{2}} RECT(\frac{y - y_1}{\frac{G_{VAT}}{\overline{G}_y} \frac{L}{2}}).
\end{aligned} \tag{3.2}$$

This is a 3D complex image space (x,y,y_1) with the product of the in-plane undistorted image to a RECT PSF connecting EPI phase-encoding y and PSF encoding y_1. The pulse sequence of VAT-PSF-EPI is shown in Figure 3.1, which is formed by adding the VAT (red) and PSF gradients (blue) to a spin-echo EPI.

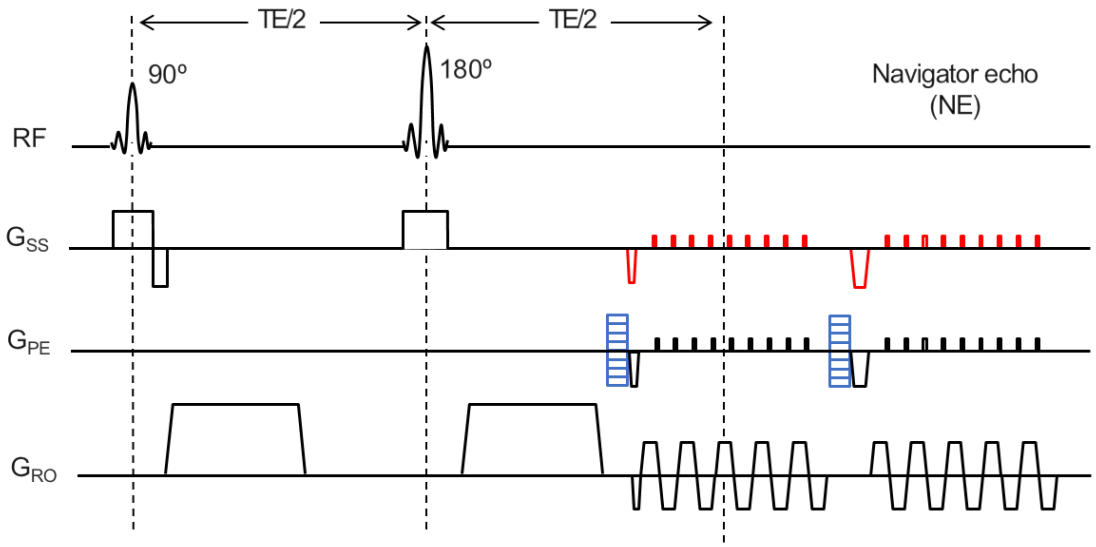

Figure 3.1: Pulse sequence of VAT-PSF-EPI. Red: VAT gradient, blue: PSF encoding gradient. The sequence is based on the spin-echo EPI; the trapezoidal gradients before and after the 180 refocusing pulse are the Stejskal-Tanner diffusion gradient. The navigator echo is for the motion correction in between multi-shots.

3.1.1 Reconstructing 2D Images from VAT-PSF-EPI

The VAT-PSF-EPI signal equation can be examined by deriving the distorted image (VAT-EPI) and undistorted reference image (CTI) from integrating the y_1 or y dimension, similar to Section 2.5.3.1. With the integration of VAT-PSF-EPI along the y_1 dimension, the distorted image at the k_{y_1} center ($k_{y_{1,c}}$) is

$$\begin{aligned}\hat{\rho}(x, y, k_{y_{1,c}}) &= \int_{y_1} \hat{\rho}(x, y, y_1) dy_1 \\ &= \int_{y_1} \rho(x, y_1, z_0^* - \frac{\Delta B(x,y)}{G_z}) \cdot \frac{1}{\frac{G_{VAT}}{G_y}\frac{1}{2}} RECT(\frac{y - y_1}{\frac{G_{VAT}}{G_y}\frac{L}{2}}) dy_1 \\ &= \rho(x, y, z_0^* - \frac{\Delta B(x,y)}{G_z}) * \frac{1}{\frac{G_{VAT}}{G_y}\frac{1}{2}} RECT(\frac{y}{\frac{G_{VAT}}{G_y}\frac{L}{2}}).\end{aligned} \tag{3.3}$$

This obtained image is the same as VAT-EPI (see 2.5.4), which verifies the VAT-PSF-EPI signal equation. Similarly, with the integration along the y dimension, an undistorted and not blurred image at k_y center (k_{y_c}) can be obtained. The estimated spin density is written as

$$\begin{aligned}\hat{\rho}(x, k_{y_c}, y_1) &= \int_y \hat{\rho}(x, y, y_1) dy \\ &= \rho(x, y_1, z_0^* - \frac{\Delta B(x, y_1)}{G_z}) \int_y \frac{1}{\frac{G_{VAT}}{G_y}\frac{1}{2}} RECT(\frac{y - y_1}{\frac{G_{VAT}}{G_y}\frac{L}{2}}) dy \\ &= \rho(x, y_1, z_0^* - \frac{\Delta B(x, y_1)}{G_z}) \cdot \text{const.}\end{aligned} \tag{3.4}$$

This undistorted image is modulated with a constant from the PSF integral at the k_{y_c}. It is similar to the undistorted image in PSF-EPI, except the integral of RECT has a finite slope instead of an infinite slope at slice boundaries.

3.1.2 VAT-PSF-EPI Sequence Acceleration along PSF encoding y1

Similar to the acceleration in PSF-EPI, it is possible to accelerate VAT-PSF-EPI with the same rFoV method. As mentioned in Section 2.5.3.2, the acceleration capability in PSF-EPI is inversely proportional to EPI distortion or PSF displacement, which is the product of the off-resonance field and EPI echo spacing, i.e., $R_{y_1} \propto 1/\Delta B(x,y_1) T_{esp}$. For VAT-PSF-EPI, the acceleration dependence of T_{esp} remains the same but with a multiplication of RF bandwidth instead of image distortion because of a different PSF shape. The minimum FoV for unfolding the accelerated image without aliasing artifacts may be written as

$$FoV_{y_1} \geq \frac{G_{VAT}}{\overline{G}_y} L = \frac{L G_z T_{esp}}{\overline{G}_y \tau} = FoV_y \cdot BW_z \cdot T_{esp}, \tag{3.5}$$

where BW_z is RF-excitation bandwidth. Similarly, because the full FoV coverage in the PSF phase encoding dimension is set the same as EPI phase-encoding FoV, the above equation can be rendered as the maximum acceleration factor for the optimal VAT gradient

$$R_{y_1} \equiv \frac{FoV_{y_1}, full}{FoV_{y_1}} \leq \frac{1}{BW_z T_{esp}} = \frac{N_{y_1, full} BW_y}{BW_z}. \tag{3.6}$$

The schematic diagram of the VAT-PSF-EPI is plotted in Figure 3.2. The image formation and image acceleration of VAT-PSF-EPI are depicted and compared with EPI, VAT-EPI, and PSF-EPI. In Figure 3.2A, EPI distortion shows up because of the appearance of the off-resonance effects and the image formed after the linear slice selection and EPI phase encoding. In Figure 3.2B, PSF-EPI can map the PSF information before the image is formed and correct the image distortion later in the image domain. However, the imaging speed of PSF-EPI is inversely proportional to the image distortion, thus very slow whenever the distortion is significant. In Figure 3.2C, the VAT gradient can correct the image distortion during EPI phase encoding. However, the image blurring shows up in the final VAT-EPI image. In Figure 3.2D, VAT-PSF-EPI uses VAT to correct the

significant distortion, and the image blurring is corrected via PSF mapping at the same time. Therefore, the final image has the same fidelity as PSF-EPI and can be scanned much faster.

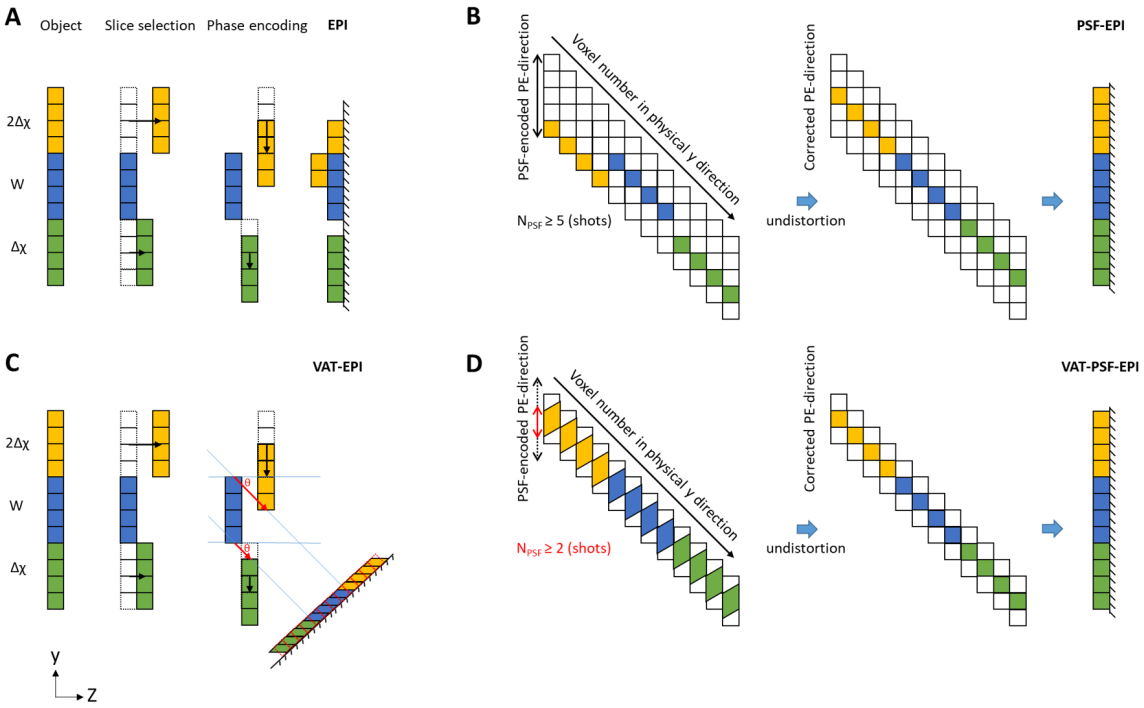

Figure 3.2: Image formation of VAT-PSF-EPI. A: EPI, B: PSF-EPI, C: VAT-EPI, D: VAT-PSF-EPI. In EPI, the in-plane image distortion and intensity abnormal are due to the frequency encoding in the slice selection and (echo train) phase encoding directions. In PSF-EPI, the applied PSF encoding captures the PSF shift in EPI and corrects the image distortion. In VAT-EPI, the gradient is tilted at a particular angle, correcting the image distortion in EPI while generating image blurring. In VAT-PSF-EPI, the image distortion is corrected by the VAT, while the generated blurring is captured and corrected by the PSF encoding. Imaging acceleration in VAT-PSF-EPI is realized by the generated blurring of VAT less than the amount of EPI distortion.

3.2 Methods

All experiments were acquired with the prototype VAT-PSF-EPI sequence at a whole-body 7 T MR scanner (Siemens Healthineers, Erlangen, Germany) using a 32-channel head coil (Nova Medical, Wilmington, United States). The gradient coil is SC72 with a maximum strength of 70 mT/m and a maximum slew rate of 200 T/m/s.

3.2.1 Assessment of Susceptibility Distortion Correction: Comparison of Full PSF Sampled VAT-PSF-EPI and PSF-EPI

A structured phantom filled with pure silicone oil (QUAX, Obernburg, Germany) was used to study the susceptibility-induced distortion correction of VAT-PSF-EPI. Silicone oil (Polydimethylsiloxane [PDMS]) is a clear and transparent liquid that has a magnetic susceptibility close to water (difference < 1 ppm) in the 1H MRI, making it a suitable phantom material to study air-tissue susceptibility distortion. Although the silicone oil has a chemical shift of 3.02 ppm away from water, the MR central resonance frequency was automatically tuned to the pure silicone oil. Thus, no chemical shift should appear.

The MR imaging protocol acquired fully PSF-sampled VAT-PSF-EPI data with three GRAPPA factors, slice thicknesses, and RF combinations (90°and 180°RF kept the same). The standard imaging parameters were set: in-plane spatial resolution = 1.4 mm (160 shots, $R_{PSF} = 1$), and readout receiver bandwidth = 1953 Hz/pixel, EPI echo-spacing = 0.8 ms, TR/TE = 3000/200 ms. Except for being variable, the following parameters were set to the same: GRAPPA = 2 (ETL = 80), slice thickness = 1.4 mm, and RF time-bandwidth product (TBP) = 2.62, RF duration = 20 ms. For the first experiment, the GRAPPA factors changed in GRAPPA 1 (ETL = 160), GRAPPA 2 (ETL = 80), and GRAPPA 4 (ETL = 40) to examine the proportionality of distortion and blurring amount to GRAPPA factors. For comparison, PSF-EPI (without VAT gradient) was also acquired using the same GRAPPA factors. The corresponding VAT gradient amplitude (view-tilting angles) of VAT-PSF-EPI was 16.35 (86.5°) for GRAPPA 1, 8.17 (83.0°) for GRAPPA 2, and 4.08 (76.2°) for GRAPPA 4. In the second experiment, the slice thickness changed to 0.7 mm, 1.4 mm, and 2.8 mm to examine the blurring amount in the VAT-EPI theory of VAT gradient amplitude overlapping. The VAT gradient amplitude (view-tilting angles) was 16.35 (86.5°) for 0.7 mm, 8.17 (83.0°) for 1.4 mm, and 4.08 (76.2°) for 2.8 mm. In the last experiment, the RF TBP and duration changed by 2.616/20 ms, 1.962/15 ms, and 1.308/10 ms to examine whether the blurring amount maintained the constant. The VAT gradient amplitude (view-tilting angle) was the same for all RF combinations at 8.17 (83.0°).

All data was carried out in three analyses using MATLAB (Mathworks, Middlesex, United States): PSF map calculation, retrospective simulation for the maximum applicable rFoV factors (PSF acceleration factors, R_{PSF}), and the signal modulation profile measurement. As shown in Figure 3.3, the standard EPI preprocessing, including 1D Nyquist ghost correction, readout ramp-sampling correction, and GRAPPA reconstruction, was performed slice by slice starting from the raw data. After the preprocessing, 3D k-space data (k_x, k_y, k_{y_1}) with all coil channel data were obtained. Several inverse Fourier transforms were then done for the targeting analysis differently and will be described below in each analysis. After the Fourier transformations, the coil combination was done

with the square root sum-of-square to obtain the magnitude images.

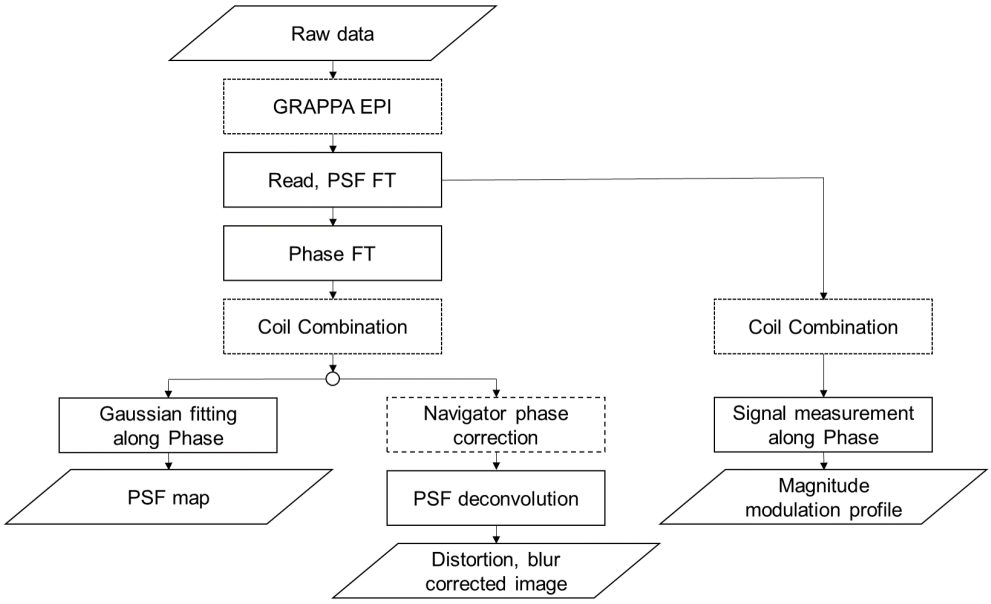

Figure 3.3: Image processing of VAT-PSF-EPI. The PSF map, distortion and blurring corrected and uncorrected images and the magnitude modulation profile can be obtained in the same data set. The dashed box is omitted for the single-channel Rx coil.

The first analysis was the PSF map calculation. After the preprocessing steps, 3D inverse Fourier transforms along the readout (k_{x}), EPI phase encoding (k_{y}), and PSF phase encoding ($k_{\mathrm{y_1}}$) directions were performed (see Figure 3.3). Afterward, voxel-wised 1D Gaussian fitting ($\mathrm{y_1}$) along the EPI phase encoding direction looped each readout pixel to calculate the PSF displacement and the PSF width. The PSF displacement was determined via the Gaussian peak shift relative to the pixel number of the PSF phase encoding direction. At the same time, the PSF width was determined by the full width at the tenth maximum (FWTM) of the Gaussian peak. The PSF range was defined in addition to the absolute PSF displacement and width value. Because the pixels of the highest PSF range contribute to the highest aliasing artifact, the final PSF values were determined by the median of the highest 28 pixels (around 0.5%) of the PSF range within each image slice.

The second analysis was the maximum rFoV factors examination. After the preprocessing, the rFoV acceleration was retrospectively simulated by keeping one line for every number of rFoV lines in the k-space of the PSF encoding ($k_{\mathrm{y_1}}$). For example, the rFoV factor of 2 is to skip every line in k_{y}. The 3D Fourier transform to readout (k_{x}) and phase encoding directions (k_{y} and $k_{\mathrm{y_1}}$) were then performed, and finally, using the rFoV unfolding to obtain the distortion and blurring corrected images (x, $\mathrm{y_1}$) in the image domain. The maximum rFoV factor was determined by the highest rFoV acceleration with less than

10% aliasing artifact signal compared with the signal from the same position in the main image.

The last analysis was the signal modulation profile measurement. Only 2D inverse Fourier transformation to readout (k_{x}) and PSF phase encoding ($k_{\mathrm{y_1}}$) directions were performed after the preprocessing. The signal was measured with the same region of interest at the phantom along the EPI phase encoding direction (x, k_{y}, $\mathrm{y_1}$) for all the acquired data. The central peak width was determined by its first derivative to determine the modulation width.

3.2.2 Assessment of Susceptibility and Chemical shift Distortion Correction

This assessment measured a homemade phantom and an *in vivo* human subject. The phantom was made with a cylindrical phantom consisting of six steady inner tubes in a wide-mouth bottle to examine the susceptibility and chemical shift distortion correction, as shown in Figure 3.4. Three large tubes were filled with air, vegetable oil (rapeseed oil), and tap water. The three small tubes (outer diameter 13 mm) were all filled with tap water, together with the large tubes (outer diameter 25 mm) immersed into the tap water-filled outer cylinder (outer diameter 60 mm). Vegetable oil has 10 proton resonance frequencies similar to those of human lipids. Moreover, the oil-water susceptibility is 1.05 ppm, less than the air-water susceptibility of 9.41 ppm. Therefore, the phantom is a good mimic of body fat in investigating both distortions.

For the phantom imaging, 1.4 mm isotropic spatial resolution and 31 axial slices with anterior-posterior phase encoding direction of $\mathrm{T_2}$-weighted images were acquired by ss-EPI, TSE, and VAT-PSF-EPI sequences. The other imaging parameters were set as follows, ss-EPI: readout receiving bandwidth = 1488 Hz/pixel, GRAPPA = 4, TR/TE = 6300/65 ms, TA = 6.3 s; TSE: readout receiver bandwidth = 789 Hz/pixel, GRAPPA = 4, turbo factor = 8, TR/TE = 8040/68 ms, TA = 1:04 min; VAT-PSF-EPI: readout receiving bandwidth = 1838 Hz/pixel, ETL = 30 (GRAPPA $\times$ $\mathrm{R_{res}}$ = 4 $\times$ 1.3), RF TBP = 1.96, RF duration = 15 ms (same for 90°and 180°), TR/TE = 6300/65 ms, $\mathrm{R_{PSF}}$ = 32 (5 shots), TA = 31.5 s. In addition, the same VAT-PSF-EPI protocol was also acquired with three other different phase encoding directions: posterior-anterior, right-left, and left-right, to examine the robustness of distortion correction. For the distortion correction effectiveness examination, the VAT gradient amplitude was varied according to the optimal gradient amplitude with the following ratios: 0.78, 0.91, 0.95, 0.97, 1.0, and 1.18.

For the *in vivo* measurement, a healthy male subject was scanned with approval from the local institutional review board and informed consent. Fully PSF-sampled VAT-PSF-EPI was acquired to retrospectively examine the achievable maximum acceleration factor and compare it with PSF-EPI. The imaging parameters were set as follows: spatial resolution = 1.4 mm isotropic (160 shots, $\mathrm{R_{PSF}}$ = 1), readout receiver bandwidth = 1953 Hz/pixel, ETL = 40 (GRAPPA $\times$ $\mathrm{R_{res}}$ = 2 $\times$ 2), RF TBP = 2.62, RF duration = 20 ms (same for

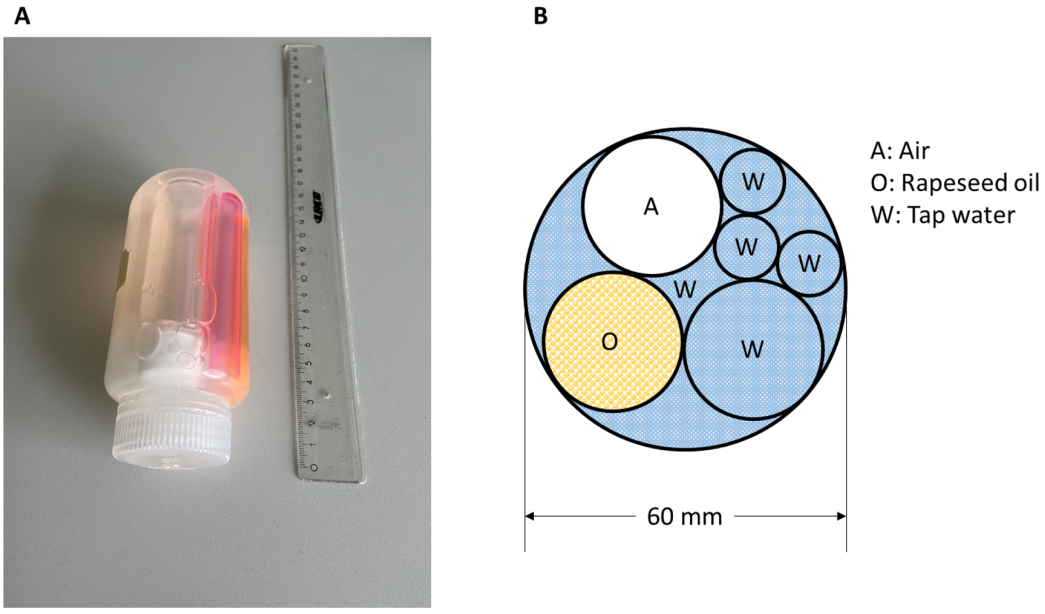

Figure 3.4: Oil-air-water phantom construction. A: The photo of the phantom includes a ruler as the distance metric. B: Illustration of the cross-section of the phantom. The phantom is to examine the water-oil chemical shift and water-air susceptibility-induced image distortion of the proposed VAT-PSF-EPI sequence.

90°and 180°), TR/TE = 2500/65 ms, TA = 6:40 min.

3.2.3 Simulation of the Eddy Current from Normal and High Diffusion b-values

The common assessments of eddy current distortion are limited to the normal b-value range ($\leq$ 1000 s/mm^2) [41, 91, 100]. It would be interesting to know how much its induced distortion increases to the high b-values ($\geq$ 3000 s/mm^2) before assessing the VAT-PSF-EPI. In the simulation, four different diffusion waveforms, including Stejskal-Tanner, TRSE, single bipolar, and dual bipolar, were simulated for diffusion efficiency and eddy current residual, as displayed in Figure 3.5. The dual bipolar gradients have an even symmetry, which means the order of gradient polarity for each bipolar gradient pair is the same. The simulated gradient system has a maximum gradient strength of 70 mT/m and a maximum slew rate of 200 T/m/s. Sequence timing was extracted from the vendor sequence simulation tool (IDEA). In the IDEA simulation, imaging parameters resolution was set to 1.4 mm isotropic with a FoV 224 mm^2. The EPI echo spacing was 0.75 ms, and all sequences were with GRAPPA 4. Two b-values with a commonly used b = 1000 s/mm^2 in brain imaging and a high b-value of b = 3000 s/mm^2 were simulated. The excitation RF pulse duration was 2.56 ms, and the refocusing RF pulse was 7.56 ms. There is an assumption that the gradient instantly switches in the eddy current simulation. At the same time, the switching duration is included in the diffusion duration for accurate

efficiency evaluation. In the simulation of diffusion weighting efficiency, the total diffusion duration is represented instead of TE. Because the total diffusion duration is the main contributor to TE in dMRI, the remaining durations of EPI readout and pre-phasing were set to the same for all waveforms (see Table 3.1).

Table 3.1: Total gradient duration of the simulated diffusion gradient waveforms in ms.

	Stejskal-Tanner	**TRSE**	**Single bipolar**	**Dual bipolar**
b = 1000 s/mm^2	36.83	59.94	43.48	68.04
b = 3000 s/mm^2	50.83	72.94	58.31	89.36

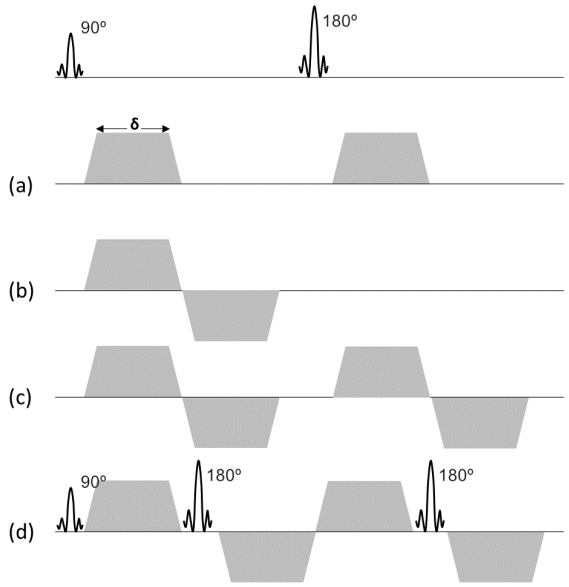

Figure 3.5: Simulated diffusion gradient waveforms. a: Stejskal-Tanner (monopolar); b: single bipolar; c: dual bipolar; d: twice-refocused spin echo (TRSE). Note that the gradient duration (δ) is not scaled to the actual timing.

3.2.4 Assessment of Susceptibility and Eddy Current Distortion Correction with Varying Diffusion b-Values

A structured phantom filled with silicone oil is used to examine the performance of VAT-PSF-EPI's eddy current distortion correction. Silicone oil has low ADC properties, making it suitable for examining the image fidelity of high b-value images without being affected by signal attenuation. The VAT-PSF-EPI was acquired with the Stejskal-Tanner diffusion gradient and compared to the Stejskal-Tanner and TRSE ss-EPI sequences for the imaging parameters. The diffusion gradient was sampled in a multi-shell scheme with b-values = 0, 500, 1000, 2000, 3000 s/mm^2. The acquired b-values and the corresponding diffusion gradient amplitudes are displayed in Figure 3.6. Except for b = 0 images acquired once,

each shell was sampled with the same 30 vendor-provided directions on the half q-space sphere (see Figure 3.6). The common imaging parameters were: spatial resolution = 1.4 mm isotropic, FoV = 224 mm^2, number of imaging slices = 25, readout receiver bandwidth = 1838 Hz/pixel, echo spacing = 0.75 ms, and TR = 6000 ms. The specific parameters for each sequence were: VAT-PSF-EPI: R_{PSF} = 32 (5 shots), ETL = 30 (GRAPPA $\times R_{res}$ = 4 × 1.33), no partial Fourier, RF TBP = 1.962, RF duration = 15.36 ms (same for 90° and 180°), TE = 77 ms, TA = 60:30 min. Stejskal-Tanner ss-EPI: GRAPPA = 3, partial Fourier = 5/8, TE = 67 ms, TA = 12:06 min. TRSE ss-EPI: GRAPPA = 4, partial Fourier = 5/8, TE = 84 ms, TA = 12:06 min. In addition, several b=0 images of VAT-PSF-EPI were acquired between measurements as the baseline for numerical comparison.

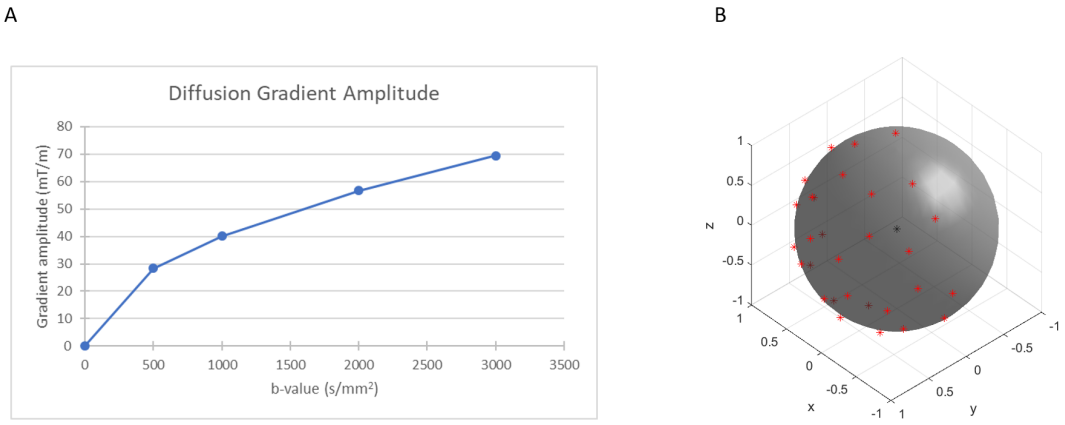

Figure 3.6: Diffusion b-values and b-vectors used in the experiment. A: b-values and the corresponding gradient amplitude. B: b-vectors represent the 3D (x, y, z) space. The vendor b-vectors are distributed in the half q-space.

For comparison, the post-processing correction of eddy current distortion was performed by FSL eddy current correction packages. In FSL, two correction packages are currently available: eddy_correct and eddy. Both packages are registration-based methods. The eddy_correct uses FSL FLIRT to register all DWI volumes to an undistorted b = 0 image, while eddy registers DWI volumes to an estimated undistorted image, similar to the FSL topup. The estimation of the eddy is based on the Gaussian processes, which assumes the diffusion gradient-induced distortion is axially symmetric and the averaging image of two opposite polarity images is undistorted (to the b = 0). The processing of FSL eddy_correct and eddy to Stejskal-Tanner ss-EPI were set mostly default, except the second level model was added in the eddy, and additional trilinear interpolation was tested in eddy_correct in addition to spline interpolation. The option of the second level model is used to remedy the non-optimal sampling for eddy, i.e., non-whole q sphere sampling and data without reversed phase encoding.

After the test with FSL, the best performance post-processing method was chosen and applied to all acquired sequences, including VAT-EPI extracted from the VAT-PSF-EPI

data. In the following, the same fuzzy thresholding method was used for masking. For the quantitative comparison, the performance of each sequence and the performed post-processing methods are compared with a numerical evaluation, coefficient of variation (CV):

$$C_v = \frac{\sigma}{\mu}, \tag{3.7}$$

where σ is the voxel-wise standard deviation across all acquired diffusion volumes, and μ is the mean signal. In addition, the image of VAT-EPI can be extracted from VAT-PSF-EPI, and its PSF displacement can be intrinsically measured in the phase encoding direction.

3.2.5 High Resolution *in vivo* dMRI

Two subjects were scanned with local institutional review board approval after informed consent. The first subject was scanned with 1.4 and 1.0 mm isotropic with the proposed VAT-PSF-EPI sequence and compared with other established methods. The compared established distortion reduction or correction methods include the readout-segmented EPI (rs-EPI) sequence, bipolar twice-refocused spin-echo (TRSE) diffusion gradient waveform, and the post-processing algorithms FSL topup and eddy as described previously. The second subject was scanned with a high isotropic resolution of 1.17 mm and a very high in-plane resolution of $0.7 \times 0.7 \times 2.8$ mm^3 of VAT-PSF-EPI DTI visualization.

The 1.4 mm isotropic experiment has FoV 224 mm^2, matrix size 160^2, one b = 0, and three orthogonal diffusion directions (x, y, z) in three shells (b = 1000, 2000, and 3000 s/mm^2) were designed. The VAT-PSF-EPI employed monopolar Stejskal-Tanner diffusion gradient waveform, whereas ss-EPI and rs-EPI applied TRSE waveform to minimize the eddy current residual. For the specific parameters, ss-EPI was acquired with minimum echo spacing 1.0 ms, GRAPPA 4, partial Fourier 5/8, TR/TE 3000/87 ms, three averages in both anteroposterior (A/P) and posteroanterior (P/A) phase encodings in order to apply the FSL topup. Therefore, the total scan time for ss-EPI was doubled by 1 min 50 s, thus 3 min 40 s. The rs-EPI used the minimum echo spacing 0.32 ms, GRAPPA 4, minimum shots number 7, TR/TE 3000/91 ms, and the total scan time was 3 min 42 s. VAT-PSF-EPI had the echo spacing of 0.8 ms, echo train length 30, 5 shots, thus the total acceleration factor 170 (GRAPPA $\times$ R_{res} $\times$ R_{PSF} = 4 $\times$ 1.33 $\times$ 32), and total scan time 2 min 30 s. In addition, the RF pulses used for VAT-PSF-EPI are Sinc pulses with a TBP factor of 1.962 and a duration of 15 ms for excitation and refocusing.

For the 1.0 mm isotropic experiment, FoV 224 mm^2, matrix size 224^2, the experiment of one b = 0 and six diffusion directions in single shells with b = 1000 s/mm^2 was designed. All sequences employed monopolar Stejskal-Tanner waveform, while the ss-EPI and rs-EPI applied FSL eddy for post-processing current distortion correction. The specific parameters for ss-EPI were minimum echo spacing 1.0 ms, GRAPPA 3, partial Fourier 6/8, TR/TE

3000/65 ms, and five averages in both A/P and P/A phase encodings to apply topup. The total scan time is 3 min 30 s. The rs-EPI had minimum echo spacing of 0.32 ms, GRAPPA 3, 11 shots, TR/TE 3000/57 ms, and the total scan time was 3 min 51 s. VAT-PSF-EPI had echo spacing of 1.0 ms, echo train length of 32, and 11 shots; therefore, the total acceleration factor 137 (GRAPPA $\times$ R_{res} $\times$ partial Fourier $\times$ R_{PSF} = 3 $\times$ 2 $\times$ 8/7 $\times$ 32), and a total scam time was 3 min 51 s. The imaging slices for all acquired sequences and both resolutions were 11 slices. Note that the imaging scan time does not account for the adjustment. The boundary F1 (BF) score was used for the numerical evaluation, where 1.0 is the perfect match.

For the high resolution 1.17 mm isotropic and 0.7 $\times$ 0.7 $\times$ 2.8 mm^3 DTI protocols, the scanning parameters are as follows: FoV $224^2/224^2$, 15/32 shots, ETL 32/54, TR 3000/3000 ms, TE 58/61 ms, total acceleration factor 78/60 (GRAPPA $\times$ R_{res} $\times$ R_{PSF} = 3/3 $\times$ 2/2 $\times$ 32/54), and the total scan time 9 min 45 s/20 min 48 s. One b = 0 and twelve diffusion-weighted volumes with b = 1000 s/mm^2 were collected.

All data were processed in a PC (Intel Core i5-6600K 3.50 GHz Processor, 32.0 GB RAM, Intel 600 P SSD). The data of VAT-PSF-EPI are reconstructed using Matlab 2015b (MathWorks, Natick, MA, USA). The post-processing distortion correction packages of FSL topup and eddy were used.

3.2.6 Limitation 1 - SNR Reduction in VAT-PSF-EPI

The current implementation of PSF is only on one axis of the image encoding directions. Thus, each imaging slice has 3D (x, y, y_1) data. In Section 3.1, the signal modulation function was measured by the signal change alone in each distorted image or each EPI phase encoding data (y). For the PSF-EPI as a multi-shot imaging method, the final undistorted image (x, y_1) can be performed either the complex summation or magnitude summation along EPI phase encoding (y).

The complex summation of data is a Fourier transform. After taking the absolute value, it becomes the image from the central EPI phase encoding data. This can be explained by the signal modulation function in Figure 3.7, which was adapted from Figure 3.10. It can be seen that the signal central phase encoding data of VAT-EPI in VAT-PSF-EPI and EPI in PSF-EPI are similarly high.

On the other hand, the magnitude summation can be understood by the Plancherel theorem (or Rayleigh's energy theorem), in which the energy is conserved in the image and *k*-space domains.

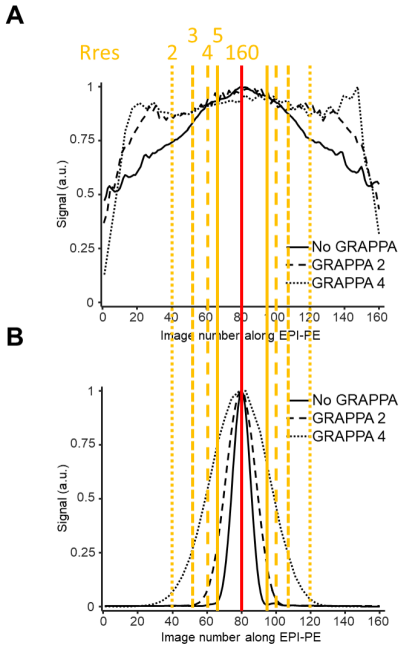

Figure 3.7: SNR reduction and improvement in VAT-PSF-EPI. SNR reduction in VAT-PSF-EPI is due to the VAT gradient leading to higher signal decay than T_2* decay at boundaries, which is decreased using GRAPPA. The proof of concept SNR's further improvement is discarding the low signal images at boundaries, equivalent to reducing the EPI resolution. Nevertheless, the final resolution of VAT-PSF-EPI will not be changed. R_{res} is the resolution reduction factor. Image adapted from Figure 3.10.

$$
\begin{aligned}
\int_y |\hat{\rho}(x,y,y_1)|^2 dy &= \int_y \hat{\rho}(x,y,y_1)\cdot\overline{\hat{\rho}(x,y,y_1)}dy \\
&= \int_{k_y}\{\int_y \hat{\rho}(x,y,y_1)e^{-2\pi i(k_y\cdot y)}dy\cdot\overline{\{\int_{y'}\hat{\rho}(x,y',y_1)e^{-2\pi i(k_y\cdot y')}dy'\}}dk_y \\
&= \int_{k_y}\int_y \rho(x,y_1)\frac{\overline{G_y}}{G_{VAT}}RECT(\frac{y'-y_1}{\frac{G_{VAT}}{\overline{G_y}}\frac{L}{2}})e^{-2\pi i(k_y\cdot y)}dy \\
&\quad \overline{\cdot\int_{y'}\rho(x,y_1)\frac{\overline{G_y}}{G_{VAT}}RECT(\frac{y'-y_1}{\frac{G_{VAT}}{\overline{G_y}}\frac{L}{2}})e^{-2\pi i(k_y\cdot y')}dy'dk_y} \qquad (3.8)\\
&= \int_{k_y}\rho(x,k_y,y_1)\cdot L\cdot SINC(2\pi k_y\frac{G_{VAT}}{\overline{G_y}}\frac{L}{2})e^{-2\pi i(k_y\cdot y_1)}\cdot\overline{\rho(x,k_y,y_1)} \\
&\quad L\cdot SINC(2\pi k_y\frac{G_{VAT}}{\overline{G_y}}\frac{L}{2})e^{2\pi i(k_y\cdot y_1)}\,dk_y \\
&\int_{k_y}|\rho(x,k_y,y_1)\cdot L\cdot SINC(2\pi k_y\frac{G_{VAT}}{\overline{G_y}}\frac{L}{2})|^2 dk_y.
\end{aligned}
$$

Therefore, the final magnitude summation undistorted image is modulated with a Sinc function, decreasing the SNR.

A straightforward method to compare with such SNR reduction is discarding the low signal data. For simplicity, the discarding factor is set to the R_{res} factor, and its reciprocal is the discarding ratio of total data. Thus, half of the R_{res} data are discarded from the boundaries of EPI phase encoding. In other words, the EPI resolution is reduced by a factor of R_{res} (Figure 3.7).

The full-sampled PSF 1.4 mm^3 structural phantom data in Section 3.2.1 with different GRAPPA factors 1, 2, and 4 were reused to evaluate the SNR of PSF-EPI and VAT-PSF-EPI. Two SNR evaluations were performed by retrospective simulation with R_{res} and R_{PSF} varying.

In the first simulation, the R_{res} under-sampling was done from 1 to 10 and filled with zero in the EPI phase encoding (see Figure 3.7), and the R_{PSF} was kept to 1. The SNR of the magnitude summed image was measured with the signal from the homogenous region of the phantom and the noise from the clear background.

In the second simulation, the highest possible R_{PSF} was firstly determined from the full-PSF sampled data under the criterion of the aliasing artifact from PSF acceleration less than 10 % of signal than the central image. After that, the highest possible R_{res} was determined by keeping the same criterion, and the SNR was measured as in the first simulation.

3.2.7 Limitation 2 - Artifacts in VAT-PSF-EPI

The analysis in the current section takes two steps to determine the source of the ghosting artifact of the fat content. The first step is to reuse the *in vivo* data from the previous section, and the second is to acquire new phantom data. An additional phantom experiment was performed to avoid confusion about ghosting with motion artifacts.

Both *in vivo* and phantom data were 1.4 mm^3 with R_{PSF} 32 and a b-value of 1000 s/mm^2. In the *in vivo* data, 1D Nyquist ghost correction was skipped in the reconstruction processing to emphasize the ghosting positions. In order to exclude the PSF over-accelerating artifact, the images of VAT-EPI were also reconstructed. The phantom experiment was acquired with the same oil-air-water phantom and MR parameters as in Section 3.2.2. The only change is that the DWI was acquired in addition to the T_2W image.

3.2.8 Improved High Resolution *in vivo* dMRI

The phantom and *in vivo* human experiments were scanned to demonstrate the fat/oil Nyquist ghosting and through-plane artifact and their suppression. Two subjects were scanned with the local approval from the ethics committee.

The structural silicone phantom was scanned with five shots VAT-PSF-EPI with b = 0 image and a b = 1000 s/mm^2 (1, 0, 1) DW image in 31 continuous imaging slices. The relevant parameters are as follows: FoV 224 mm^2, matrix size 160^2, RF bandwidth 130

Hz, TR/TE 6300/60 ms, GRAPPA 4, R_{res} 1.33, R_{PSF} 32 (total acceleration factor 170), and the total scan time for each DWI was 31.5 s. The parameters for the first *in vivo* subject were the same as in the phantom measurement, except 23 slices instead of 31 were measured. To demonstrate the through-plane artifact suppression, the 90-180 RF durations were first used, the same as 15 ms, to highlight the through-plane artifact. Next, the differencing RF method was implemented in diffusion imaging with an RF duration reduction in excitation rather than refocusing to make the overall SAR low. As a result, the excitation duration was halved to the refocusing 7.5 for the fat artifact suppression.

The second subject was scanned with two resolution protocols, 1.17 mm^3 and 0.7 × 0.7 × 2.8 mm^3. The former high isotropic resolution protocol includes R_{PSF} 16, GRAPPA 3, R_{res} 2 (total acceleration factor 96), TR/TE 3000/64 ms, one b = 0 and 12 b = 1000 s/mm^2 DWIs. The total scan time was 7.2 minutes. The later very high in-plane resolution protocol was with R_{PSF} 16, GRAPPA 4, R_{res} 2.5 (total acceleration factor 160), TR/TE 3000/67 ms, one b = 0 and 20 b = 1000 s/mm^2 DWIs. The total scan time was 20 minutes.

3.3 Results

The distortion uncorrected and corrected EPI images in a selected imaging slice are presented (Figure 3.8), together with the 1D PSF profiles measured from a specific voxel within that slice. PSF-EPI and VAT-PSF-EPI sequences are full-sampled (no acceleration) in the PSF phase encoding and EPI phase encoding, i.e., R_{PSF} 1 and no GRAPPA. The uncorrected image, PSF-corrected image, and PSF (i.e., images and profile from the same raw) are calculated from the same full PSF-sampled raw data. In EPI, an uncorrected image has gigantic susceptibility-induced image distortion at the structure boundaries along the EPI phase encoding direction (y). Meanwhile, in the PSF-corrected images, the gigantic geometric distortion is corrected. A few signal dropouts correspond to the highest distortion areas. In the uncorrected VAT-EPI, the geometric distortion is suppressed effectively by VAT. However, a huge image blurring accompanies the EPI phase encoding direction (y). In the PSF-corrected VAT-EPI, both geometric distortion and blurring are corrected well. The signal dropout is smaller than in the PSF-corrected EPI at the four corners of the image but has neglectable signal pile-up spots at the corners of the inner structure. The 1D PSF profile was selected from a gigantic distortion region (x = 57, y_1 = 129) (red voxel) in EPI to demonstrate excellent distortion suppression in VAT-EPI. The PSF measurement calculates the relative PSF peak displacement (distortion) and extension (blurring) between the distorted image (x, y) and the reference undistorted image (x, y_1). In EPI, the PSF is measured as 31 pixels (4.3 cm) displacement and 2 pixels (0.3 cm) width. In contrast, in VAT-EPI, the PSF displacement is 0.46 pixels (0.06 cm), and the width is 6.5 pixels (0.9 cm). The result demonstrates effective distortion suppression of VAT-EPI and a smaller PSF range than in EPI (i.e., green lines and yellow lines). Also, full

PSF-sampled PSF-EPI and VAT-PSF-EPI can correct the image distortion and blurring well.

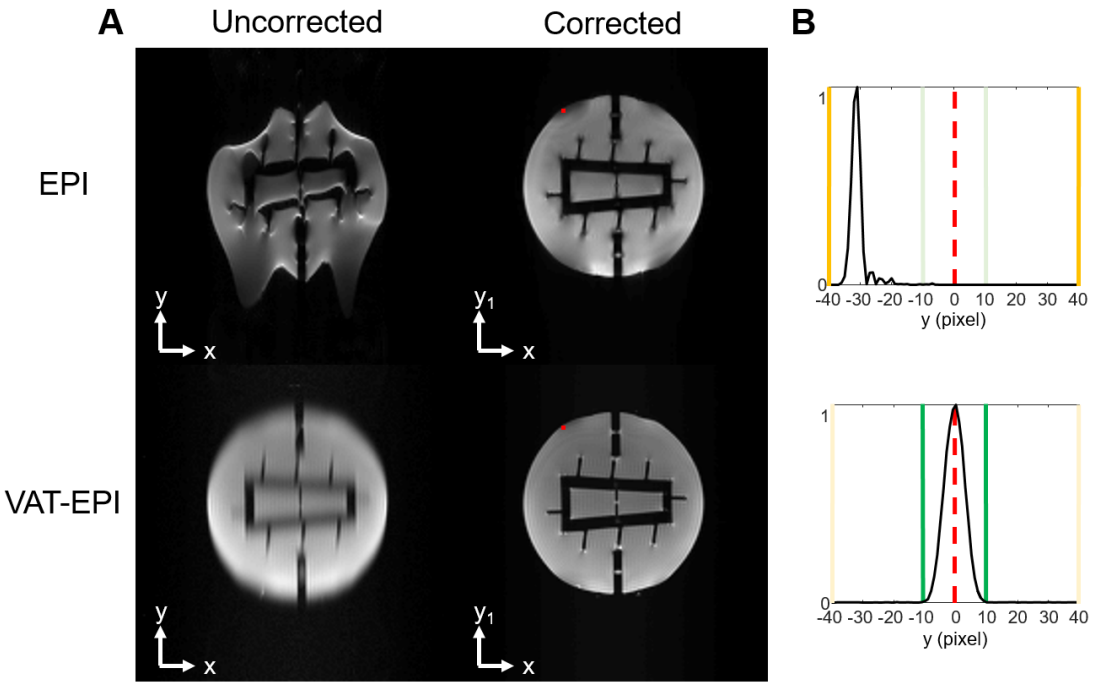

Figure 3.8: Full-PSF sampled VAT-PSF-EPI and PSF-EPI data. A: distortion uncorrected and corrected images, B: PSF plotted from the air-phantom interfaces of corrected images (red dot). The distortion uncorrected images are either EPI generated from PSF-EPI data or VAT-EPI generated from VAT-PSF-EPI data. Both distortion-corrected images showed good correction results from in-plane distortion. An example of the PSF range is plotted in B. The PSF range in VAT-EPI is much smaller than in EPI, demonstrating the potential acceleration capability in VAT-PSF-EPI.

Voxel-wise PSF maps of VAT-EPI and the corresponding distortion-corrected VAT-PSF-EPI images are displayed in Figure 3.9 and compared with those in EPI. PSF-EPI and VAT-PSF-EPI were acquired without GRAPPA (ETL = 160). The PSF range of EPI is composed of huge displacement values in both polarities and small width values with small variations at boundaries. The highest value in the PSF range was 36.1 pixels, with 33.5 pixels of displacement and 2.6 pixels of width. According to equation 2.43, the maximum rFoV factor to unfold the PSF-EPI image without aliasing artifact is 2 (80 shots). In contrast, VAT-EPI had homogeneous PSF range values composed of small displacement and large width values. The highest PSF range was 9.61 pixels with -1.37 pixels displacement and 8.24 pixels width. Therefore, the applicable maximum rFoV factor to unfold VAT-PSF-EPI image increased to 8 (20 shots) compared to PSF-EPI, which is four times faster. In addition, in the PSF-corrected images, the corresponding maximum rFoV accelerated images showed no image fidelity (distortion, blurring or artifacts; i.e., Figure 2.7) degradation compared to the full PSF-sampled images in both PSF-EPI and

VAT-PSF-EPI. Moreover, the images with doubled maximum applicable rFoV factor demonstrate the aliasing artifact in different forms, i.e., strong signal displacement in PSF-EPI and ghosting in VAT-PSF-EPI. Detailed PSF measurements are shown in Table 3.2.

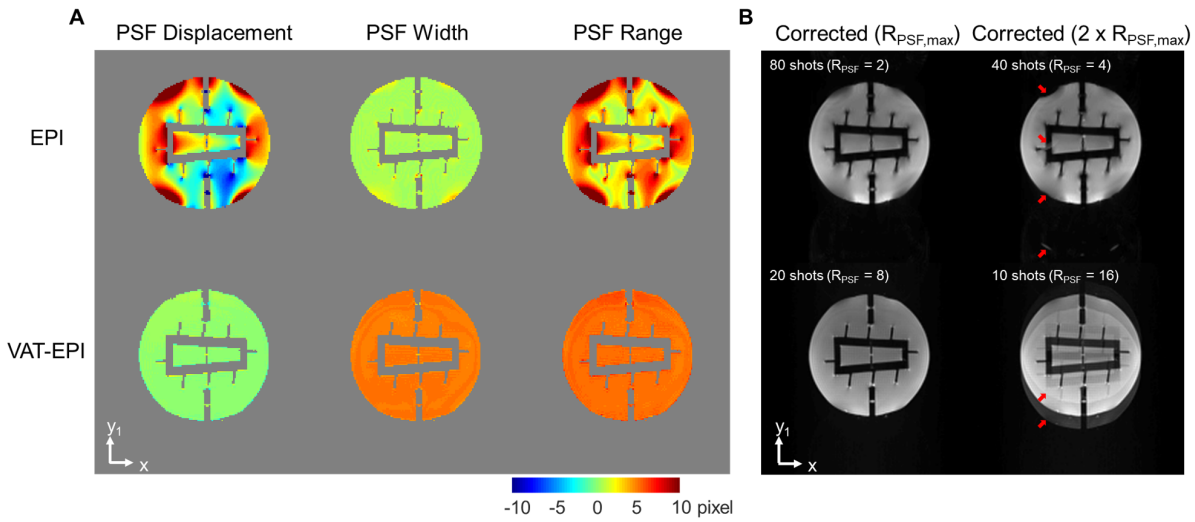

Figure 3.9: PSF maps and the sequence acceleration. A: PSF maps in separating the contribution of PSF displacement and PSF width. B: Image acceleration examination. The upper row shows the image distortion and blurring in EPI, and the lower row is VAT-EPI. The available acceleration in VAT-PSF-EPI is fourfold that of the PSF-EPI.

Signal modulation functions and the distortion-corrected images retrospectively reconstructed from VAT-PSF-EPI with different GRAPPA factors (1 [ETL = 160], 2 [ETL = 80], and 4 [ETL = 40]) are displayed in Figure 3.10 and compared to PSF-EPI. GRAPPA factor 1 means no GRAPPA acceleration was applied during MR scanning. The applied VAT ratios (view-tilting angles) of VAT-PSF-EPI were 16.35 (86.5°) for GRAPPA 1, 8.17 (83.0°) for GRAPPA 2, and 4.08 (76.2°) for GRAPPA 4. The modulation function plots the signal profile along (x, y, k_y), and thus, the signal changes along the EPI (or VAT-EPI) phase encoding direction in the *k*-space. The central image number in this plot means the *k*-space center, while the peripheral image numbers contain high spatial frequency information. GRAPPA reduces the signal decrease in the periphery of the signal profile and results in image blurring reduction in both EPI and VAT-EPI. In the measured signal profiles of PSF-EPI, GRAPPA 1 had the highest signal reduction in the periphery and was mitigated progressively with GRAPPA 2 and 4. In VAT-PSF-EPI, the signal profile was much narrower with GRAPPA 1 compared to PSF-EPI and became wider for higher GRAPPA factors. In addition, image distortion also decreased with higher GRAPPA factors in both EPI and VAT-EPI (see Table 3.2). As a result, the applicable maximum

Table 3.2: PSF quantification and maximum acceleration of PSF-EPI and VAT-PSF-EPI sequences. In each PSF map, 0.5 % of the total phantom area (28 pixels) was selected to measure the highest PSF amounts and represented in the median (interquartile range).

	PSF Displacement	**PSF Width**	**PSF Range**	$\mathbf{R_{PSF,max}}$
VAT-PSF-EPI, 1.4 mm, TBP 2.616 (pixel)				
GRAPPA 1	1.52 (1.38-2.06)	6.89 (6.51-7.26)	8.47 (8.37-8.70)	9.45 (9.19-9.56)
GRAPPA 2	0.800 (0.710-1.26)	3.53 (3.00-3.74)	4.30 (4.25-4.47)	18.6 (17.9-18.8)
GRAPPA 4	0.370 (0.271-0.432)	1.96 (1.89-1.99)	2.28 (2.23-2.36)	35.1 (33.9-35.9)
PSF-EPI, 1.4 mm, TBP 2.616 (pixel)				
GRAPPA 1	27.4 (25.9-30.6)	2.62 (2.45-2.92)	30.2 (28.3-33.4)	2.65 (2.39-2.83)
GRAPPA 2	13.7 (13.3-15.3)	1.13 (0.926-1.29)	14.9 (14.3-16.5)	5.36 (4.85-5.58)
GRAPPA 4	7.26 (6.82-7.96)	0.832 (0.748-0.975)	8.12 (7.70-8.71)	9.86 (9.18-10.4)
VAT-PSF-EPI, GRAPPA 2, TBP 2.616 (pixel)				
2.8 mm	0.776 (0.570-1.26)	3.81 (3.54-3.97)	4.52 (4.34-4.71)	17.7 (17.0-18.4)
1.4 mm	0.800 (0.728-1.26)	3.50 (3.00-3.70)	4.30 (4.25-4.47)	18.6 (17.9-18.8)
0.7 mm	0.966 (0.916-1.13)	3.37 (3.26-3.45)	4.35 (4.29-4.45)	18.4 (18.0-18.7)
VAT-PSF-EPI, GRAPPA 2, 1.4 mm (pixel)				
TBP 1.308	0.975 (0.667-1.29)	6.05 (5.64-6.38)	6.85 (6.75-7.09)	11.7 (11.3-11.8)
TBP 1.962	0.946 (0.676-1.27)	4.29 (4.04-4.71)	5.27 (5.18-5.52)	15.2 (14.5-15.4)
TBP 2.616	0.793 (0.536-0.885)	3.98 (3.80-4.08)	4.69 (4.63-4.80)	17.0 (16.7-17.3)

rFoV factor of PSF-EPI and VAT-PSF-EPI increased linearly with the GRAPPA factors. In the detailed PSF analysis, VAT-EPI suppresses 94.5 ± 0.3 % distortion compared to EPI regardless of GRAPPA. The total PSF range in the VAT-EPI is compositing of 20.3 ± 2.9% PSF displacement, and PSF width is the rest. The VAT blurring contributes to the majority of 62.7 ±4.5 % of PSF width, derived from the subtraction of PSF width from EPI, considered as T_2* blurring. A small difference of 2.72 ± 1.33 % was obtained by comparing the measured VAT blurring to the analytical expression. In contrast, PSF width has a small amount of 10.2 ± 1.2% within the PSF range, which is usually ignored in EPI. In PSF-EPI, the applicable maximum rFoV factor was 2 (80 shots) for GRAPPA 1, 4 (40 shots) for GRAPPA 2, and 8 (20 shots) for GRAPPA 4. While in VAT-PSF-EPI, the applicable maximum rFoV factor was 8 (20 shots) for GRAPPA 1, 16 (10 shots) for GRAPPA 2, and 32 (5 shots) for GRAPPA 4. Thus, regardless of the GRAPPA factor, VAT-PSF-EPI can be acquired four times faster than PSF-EPI. Note that with the GRAPPA 4, the image distortion of VAT-EPI (the uncorrected image) was suppressed via VAT compared with EPI, and the image blurring was barely noticeable.

As shown above, the change in the PSF range leads to the difference in the applicable maximum rFoV factor. Further examination of the VAT-PSF-EPI signal modulation function and the acceleration factors by changing the slice thickness or RF combinations are shown in Figure 3.11. The rest of the parameters were kept the same, including the GRAPPA, which was fixed to two (ETL = 80). For the slice thickness experiment, the VAT gradient amplitude ratio (view-tilting angles) was 16.35 (86.5°) for 0.7 mm, 8.17

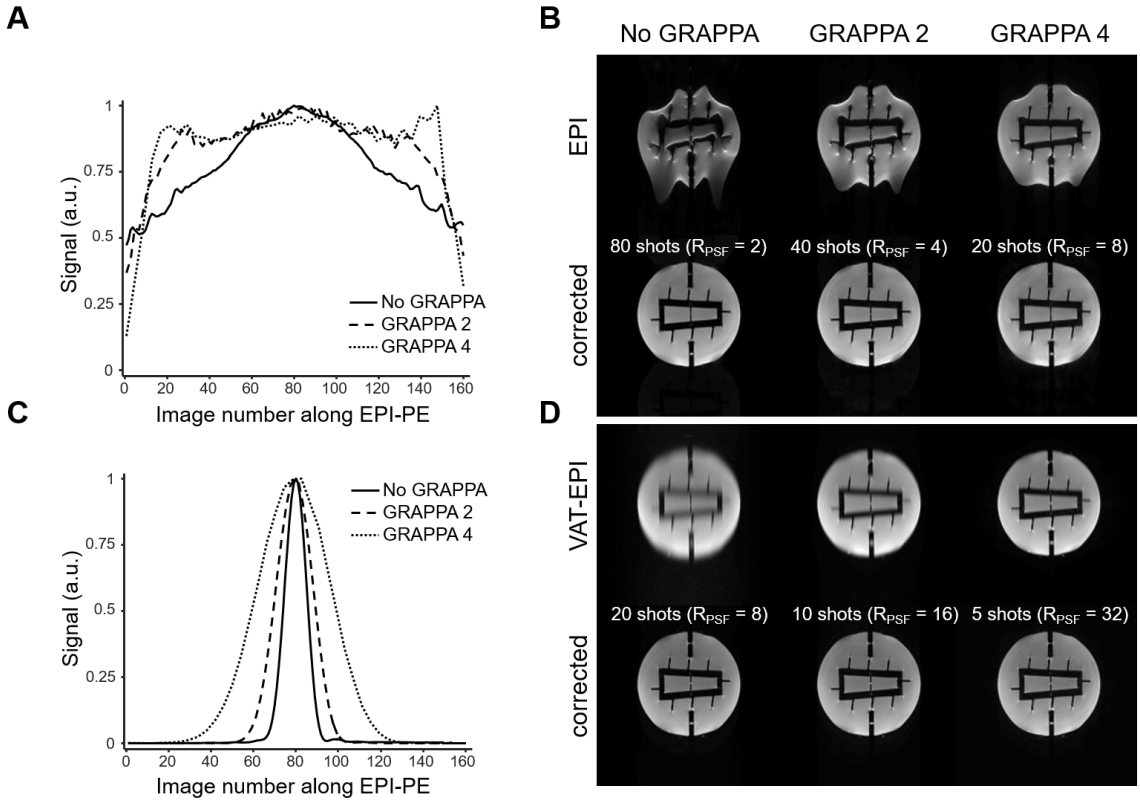

Figure 3.10: Signal modulation profile and the uncorrected and corrected images in various in-plane GRAPPA factors (1, 2, and 4). A, C: Signal modulation profile. B, D: distortion uncorrected and corrected images. The upper row contains images reconstructed from PSF-EPI, and the lower row contains VAT-PSF-EPI. The VAT-EPI corrects the geometric distortion well in all GRAPPA factors, and the image blurring decreases with higher GRAPPA factors. Notably, because the acceleration of the PSF sequences is inversely proportional to the PSF range, VAT-PSF-EPI shows a fourfold imaging speed compared with PSF-EPI without sacrificing image fidelity.

(83.0°) for 1.4 mm, and 4.08 (76.2°) for 2.8 mm. The signal profiles were a similar width but had an amplitude scaling. The amplitude ratio for 0.7 mm, 1.4 mm, and 2.8 mm was 0.24:0.48:1.0. The applicable maximum rFoV factor was 16 (10 shots) for all three slice thicknesses. Local signal variation at inner boundaries became evident when the slice thickness increased. For the experiment with changing RF, the applied VAT gradient ratio and the view-tilting angle were kept the same at 8.17 (83.0°) for three different combinations of RF. The TBP and RF duration were 2.616/20 ms, 1.962/15 ms, and 1.308/10 ms, but the RF excitation bandwidth remained the same. When RF duration decreases, the width of the signal profile decreases slightly while the signal amplitude increases in the ratio of 0.40:0.55:1.0 for 20 ms, 15 ms, and 10 mm. The applicable maximum rFoV factor was 16 (10 shots) for 20 ms, 13 (12 shots) for 15 ms, and 11 (14 shots) for 10 ms. The detailed PSF measurement of these two experiments is included in

Table 3.2.

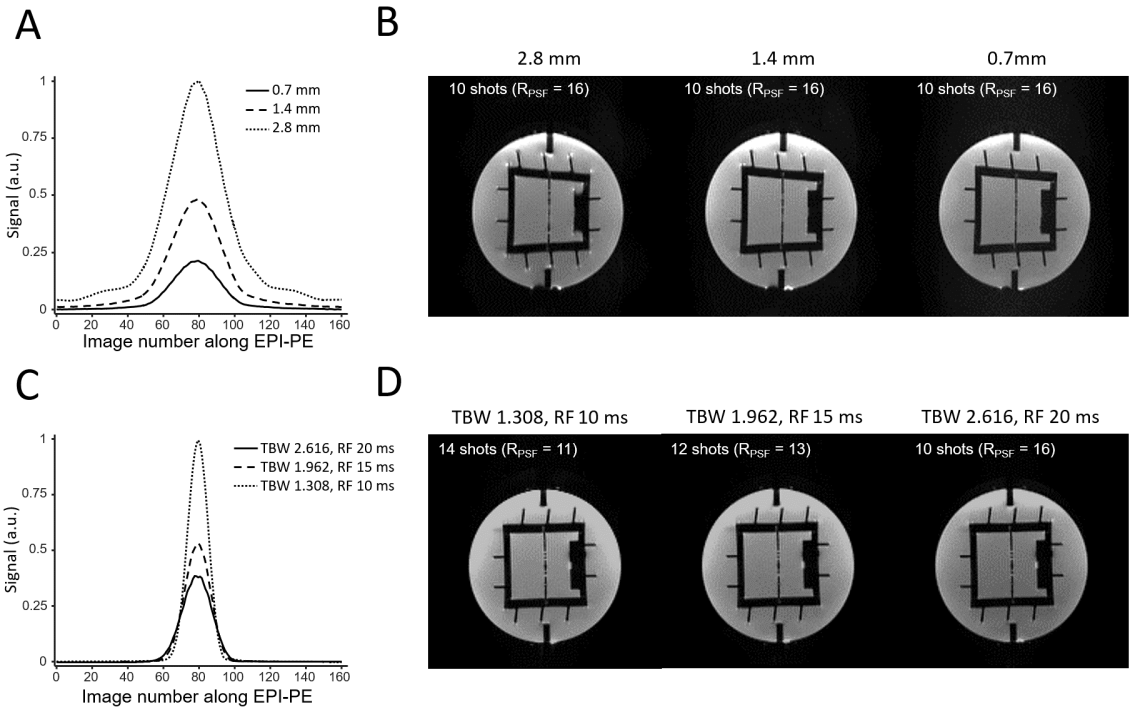

Figure 3.11: Signal modulation profile and corrected images with varying slice thicknesses and RF parameters. A, C: Signal modulation profile B, D: accelerated distortion corrected images. The upper row shows the slice thickness change, and the lower row shows the RF pulse change. Both unchanged image acceleration factors in changing with slice thickness and changed image acceleration factors verified the updated VAT theory from the current thesis.

Figure 3.12 demonstrates an air-oil-water phantom's fat-water chemical shift-induced distortion on top of air-water susceptibility-induced distortion. Despite a high GRAPPA factor of four, susceptibility-induced distortion and T_2* blurring is noticeable in ss-EPI with a fat-suppression RF pulse. When the fat suppression was switched off, the oil signal became visible, with a large displacement of -30.5 pixels (4.3 cm) toward the opposite phase encoding direction. While the TSE with strong fat suppression RF is the non-distortion reference image, the oil signal appeared and had a small displacement of around 1.0 pixels (0.1 cm) toward the opposite frequency encoding direction when fat suppression was switched off. The proposed VAT-PSF-EPI corrected the image distortions and the blurs caused by the T_2* signal decay and VAT signal modulation function.

Validation of the distortion correction robustness with four different phase encoding directions of VAT-PSF-EPI is displayed in Figure 3.13. The edge detected by the Sobel filter from the fat-suppressed TSE is superimposed on the ss-EPI and the VAT-PSF-EPI. The BF score was 0.91 for ss-EPI and an average of 0.99 for VAT-PSF-EPI with four different directions, where 1.0 is the perfect match. No additional correction processing

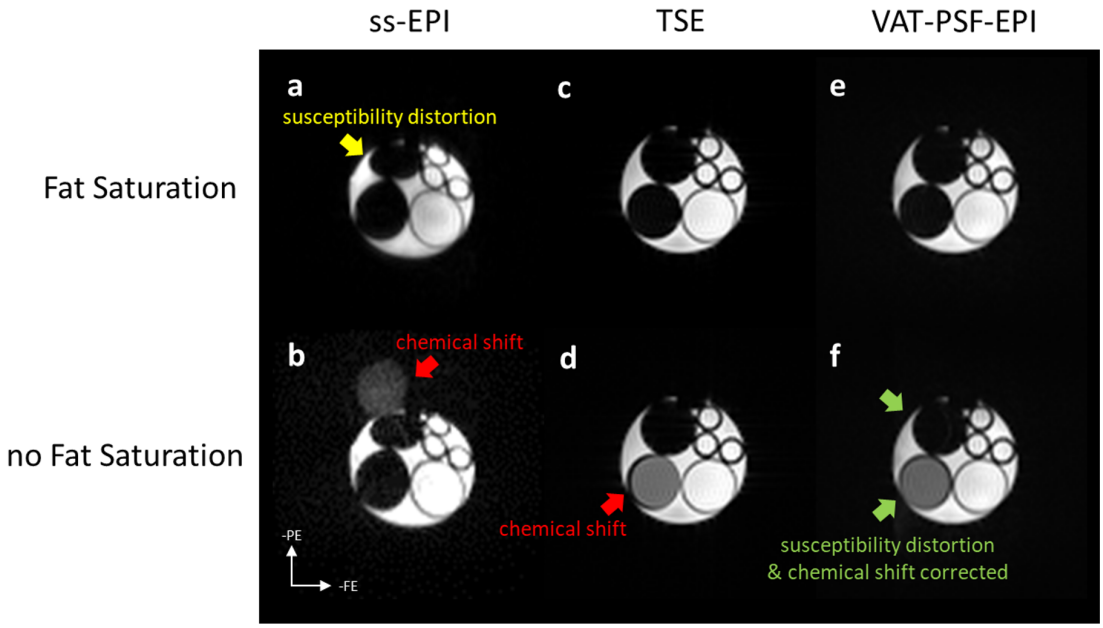

Figure 3.12: Images with and without fat suppression. a, b: EPI; c, d: TSE; e, f: VAT-PSF-EPI. The left column has fat suppression, and the right does not. The air-water susceptibility-induced geometric distortion is significant in EPI, even with GRAPPA 4. Fat signal shifting is observed without fat suppression and is more significant than susceptibility distortion. The reduced oil signal in EPI is due to the unmatched RF bandwidth between 90°and 180°pulses in the vendor EPI as another fat suppression method. The TSE with maximized bandwidth shows a slight chemical shift, while the susceptibility artifact is not observable. In the VAT-PSF-EPI, neither artifact is observed.

was made in VAT-PSF-EPI.

Further examination of the effectiveness of VAT-EPI and VAT-PSF-EPI in correcting the susceptibility and chemical-induced distortions is shown in Figure 3.14. In the range of 0.78 to 1.18 times the optimal VAT gradient amplitude, the susceptibility-induced distortion was corrected in VAT-EPI, and small displacements of water signal were at the upper part of the phantom with -1.0 pixel (0.1 cm) in the ratio of 0.78 and 1.0 pixel (0.1 cm) in the ratio of 1.18. Meanwhile, the oil signal displacements are pronounced and changed gradually in the gradient, varying from -5.0 pixels (0.7 cm) to 7.0 pixels (1.0 cm). No aliasing artifact from the susceptibility-induced distortion and VAT gradient-induced blurring can be observed in VAT-PSF-EPI. However, oil signal displacements in the VAT gradient ratio of 0.78 and 1.18 were the same as in VAT-EPI. In the ratio of 0.91, a transition of oil signal displacement from the 0 pixels to the -5 pixels was observed. For the ratios of 0.95 and 0.97, the images had no difference from the image of optimal ratio.

The *in vivo* human brain PSF maps and the T_2-weighted images are presented in Figure 3.15. In EPI, the PSF measurement shows a large displacement of 24 pixels (3.4 cm or 375 Hz) in the frontal region and a huge displacement of -60 pixels (8.4 cm or

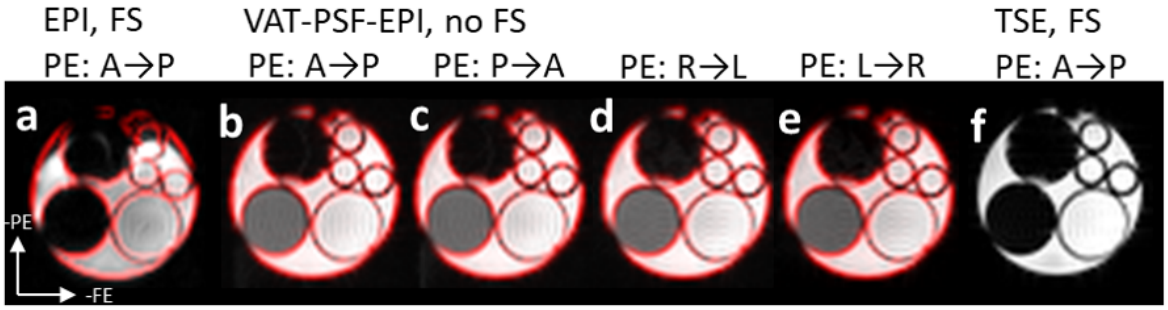

Figure 3.13: Numerical evaluation of distortion correction. a: EPI with fat suppression; b, c, d, e: VAT-PSF-EPI without fat suppression in different phase-encoding directions; f: TSE with fat suppression. The red contour was detected by TSE and superimposed on the EPI and VAT-PSF-EPI. The BF score is 0.91 for EPI and an average of 0.99 for VAT-PSF-EPI, where 1.0 is the perfect match.

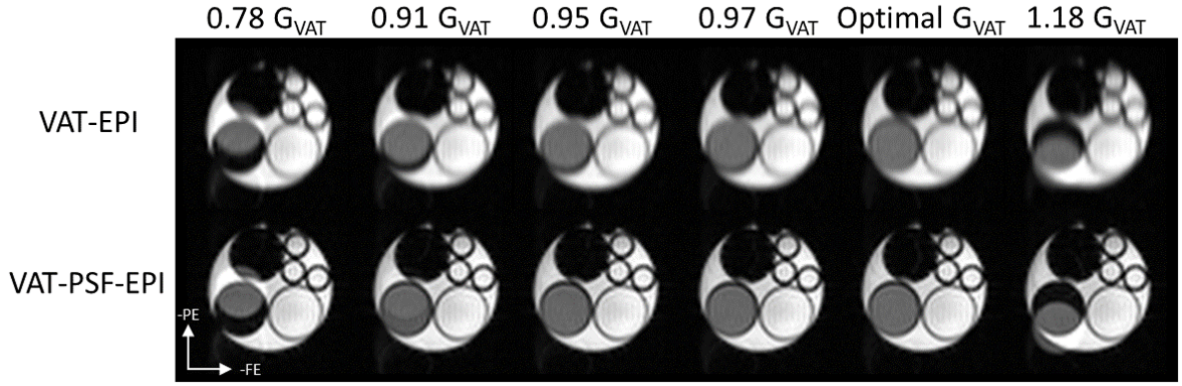

Figure 3.14: Images deviating from the optimal VAT gradient. The upper row is the PSF uncorrected images (VAT-EPI) with varying VAT gradients during acquisition, and the lower row is the PSF corrected images. In the uncorrected images, the amount of oil signal shift changes according to the VAT gradient variation, while susceptibility distortion does not change within ± 20 % VAT gradient. In the corrected images, oil signal variation is observed with more than 5 % VAT gradient change, while no susceptibility distortion is observed within ± 20 % VAT gradient.

937 Hz) for occipital subcutaneous fat tissue. The width was small, with a mean of 1.4 pixels (0.2 cm). The applicable R_{PSF} was 3 (54 shots) to resolve the susceptibility-induced distortion and 1 (160 shots) to resolve the water-fat chemical shift-induced distortion in PSF-EPI. In VAT-EPI, the displacement was negligible over the entire head region with a mean of 0.15 pixels (0.02 cm or 2 Hz), while the mean width was 2.5 pixels (0.4 cm) and larger than in EPI. As a result, VAT-PSF-EPI had a high R_{PSF} of 14 (11 shots) to resolve these effects. Thus, a 4.7-fold faster acquisition than the traditional PSF-EPI is possible for the susceptibility-induced distortion correction or 14-fold for the water-fat chemical shift-induced distortion correction.

In the reconstructed T_2-weighted images, the distortion from water–fat chemical shift (yellow arrow) is visible in EPI and was much larger than the susceptibility-induced distortions (red arrow). PSF-EPI corrected the susceptibility artifact with 54 PSF-encoding steps ($R_{PSF} = 3$), but the shifted fat artifact remained. In contrast, VAT-EPI suppressed both effects, albeit with increased blurring. The proposed VAT-PSF-EPI corrected the abovementioned off-resonance effects with 11 PSF encoding steps ($R_{PSF} = 14$) without aliasing artifacts.

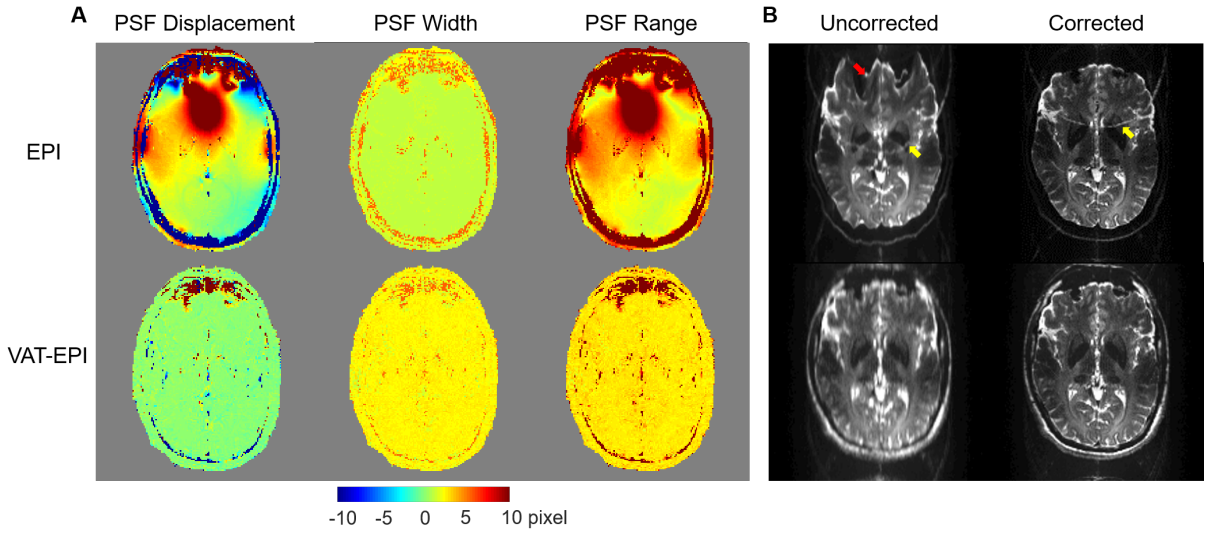

Figure 3.15: PSF maps and images of *in vivo* human head without applying fat suppression. A: PSF maps separating PSF displacement and width; B: PSF uncorrected and corrected EPI images. The upper row is data from PSF-EPI, and the lower is VAT-PSF-EPI. The red and yellow arrows indicate susceptibility distortion and chemical shift, corresponding to the PSF map's high positive and negative displacements in EPI. The high air-tissue susceptibility is typically close to the human head's frontal sinus and middle ear cavity.

In the simulation of diffusion efficiency, the minimum total durations for each gradient waveform are listed in Table 3.1 (Section 3.2.3). The Stejskal-Tanner has the shortest duration to produce the required diffusion weighting and has the highest efficiency for both b-values. The efficiency ranges from high to low, and it is Stejskal-Tanner, single

bipolar, TRSE, and dual bipolar. The ratio of average total duration is 1:1.53:1.16:1.80. In addition, the extended diffusion duration from b = 1000 s/mm^2 to b = 3000 s/mm^2 is 138 % for Stejskal-Tanner, 1.22 for TRSE, and 1.34 for single bi-polar and dual bipolar waveforms.

The simulation of the eddy current residual right after the diffusion module is displayed in Figure 3.16. At first glance, eddy current residuals sharply increase when the time constant is less than 10 ms for all waveforms, with different levels of decay followed by that. In a closed look, Stejskal-Tanner has the highest eddy current residual compared with the other three waveforms, except single bipolar has a higher residual for the time constant less than 10 ms. Although single bipolar has a higher residual in the short time constant period, it decreases drastically and overlaps with dual bipolar at 50 ms for b = 1000 s/mm^2 and 60 ms for b = 3000 s/mm^2. TRSE has the lowest amplitude on short-time constants and the highest decay rate on the intimidate time constants, where the residual crosses zero (null point) at 23 ms for b=1000 s/mm^2 and 28 ms for b = 3000 s/mm^2.

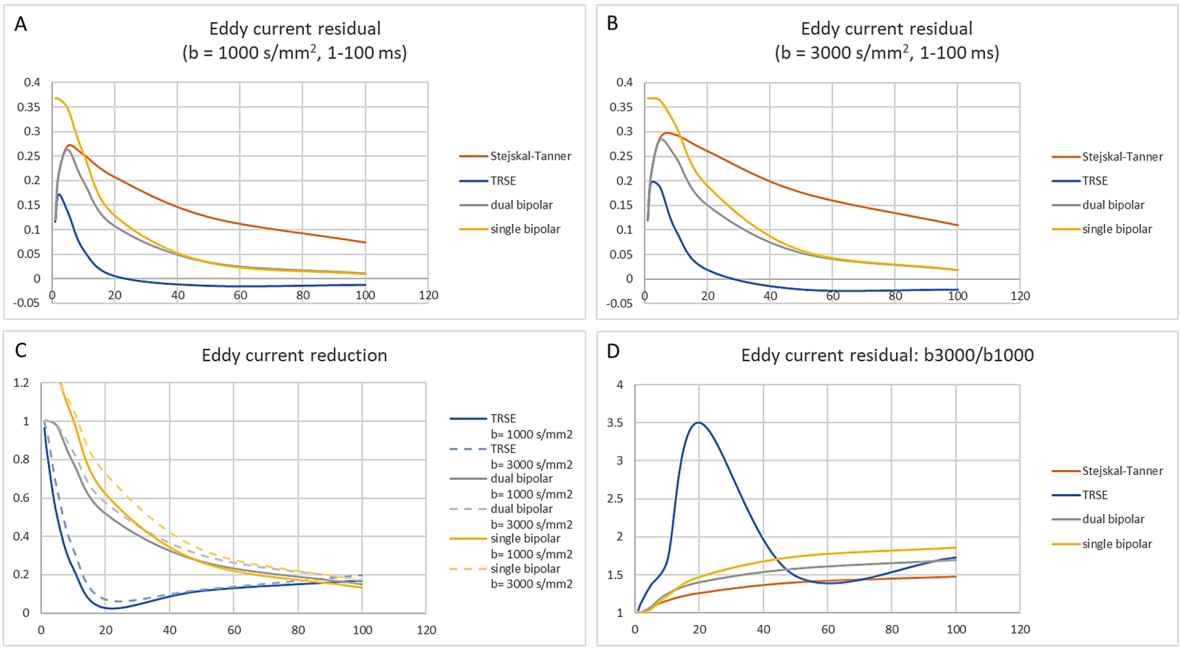

Figure 3.16: Numerical simulation of eddy current residual with different diffusion gradient waveforms in the SC72 whole-body gradient system with maximum amplitude 70 mT/m and slew rate 200 T/m/s. A: eddy current residual of b = 1000 s/mm^2. B: eddy current residual of b = 3000 s/mm^2. C: eddy current residual normalized to Stejskal-Tanner waveform. D: eddy current residual ratio of b = 3000 s/mm^2 to b = 1000 s/mm^2.

In comparing the eddy current reduction, TRSE, single bipolar, and dual bipolar were normalized to Stejskal-Tanner. The single bipolar and dual bipolar reduction are monotonic decreased when the time constant increased. They have around 50 % reduction with a time constant of 30 ms and around 80 % with a time constant of 100 ms. The TRSE

reduction has a turning point and global minimum at a time constant of 20 ms with a reduction of more than 90 % and gradually increases to 80 % with a time constant of 100 ms.

The residual increment is calculated by dividing the b = 3000 s/mm^2 by b = 1000 s/mm^2. The increments are larger than 1.0 for all waveforms within the intermediate time constant range. Three waveforms, including Stejskal-Tanner, single bipolar, and dual bipolar, are monotonically increased with the time constant. At the time constant of 100 ms, the residual grows to 1.48 for Stejskal-Tanner, 1.70 for single bipolar, and 1.86 for dual bipolar. TRSE is not monotonically increased. There is a global maximum with a ratio of 3.5 at the time constant of 20 ms, a local minimum of 1.45 at the time constant of 60 ms, and a reach of 1.7 at the time constant of 100 ms. Note that although a high increase ratio of 3.5 at the time constant 20 ms for TRSE, it is also the global minimum of eddy current reduction.

Raw diffusion-weighted images (DWI) of Stejskal-Tanner ss-EPI, TRSE ss-EPI, and VAT-PSF-EPI are shown in Figure 3.17. A representative imaging slice of each sequence was with b = 3000 s/mm^2, and the video of all 30 diffusion directions is included in Supplementary Video 1. In Stejskal-Tanner ss-EPI, severe eddy current-induced image distortion, including shearing, scaling, and shifting, can be observed on top of susceptibility-induced distortion. For TRSE ss-EPI, eddy current distortion is reduced with a lower level of susceptibility-induced distortion than SRSE ss-EPI. In contrast, no distortion induced by eddy current or susceptibility can be observed in VAT-PSF-EPI.

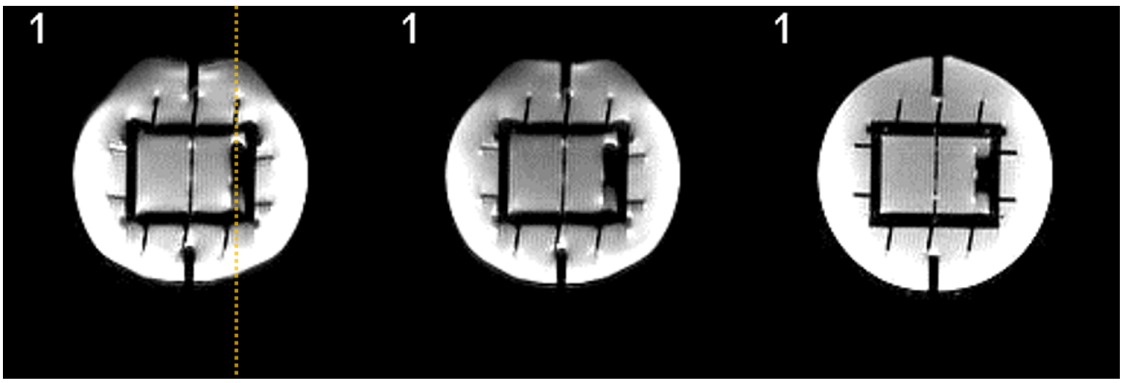

Figure 3.17: Raw images of DWI. DWI from left to right is EPI, TRSE, and VAT-PSF-EPI. The animation of all 30 diffusion directions that shows eddy current signal variation and image distortion is in the attachment. The orange dot line is the location of the plotting signal variation for Figure 3.18.

The image stacked by plotting the signal profile of b = 500, 1000, and 3000 s/mm^2 along the EPI phase encoding direction for all 30 DWIs is shown in Figure 3.18. Image profiles were plotted at the x = 100 pixels as the orange dotted line in Figure 3.17. It can

be seen that signal variation became large when the b-value (diffusion gradient amplitude) increased. In Stejskal-Tanner ss-EPI, the signal variation is already prominent in b = 500 s/mm^2. For example, an apparent downward signal shift, which is the tenth diffusion direction (-0.33, 0.96, -0.11), can be observed. The same diffusion direction in the TRSE ss-EPI with upward shifting can be observed in b = 1000 s/mm^2. This shift is barely noticeable in the VAT-PSF-EPI, even in b = 3000 s/mm^2. Note that the pattern of eddy current distortion in VAT-PSF-EPI is closer to Stejskal-Tanner ss-EPI with a much smaller quantity but is different from TRSE ss-EPI.

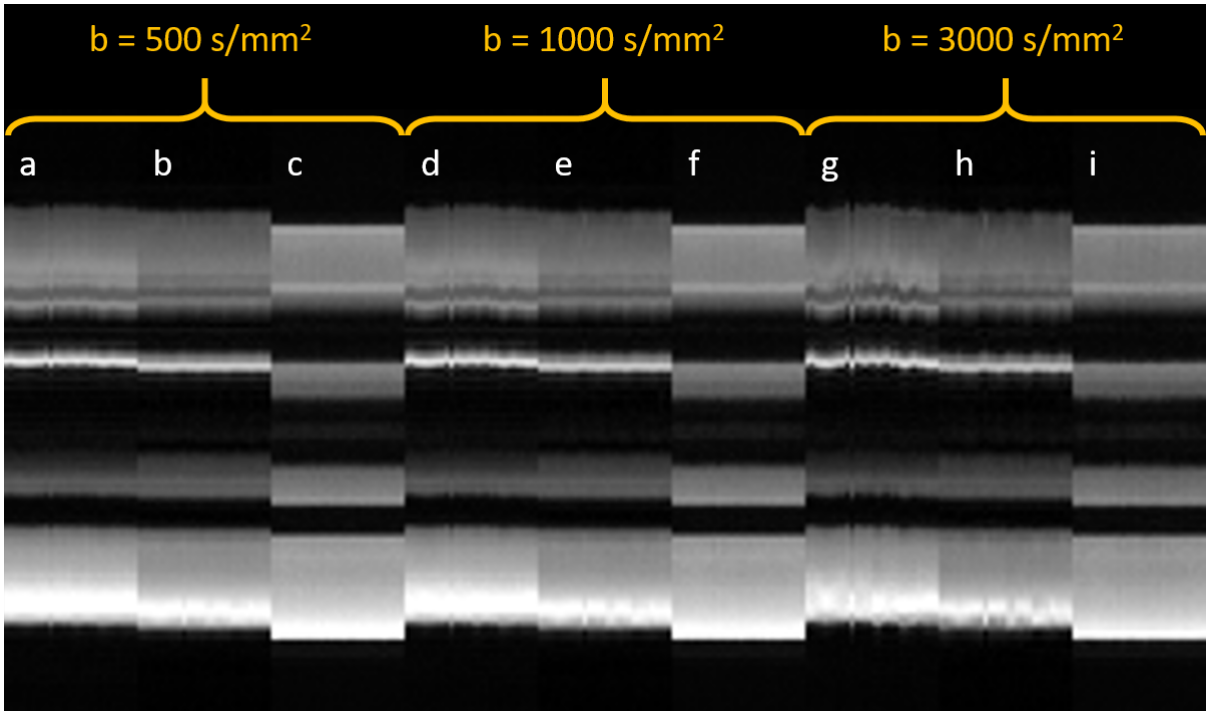

Figure 3.18: Signal variation due to eddy current residual in all 30 diffusion directions. a, d, g: EPI. b, e, h: TRSE. c, f, i: VAT-PSF-EPI. The profile is plotted along the orange dot line in Figure 3.17.

The numerical evaluation of signal variation is shown in Figure 3.19. In Figure 3.19A, the relative signal standard deviations of the three sequences are compared via the coefficient of variation (CV) map in a representative slice of b = 3000 s/mm^2. The CV is the highest in the Stejskal-Tanner ss-EPI among the compared sequences, especially at boundaries. In the TRSE ss-EPI, CV is overall reduced. In VAT-PSF-EPI, CV is further reduced, with a few spots remaining in associating positions of high through-plane distortion. Note that extra signal variations can be observed from the boundaries.

Figure 3.19B shows a CV plot with b-values from 500 s/mm^2 to 3000 s/mm^2 in averaging all 25 slices. Stejskal-Tanner ss-EPI has the highest CV all over the b-values, from 3.8 % to 8.7 %, corresponding to the measured b-values from low to high. In TRSE ss-EPI, the CVs are reduced compared to Stejskal-Tanner ss-EPI, from 2.7 % to 5.0 %. The CV reduces more with higher b-values. VAT-PSF-EPI's CVs are low compared to TRSE and

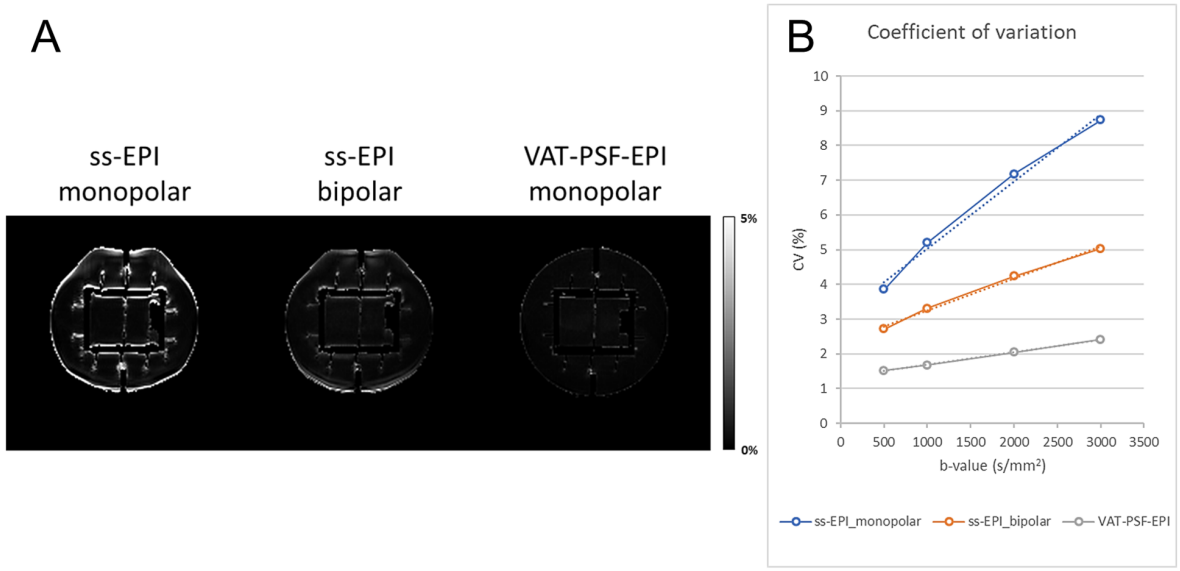

Figure 3.19: Quantifying eddy current signal variation of the acquired sequences. A: coefficient of variation (CV) map. B: CV plot. The obtained sequences are Stejskal-Tanner EPI (monopolar ss-EPI), TRSE (bipolar ss-EPI), and VAT-PSF-EPI (monopolar).

Stejskal-Tanner ss-EPI, with values from 1.5 % to 2.4 %. Once more, CV reduces more with higher b-values compared to TRSE ss-EPI and much more than Stejskal-Tanner ss-EPI. The measured data shows that the CV of VAT-PSF-EPI with b = 3000 s/mm^2 is slightly lower than b = 500 s/mm^2 in TRSE ss-EPI. Note that the CV of baseline b=0 VAT-PSF-EPI images was 1.5 % and comparable to b = 500 s/mm^2 images in VAT-PSF-EPI.

If linear fittings of each sequence to diffusion gradient amplitude (instead of b-value) is made, the relative slope of Stejskal-Tanner ss-EPI, TRSE ss-EPI, and VAT-PSF-EPI is 1.0:0.47:0.18.

The CV plots for the post-processing methods and the application of their best performance in all three sequences are shown in Figure 3.20. In Figure 3.20A, both FSL eddy_correct and FSL eddy were applied to correct the eddy current in Stejskal-Tanner ss-EPI. The CV after these corrections is smaller than before the correction. CV reduces more in the high b-values for both methods. In comparison, the eddy_correct has a much higher performance of eddy current distortion reduction than eddy. The CV curve to b-values in eddy_correct is almost parallel to eddy; however, the CV has an average 60 % reduction. Among the two interpolation methods in FSL eddy_correct, the trilinear interpolation performs slightly more than spline interpolation in the high b-values. The difference can only be observed at the b-value 3000 s/mm^2.

In Figure 3.20B, the comparison of applying trilinear FSL eddy_correct in all three sequences, including VAT-EPI extracted from VAT-PSF-EPI data, is displayed. After

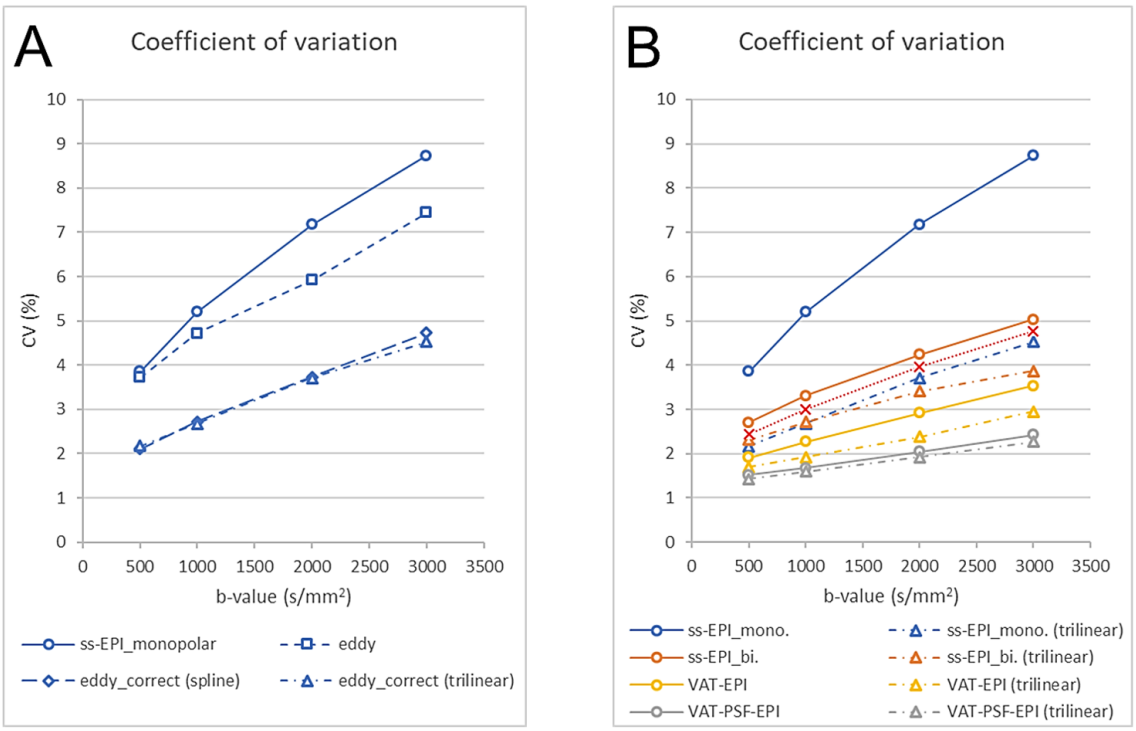

Figure 3.20: Quantifying eddy current signal variation of the post-processing registration methods. A: CV plot of the monopolar EPI with the registration methods, i.e., FSL eddy_correct and eddy packages. B: CV plot of all acquired sequences with the post-processing method FSL eddy_correct.

FSL eddy_correct correction, the CVs are reduced for all acquired sequences, including VAT-EPI. The CV reduction averaging with all b-values is 47 % for Stejskal-Tanner ss-EPI, 19 % for TRSE ss-EPI, 17 % for VAT-EPI, and 5 % for VAT-PSF-EPI. It can be observed that the CVs of VAT-EPI and VAT-PSF-EPI without correction are lower than those of both ss-EPI sequences with correction.

The PSF displacement or distortion measurement of VAT-PSF-EPI in the unit of the pixel is summarized in Table 3.3. The b = 0 image has 1.06 pixels distortion, including the susceptibility distortion and the eddy current distortion from the EPI encoding gradients. The distortion increases gradually with b-values increase and reaches 1.39 pixels in b = 3000 s/mm^2. The relative distortion is 0.47 pixels in b = 500 s/mm^2 and doubles when b = 3000 s/mm^2.

Table 3.3: Quantifying eddy current image distortion of VAT-PSF-EPI with different b-values. The values are measured from the PSF maps.

	b = 0	**b = 500 s/mm²**	**b = 1000 s/mm²**	**b = 2000 s/mm²**	**b = 3000 s/mm²**
PSF displacement [pixel]	-1.06 to 0.81	-1.12 to 0.88	-1.20 to 1.04	-1.29 to 1.22	-1.32 to 1.39
Relative PSF Displacement [pixel]		-0.47 to 0.47	-0.56 to 0.56	-0.66 to 0.84	-0.77 to 0.94

The *in vivo* dMRI results of rapid 5-shots *in vivo* VAT-PSF-EPI with ss-EPI, TRSE ss-EPI with topup, and TRSE rs-EPI are shown in Figure 3.21. All images were acquired

with 1.4 mm isotropic resolution and a GRAPPA factor 4. At the 7 T human scanner, even with a GRAPPA of 4, the image distortion is still apparent, especially close to the sinus (e.g., frontal sinus, red arrows). By using the rs-EPI sequence or FSL topup, susceptibility-induced geometric distortion is reduced compared to ss-EPI. The rs-EPI corrects the distortion in a reduction manner, while the topup generates the virtual undistorted image via different phase encodings. As a result, in the severely distorted regions, the rs-EPI has similar distortion patterns to ss-EPI with a reduced amount, while the topup has aliasing artifacts (yellow arrow). In addition, the image blurring in the topup due to the uncorrected distortion is on top of the initial T_2* blurring of ss-EPI. Thus, the corrected images look more blur than the ss-EPI. Although no extra eddy current correction occurred, the proposed method well corrects the susceptibility and eddy current-induced distortion. Further, the FSL top-up correction for ss-EPI took 20 minutes post-processing.

High-resolution DWI results of 1.0 mm isotropic are shown in Figure 3.22. It can be seen that the image distortion of ss-EPI is more severe than the previous 1.4 mm results (red arrows). The geometric fidelity is improved after the topup and eddy correction. However, the aliasing artifact exceeds the 1.4 mm result above, which is the unwrapping error. At the same time, distortion is reduced in rs-EPI despite the apparent distortion residual. In contrast, VAT-PSF-EPI processes high geometrical fidelities as TSE reference images. Moreover, the topup and eddy correction for ss-EPI processed 1 hour 20 min, while it was 13 minutes of eddy correction for rs-EPI. The BF score averaging of all acquired slices was 0.84 for ss-EPI, 0.89 for topup correction, 0.90 for rs-EPI, and 0.94 for VAT-PSF-EPI with reference to the TSE image.

High-resolution *in-vivo* DTI results acquired with the highly accelerated VAT-PSF-EPI sequence are shown in Figure 3.23. Very high in-plane ($0.7 \times 0.7 \times 2.8$ mm^3, top row) and high isotropic resolutions (1.17 mm^3, bottom row) demonstrate variants of the proposed method. These resolutions were not previously acquired for VAT-EPI due to the server image blurring. The anatomical structures in T_2-weighted (b = 0) and DW images are very well-matched with the reference T_1-weighted images. Upon closer inspection, the high in-plane resolution imaging provided finer anatomic details, while the isotropic resolution images showed reduced through-plane partial volume effects. For instance, gyrifications are better characterized in the former protocol (arrows in the top row). White matter nerve tracts of the limb of the internal capsule or the anterior thalamic radiation in the striatum are better distinguishable in the later protocol (arrows in the bottom row). Note that minor artifacts can be seen in both b = 0 and DW images in the frontal regions and skins.

Figure 3.24A shows the SNR change of PSF-EPI and VAT-PSF-EPI when varying the R_{res} factor by keeping the R_{PSF} to 1. In PSF-EPI, the SNR generally decreases when the R_{res} increases, except from the R_{res} 1 to 3 in the GRAPPA 1 and 2 data. In addition, the

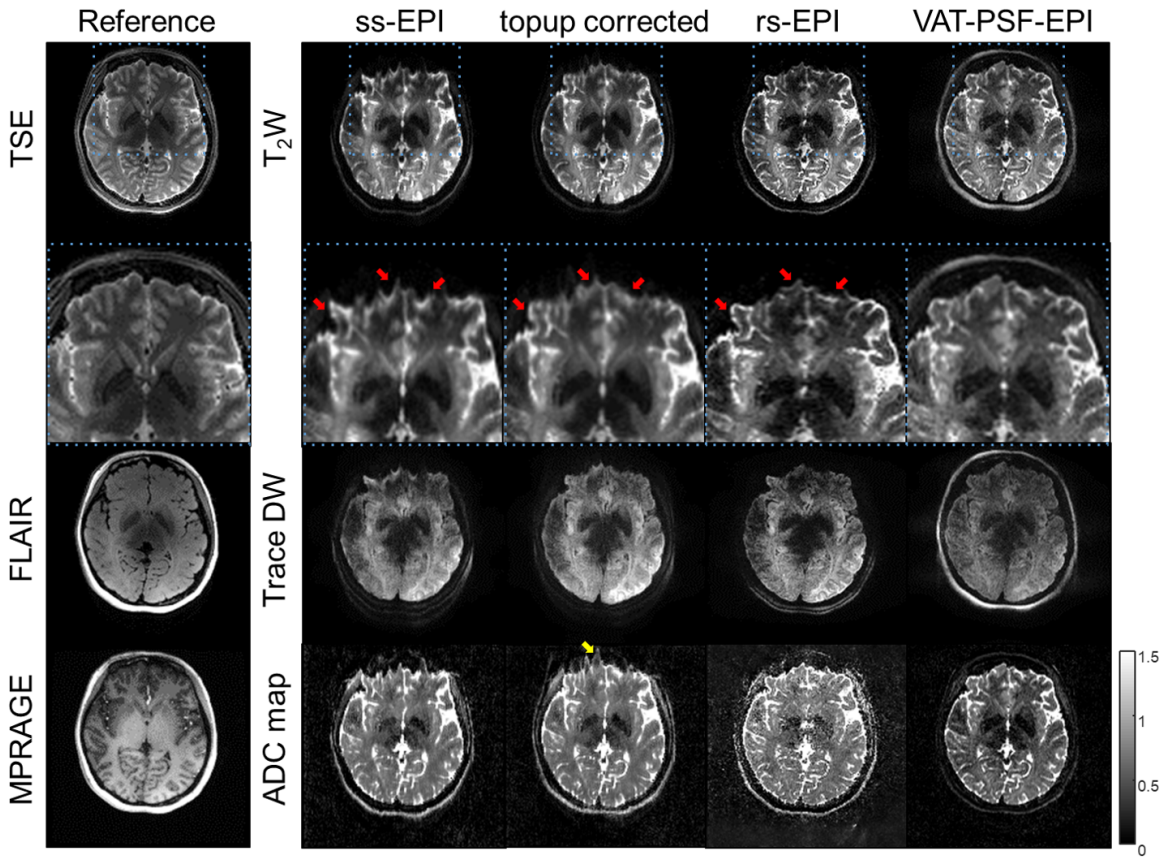

Figure 3.21: Image comparison of *in vivo* human brain diffusion images with 1.4 mm^3 resolution. All sequences use GRAPPA 4. ss-EPI, topup, and rs-EPI uses TRSE to minimize the eddy current, while VAT-PSF-EPI uses a monopolar diffusion gradient. Despite the TRSE and a high GRAPPA factor of 4, ss-EPI shows severe image distortion (red arrows). The post-processing method FSL topup and multi-shot method rs-EPI (minimum available seven shots) improve distortion but cannot eliminate it. In FSL topup correction, the ADC map shows typical errors of the post-processing method due to the uncorrected image distortion (yellow arrow). In contrast, the five shots VAT-PSF-EPI correct distortion from various sources described in the context.

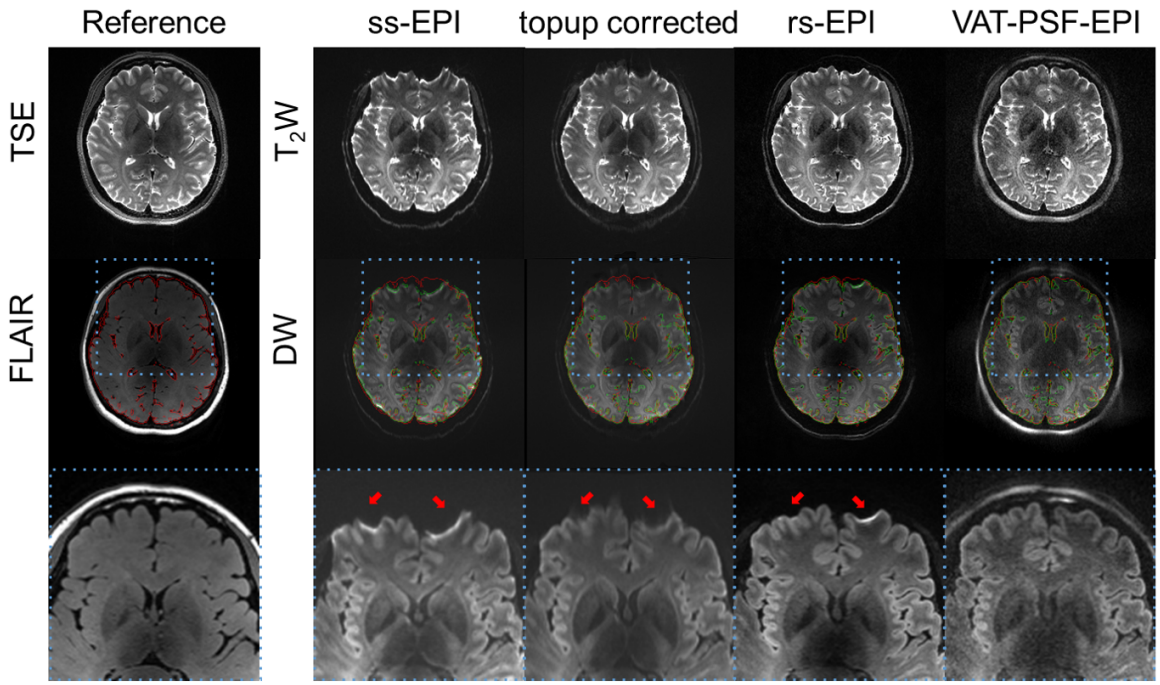

Figure 3.22: Image comparison of high-resolution diffusion images with 1.0 mm^3 resolution. Image distortion is higher in the high-resolution imaging (red arrows). As a result, the distortion residual in the post-processing and reduction methods is increased. In comparison, VAT-PSF-EPI can still correct the distortion well in a scan time similar to rs-EPI without post-processing susceptibility and eddy current correction. The post-processing time for high-resolution imaging can take hours, even with detailed masking. The Sobel filter generates the contour; red is from TSE, and greens are from EPIs. The BF score is 0.84 for ss-EPI, 0.89 for topup, 0.90 for rs-EPI, and 0.94 for VAT-PSF-EPI, where 1.0 is a perfect match.

SNR decrease with R_{res} is more prominent when higher GRAPPA factors are used. In contrast, VAT-PSF-EPI's SNR generally increases with R_{res} except for the R_{res} larger than 3 in GRAPPA 4 data. For the relative SNR of VAT-PSF-EPI to PSF-EPI, it is 0.32 for GRAPPA 1, 0.40 for GRAPPA 2, and 0.54 for GRAPPA 4 when the R_{res} under sampling is not used ($R_{res} = 1$). With the R_{res} factor 10, the SNR ratio became 0.77 for GRAPPA 1, 0.91 for GRAPPA 2, and 1.05 for GRAPPA 4.

Figure 3.24B displays the SNR efficacy (SNR per shot) when the maximum R_{PSF} is determined before the R_{res}. The available R_{PSF} factor of VAT-PSF-EPI to PSF-EPI is 4.42 $\pm$ 0.16, and the available ETL for both sequences is 28 in all GRAPPA factors. Under these conditions, the SNR of VAT-PSF-EPI is 0.61 $\pm$ 0.01 compared to PSF-EPI for the tested GRAPPA factors. By dividing each SNR by shot number, the SNR efficacy of VAT-PSF-EPI to PSF-EPI is 2.2 for GRAPPA 1, 2.1 for GRAPPA 2, and 1.4 for GRAPPA 4.

The *in vivo* DW images with and without 1-D Nyquist ghost correction are shown in

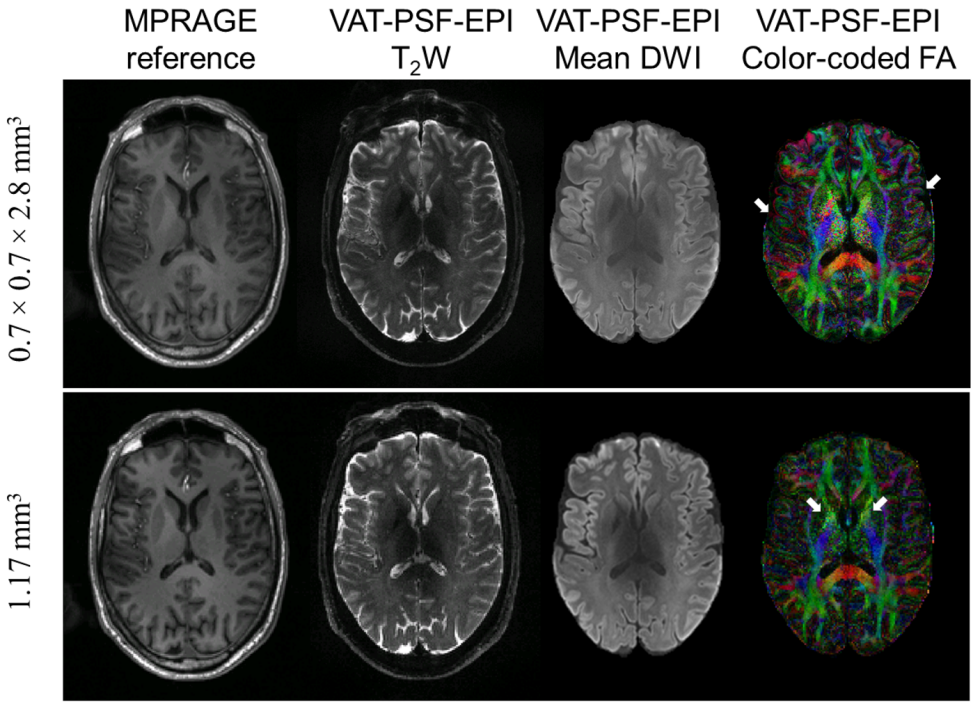

Figure 3.23: High-resolution *in vivo* human brain images acquired with the proposed VAT-PSF-EPI sequence in two resolutions, $0.7 \times 0.7 \times 2.8$ mm^3 (top row) and 1.17 mm isotropic (bottom row). Columns from left to right show reference T_1-weighted MPRAGE images, T_2-weighted images, DW images, and color-coded FA maps. T_2-weighted images, DW images, and color-coded FA maps. High in-plane resolution can better resolve fine structures in the cortex (arrows in the top row). In contrast, high-resolution isotropic imaging can better resolve deep nuclei (arrows in the bottom row).

Figure 3.25. Even though the VAT well corrects the on-resonance fat signal of the scalp, certain bright ghosting can be seen. In the images with Nyquist ghost correction, the fat Nyquist ghost signal is less pronounced and less than 10 % of the signal than the uncorrected images. However, their signal strength is comparable or stronger to the water signal in DWI, which is potentially confounding. On the other hand, those faint signals in the Nyquist ghost-corrected images are more pronounced at the exact location when the Nyquist ghost correction is skipped. Those ghosting in the VAT-PSF-EPI have the same positions as in the VAT-EPI.

The phantom images of T_2W and DWI with and without fat suppression are shown in Figure 3.26. The same results as in the *in vivo* images show that the VAT corrects both susceptibility and fat signal. However, the Nyquist ghosts of oil are presented in the DWI with a signal strength comparable to that of the water in both images of VAT-EPI and VAT-PSF-EPI. The on-resonance fat signal and the Nyquist ghosts are gone with the spectral fat suppression.

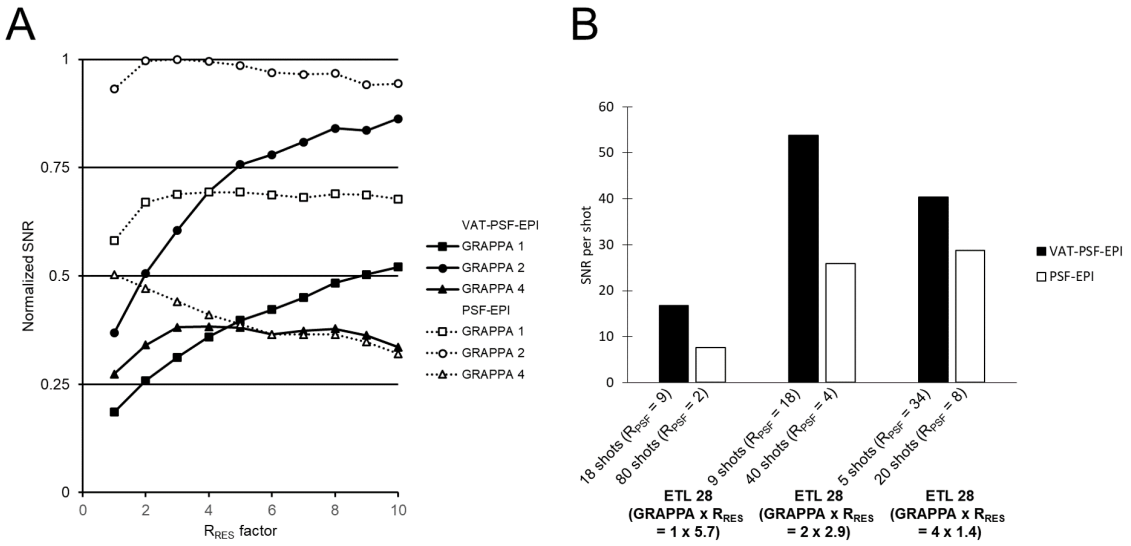

Figure 3.24: SNR improvement by reducing the EPI phase-encoding resolution (R_{res} factor). A: Normalized SNR with the change of R_{res} in the full-PSF sampled data ($R_{PSF} = 1$). B: SNR efficacy by the optimization order of maximizing the R_{PSF} factor first and then the R_{res}. Note that the final image resolution of VAT-PSF-EPI and PSF-EPI are not changed by increasing R_{res}. However, the available PSF acceleration (R_{PSF}) may be reduced with high R_{res}.

In Figure 3.27, fat through-plane artifact and Nyquist ghosting in VAT-PSF-EPI are demonstrated together with their suppression. In Figure 3.27 A and B, although the in-plane (x, y) image distortion in VAT-PSF-EPI is well corrected compared to in EPI, a few signals are related to the through-plane distortion (red arrows). In addition, faint fat Nyquist can also be observed (yellow arrow). By reformatting through-plane (z,y), through-plane distortion is more apparent with a maximum of 1 pixel (1 slice) of the shift. Both artifacts are minimized when combining the differencing RF bandwidth in 90° and 180° RF pulses (Figure 3.27 C).

High resolution (1.17 mm^3) and very high in-plane resolution ($0.7 \times 0.7 \times 2.8$ mm^3) DTI results scanned by the VAT-PSF-EPI sequence are shown in Figure 3.29 and Figure 3.28. Compared with the reference undistorted T_1W MPRAGE image and distorted EPI, in-plane image distortion in VAT-PSF-EPI is well corrected. In addition, no through-plane artifact or Nyquist ghost signal from the high off-resonance content of fat can be observed.

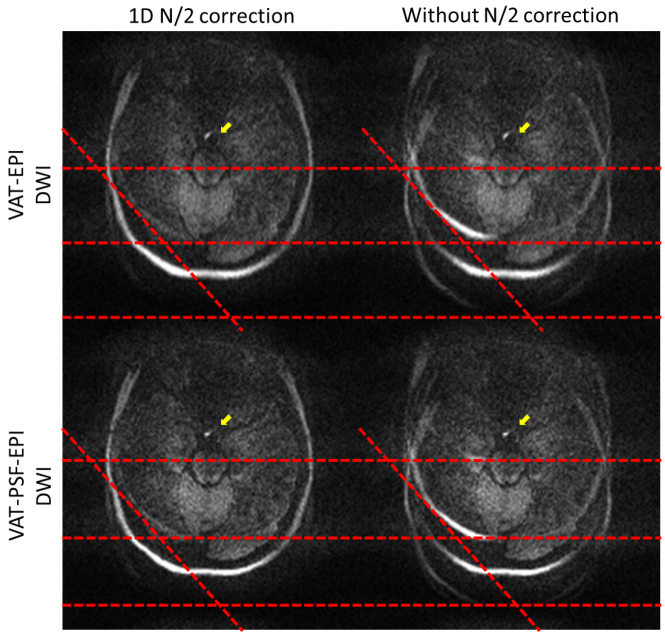

Figure 3.25: Demonstration of the faint artifacts from the fat content in VAT-PSF-EPI. The dashed lines label the positions of the EPI Nyquist ghost, while the yellow arrows label the through-plane distortion. Both fat signals can lead to confounding pathological signals in the DWI, especially when the b-value is high.In addition, turning off the Nyquist ghost correction helps locate the Nyquist ghost. Also, the ghosting shown in the VAT-EPI image proves that they are not the PSF over-accelerated artifact (as shown in Figure 3.9).

3.4 Discussion

3.4.1 Assessment of Susceptibility Distortion Correction: Comparison of Full PSF Sampled VAT-PSF-EPI and PSF-EPI

Image distortion is one of the most significant challenges in ultrahigh field MRI, especially for the fastest sequence ss-EPI. Among the sources of distortion, air-tissue susceptibility is one of the three primary sources in the human 1H MRI. The first experiment uses a structured silicone oil phantom at a 7 T human scanner to study susceptibility distortion correction in the ultrahigh field. The proposed fast multi-shot EPI method, VAT-PSF-EPI sequence (with spin echo signal), is extensively examined for the achievable PSF acceleration factor in correcting the susceptibility distortion. Within the study, the first difficulty was quantifying the distortion and blurring amount separately. However, the common methods cannot delineate the huge distortion and blurring well. A reliable method must be established. PSF mapping was used to quantify the EPI distortion and blurring. Similarly, it is used in the current study to quantify the PSF in VAT-EPI because the achievable acceleration in VAT-PSF-EPI is closely connected to the effectiveness of distortion suppression and accompanied blurring in VAT-EPI. In this study, blurring

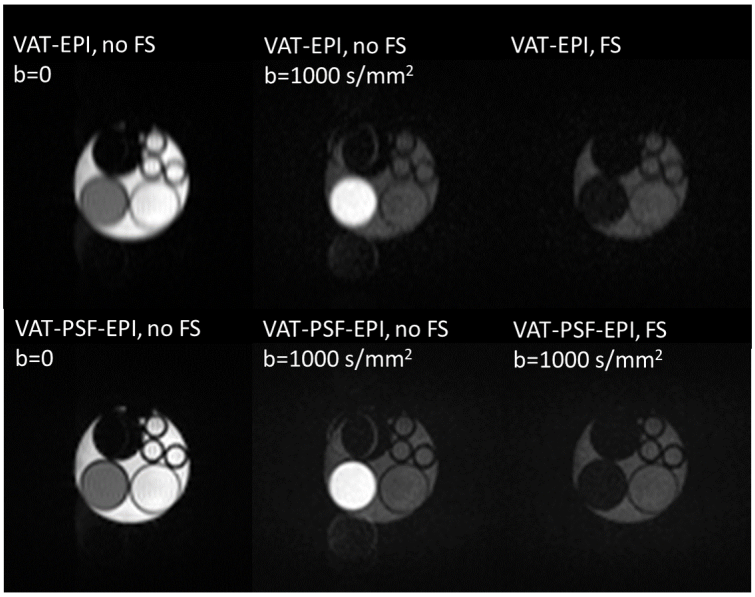

Figure 3.26: Oil Nyquist ghost artifacts in VAT-PSF-EPI. Similar ghosting in phantom than *in vivo* imaging excludes the source of the artifact from the subject movement.

produced from VAT is quantified for the first time via the PSF mapping method. After the distortion and blurring quantification process was established, it was found that the distortion suppression of VAT-EPI and the accompanied blurring had significant inconsistency than found in the literature [90, 106]. The VAT blurring was reduced when higher GRAPPA factors were applied but not further reduced when the slice thickness was increased. Also, the description of VAT-EPI in the literature emphasized the importance of excitation RF pulse. However, it was found that the refocusing of the RF pulse in VAT-EPI also significantly influences the optimal VAT view angle, which will be described later. At the moment, excitation and refocusing RF pulses were kept the same for simplification. In order to solve the optimal view angle's inconsistency and complete the VAT-EPI theory, three different experiments were designed to isolate the parameters that may influence the view angle. Ultimately, these developments are combined to establish the VAT-PSF-EPI theory and produce a highly accelerated susceptibility distortion and blurring corrected images. The achieved acceleration factor in the corrected images in VAT-PSF-EPI is then compared to those in PSF-EPI.

The typical image quality control methods are registration, PSF simulation, and human scoring. Among these methods, the registration method is an indirect quantification method. It requires a reference undistorted image, usually an extra scan of a structural image or an atlas. However, the error may be raised in the algorithm due to significant

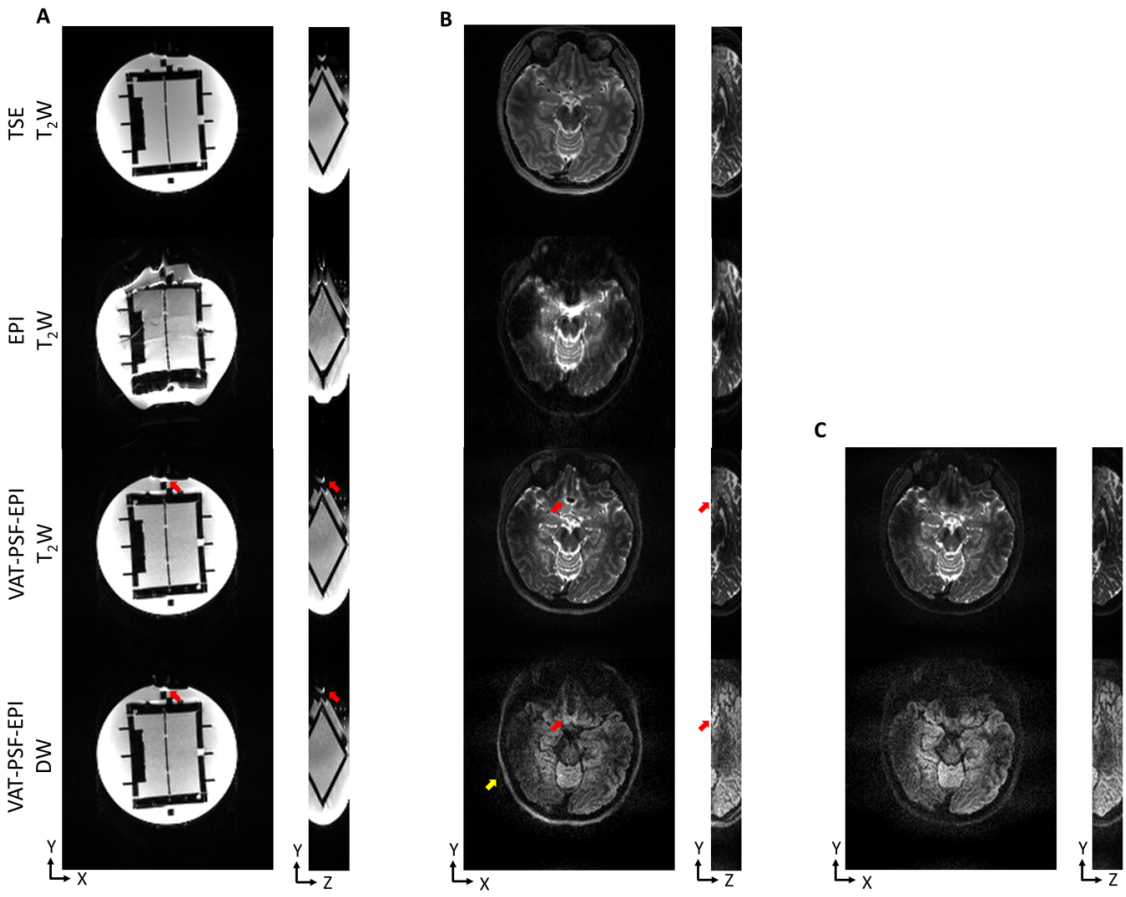

Figure 3.27: Artifact suppression in VAT-PSF-EPI. Faint fat Nyquist ghosting (yellow arrow) and minor through-plane distortion (red arrow) are suppressed using the RF differencing method. The TE is also reduced.

differences in distortion, intensity, and contrast between the reference and distorted images. Compared to the PSF mapping method, an undistorted reference image comprises a series of distorted images in the acquired data. The intensity displacement and spreading can be quantified to the extension of the number of distorted images for a complete PSF measurement. On top of that, the contrast between the reference images and the distorted ones was the same due to the same TE and TR. Therefore, PSF mapping allows accurate measuring of separated distortion and blurring unless the off-resonance is larger than the field of view within an imaging slice. In principle, the PSF mapping method can be applied to different readout trajectories (e.g., EPI, Cartesian, radial, and spiral) to measure the PSF [102].

In the independent PSF measurement of susceptibility distortion, EPI without GRAPPA has more than 30 pixels or 4.8 cm voxel displacement locally. This high distortion amount is attributed to the low phase-encoding bandwidth (7.8 Hz). The distortion is inversely proportional to the GRAPPA factors, which can be seen as the increase of effective bandwidth because of the rise in the phase-encoding gradient amplitude. However, even

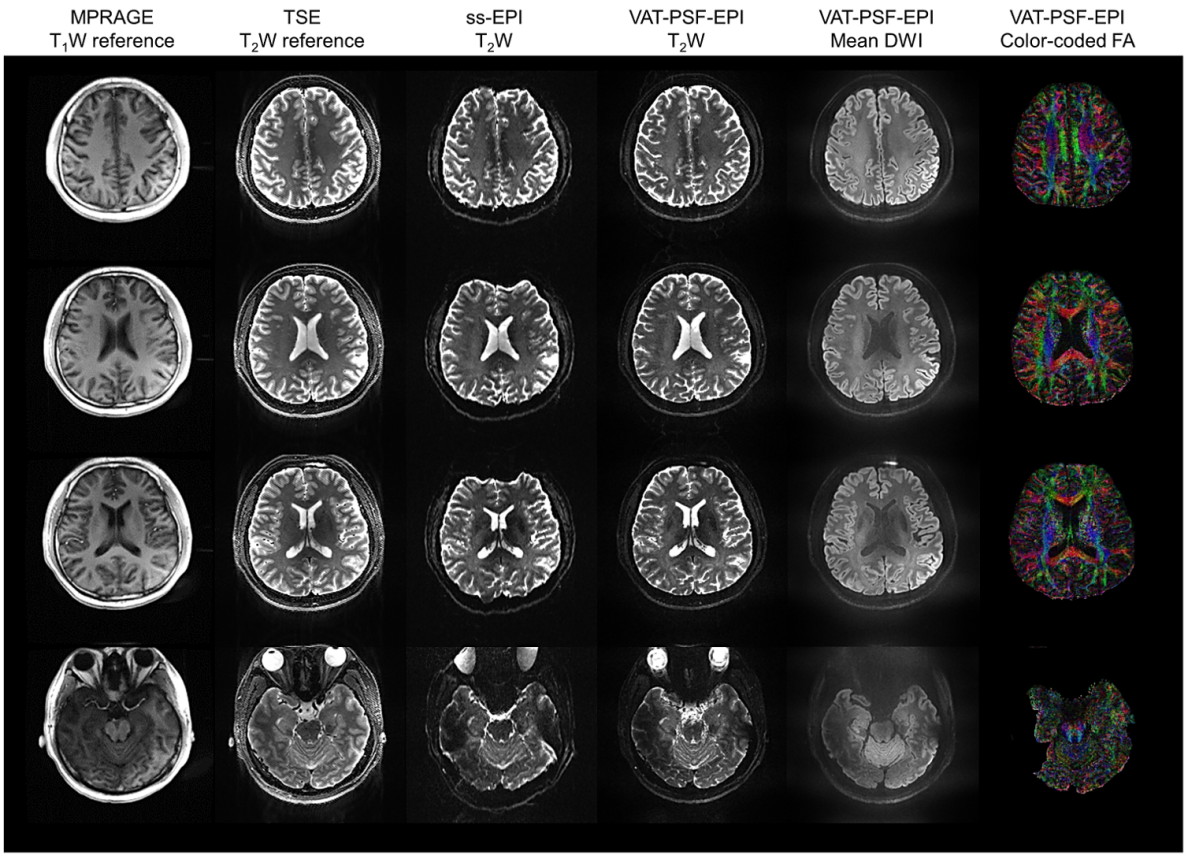

Figure 3.28: High isotropic resolution diffusion imaging using VAT-PSF-EPI (1.17 mm^3) incorporating the SNR improvement and artifact suppression methods.

with a high GRAPPA factor of 4, the distortion can still be more than 8 pixels or 1.2 cm. This means that the susceptibility distortion in EPI needs to be corrected. The measured local distortion is way lower than the expected susceptibility distortion of 9 ppm between silicone oil and air. It is likely due to the good shimming, in which the FWHM is roughly 30 to 60 Hz (0.1 to 0.2 ppm) measured on the scanner's interactive shimming. In VAT-EPI, distortion was not eliminated with the optimized VAT gradient amplitude, which differs from the assumption. Nevertheless, VAT performs very well considering distortion suppression even without GRAPPA (1.52 pixels). The VAT-EPI distortion suppression was 94.5 ± 0.3 % compared to distortion measured in EPI regardless of the GRAPPA factor. It may be converted to an 18.2-times higher effective bandwidth ratio for all GRAPPA factors. Considering only distortion suppression, the GRAPPA 1, 2, and 4 in VAT-EPI are equivalent to the GRAPPA factors of 18.2, 36.4, and 72.8 in EPI. By the time of the study, such a high GRAPPA factor is impossible. Moreover, although the object-independent field inhomogeneity was not measured independently of susceptibility variation, it is relatively small and contained in the measured PSF displacement. With passive and active shimming, the modern magnet can reach less than 0.1 ppm object-independent field inhomogeneity. Thus, the proposed method can also be used to correct

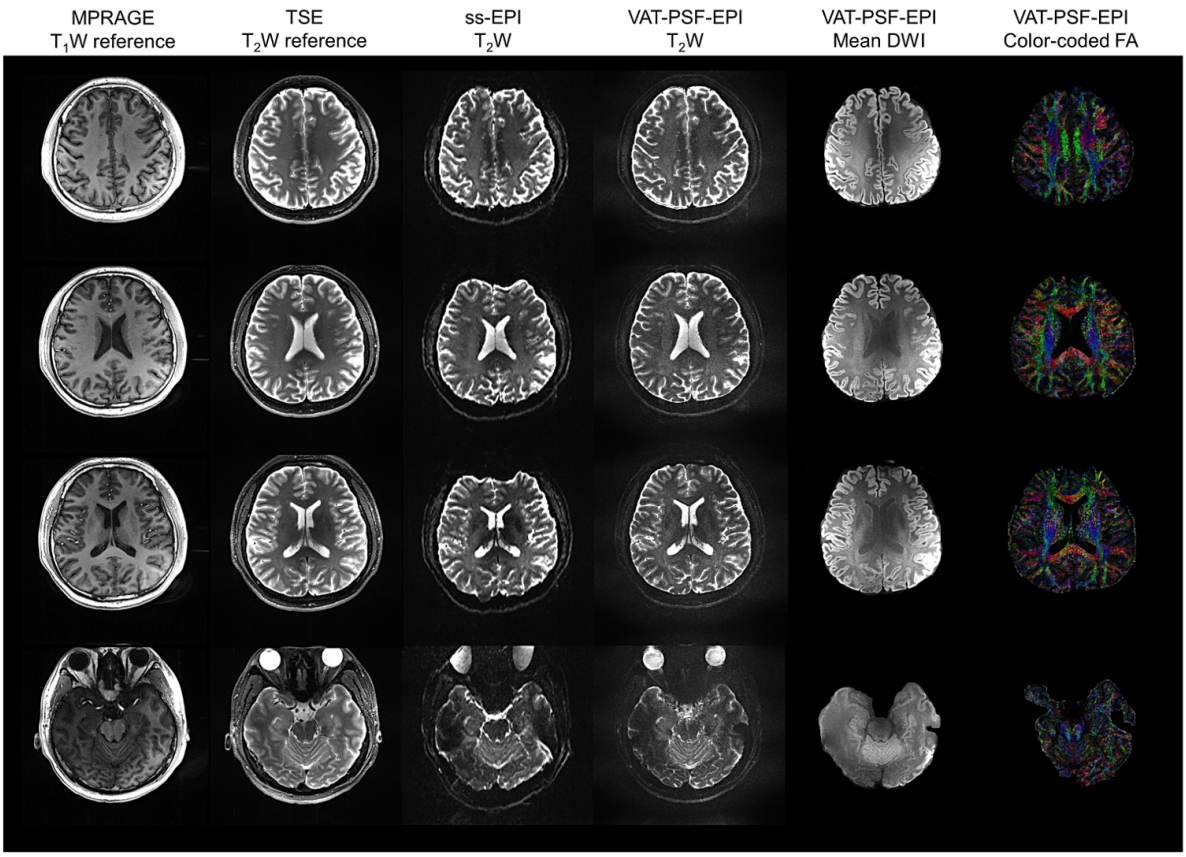

Figure 3.29: Very high in-plane resolution diffusion imaging using VAT-PSF-EPI ($0.7 \times 0.7 \times 2.8$ mm^3) incorporating the SNR improvement and artifact suppression methods.

it.

In further investigating the residual distortion, the distortion distribution in VAT-EPI is very different than in EPI. In EPI, the distributions with various GRPPA factors are similar, with only the amount scaled differently. In contrast, the high distortion areas in VAT-EPI are more concentrated at the inner structure boundaries. The distortions in those areas decrease more with higher GRAPPA factors than in other areas. These remaining distortions in VAT-EPI are considered residual distortions in the current study and may be attributed to the through-plane distortion. Two possible explanations exist for the residual in-plane distortion in the VAT sequences. First, the residuals come from the through-plane distortion (z), and the amount is proportional to the bandwidth ratio of slice selection and correcting direction. In VAT-EPI, it is $\mathrm{BW_{RF}}/2/(\text{effective})\ \mathrm{BW_{PE}}$. Suppose the phase-encoding bandwidth is calculated with the EPI phase-encoding gradient amplitude. In that case, the measured residual distortion in VAT-EPI has the same trend of inverse proportionality to the GRAPPA factors as in the explanation. Still, the amount is an average of 5.3 times smaller. The second possible explanation is that the VAT gradient amplitude contributes to the effective phase-encoding gradient amplitude, which equals

$G_{PE} \times \sqrt{(1 + G_{VAT}^2/G_{PE}^2)}$. In the current sequence implementation, the large constant amplitude of the VAT blip gradient was applied to all GRAPPA factors. Therefore, the effective gradient amplitude roughly remains constant. Although the amount of distortion is closer to the measured values in the second explanation, it has a constant effective gradient amplitude instead of the measured inverse proportionality to the GRAPPA factors. Therefore, both explanations must be modified to explain the measured results better. In the current study, the residual distortions are largely corrected by PSF, and further investigation may be out of the scope.

In the blurring quantification, the primary source of EPI blurring is T_2* blurring. The blurring decreases with the increasing GRAPPA factors due to the higher effective bandwidth. If the T_2* blurring is assumed to be the same in both EPI and VAT-EPI, the VAT blurring can be obtained by subtracting total blurring from T_2* blurring from EPI. The VAT blurring is measured as the primary source of blurring in VAT-EPI. The total blurring constitutes 62.5 ± 4.5 % VAT blurring and the rest of T_2* blurring. The VAT blurring is well estimated by the equation given in the theory, which has only a 2.72 ± 1.33 % difference between the analytical and measured values. The VAT blurring can be seen as the signal modulation function in the k_y. A simple simulation has been performed by applying the measured VAT-EPI signal modulation function to EPI. After the Fourier transformations, the images are severely blurred with the same distortion amount (not shown). It confirms that the blurring in VAT-EPI can be characterized by signal modulation function in the k-space.

This study defines the PSF range as adding PSF displacement and width. The distortion in EPI is the major contributor of 90.7 ± 1.1 % of the PSF range, with blurring in the rest. In contrast, blurring is the main contributor to the PSF range in VAT-EPI, which has 79.7 ± 2.9 % out of the total PSF range. In computing the acceleration factor from the measured PSF range, the maximum acceleration factor must be corrected by roughly 10 % due to the neglecting T_2* blurring. In contrast, the maximum acceleration factor VAT-PSF-EPI must be fixed by 20 % of the neglecting distortion. Considering the total PSF range, a correction factor 2 must be applied rather than only the VAT blurring. The theory implies that if the PSF range is tiny (i.e., $\leq$ 0.5 pixels in the current imaging protocol) or signal differences from the reference to the EPI or VAT-EPI are small, the single-shot distortion-corrected VAT-PSF-EPI may be achievable.

The distortion-corrected results showed that even without parallel imaging (GRAPPA 1), the gigantic distortion in EPI and giant blurring in VAT-EPI can be corrected with the full-PSF sampled sequences. Although PSF mapping can correct a huge distortion and blurring, the sequences' speeds may be slow. This implies that applying GRAPPA is necessary for the PSF-corrected EPI sequences in the ultrahigh field. However, the maximum acceleration factor can be achieved differently in PSF-EPI and VAT-PSF-EPI because the PSF range in VAT-EPI is much smaller than in EPI. The measured PSF

range in VAT-EPI is 3.5-fold smaller than in EPI, which can be converted to a faster distortion-corrected imaging speed in VAT-PSF-EPI. In the current prototype sequence implementation, the acceleration factor defines the sequence PSF under-sampling factor instead of the number of shots. Therefore, the 4.0-fold acceleration was imaged instead of 3.5. An acceleration factor with decimals may be possible in a more sophisticated sequence implementation. With the commonly applied large GRAPPA factor of 4, the PSF-EPI [107] can achieve the fastest 20 shots with the 1.4 mm isotropic resolution. For the VAT-PSF-EPI, the fastest of 5 shots can be achieved. Compared to a recent high-performance gradient at 3 T (80 mT/m, 700 mT/m/ms), its echo spacing is 0.44 ms [108]. Due to a lower field and EPI echo spacing, the off-resonance effects are much smaller. However, the 1.4 mm isotropic PSF-EPI achieved to correct the air-tissue susceptibility distortion is 12 shots with GRAPPA 3 or can be converted to 9 shots with GRAPPA 4.

The unresolved distortion with PSF will become an aliasing artifact in the PSF-corrected images. This is mainly due to the over-accelerating of the sequence. The over-accelerated aliasing artifact in PSF-EPI is easy to recognize. The signal missing at the high susceptibility regions will appear at the same readout position but in a different phase-encoding position. It may be challenging to differentiate the aliasing artifact caused by the over-acceleration in the *in vivo* measurement. In the VAT-PSF-EPI, the aliasing artifact is a faint copy of the image (ghosting). Different sources may lead to similar ghosting artifacts, including the EPI Nyquist ghosts, physiologic artifacts, and the reconstruction error. A troubleshooting method of the VAT-PSF-EPI over-acceleration may be performed by changing the accelerating factor. The signal and ghosting position will be changed by adjusting the accelerating factor.

Previously, VAT-EPI was considered only valuable for the thick slice of 4 to 5 mm because the slice thickness is inversely proportional to the view angle or the arctangent of the VAT gradient ratio [90]. This implies that a thin slice will lead to a blurry image. However, the current study shows that the measured blurring amount cannot be explained only by the proportionality of the VAT gradient ratio. For example, the blurring amount is very different from the 1.4 mm^3 with GRAPPA 1 imaging protocol than $1.4 \times 1.4 \times 0.7$ mm^3 with GRAPPA 2, where both have the same VAT gradient ratio of 16.35. It suggests that the image blurring caused by VAT has a linear relationship with the VAT gradient ratio and slice thickness. This is because the slice-selected gradient amplitude changes with the slice thickness change. Therefore, thin-slice applications in VAT-EPI and VAT-PSF-EPI can be valuable despite a high view angle. The blurring corrected by the PSF is also making the high in-plane resolution image meaningful. Compared to a previous ss-VAT-EPI result at 3 T ($3.4 \times 3.4 \times 4$ mm^3), the voxel size (1.4 mm^3) acquired in the current study is around 2.8 times smaller, albeit a slower total acquisition time (fastest five shots).

An additional factor influencing the amount of blurring has been found in VAT-EPI with

the RF TBP experiment, so the achievable sequence acceleration in VAT-PSF-EPI has also changed. In the experiment, except for RF TBP, all other imaging parameters were kept the same, including the RF bandwidth, duration, and VAT gradient ratio. Simultaneously, changing TBP with RF duration affects the slice profile, not RF bandwidth. Therefore, the blurring amount was supposed to stay the same. A similar number of measured PSF displacements implies that all three imaging protocols had the optimal VAT gradient amplitude. However, the PSF width is measured to increase inversely with the TBP factor. A possible explanation is that the effective slice thickness is thicker with a lower TBP factor. Usually, the slice thickness is defined as FWHM in the slice profile, and the low TBP Sinc pulse is less steep in the slice profile. As a result, some intensity spreads more widely than the slice profile, resulting in a larger slice thickness. As in the updated VAT theory, the blurring is more significant with the higher slice thickness. The factor of slice profile change is roughly equal to the PSF width change, and the acceleration also changes inversely accordingly in VAT-PSF-EPI. The current RF bandwidth of VAT-PSF-EPI is set to 130 Hz, which has roughly a 4-fold acceleration than PSF-EPI. However, the minor through-plane distortion can be seen as a trade-off of in-plane distortion. Nevertheless, VAT-PSF-EPI acceleration is higher compared to PSF-EPI unless the RF bandwidth is five times larger than the current setting from the PSF range estimation.

Currently, all experiments have a very long TE of 200 ms. It was for a fair comparison of all imaging protocols. The long TE was mainly to keep the GRAPPA 1 in the same condition as others. In addition, although a naive Sinc RF with a long RF duration was implemented in the current study, a more sophisticated RF design may shorten the TE. An unexpected finding related to the signal is that the SNR of the distortion-corrected images in VAT-PSF-EPI is much lower than in the PSF-EPI. The SNR decrease is 58.0 $\pm$ 9.1 % with a trend that the higher GRAPPA factors decrease less. Such a high SNR reduction has not been reported before in VAT methods and needs further investigation. The study of SNR reduction will be in a later chapter.

To summarize the first assessment, susceptibility distortion correction, VAT-PSF-EPI is verified to effectively correct the air-silicone oil (air-tissue) susceptibility distortion at ultrahigh field 1H MRI. The proposed method can be compared to the composited methods, VAT-EPI and PSF-EPI. On the one hand, VAT-PSF-EPI corrects a giant blurring to those in VAT-EPI. On the other hand, VAT-PSF-EPI accelerates the slow PSF-EPI sequence to up to 4-folds in correcting the susceptibility distortion. In addition, completing the VAT-EPI theory releases the high-resolution isotropic imaging restriction for VAT-PSF-EPI. Matching the sequence acceleration factor with the PSF measurement confirms that the constant-time PSF encoding gradients can accurately measure the PSF other than the EPI sequence. However, the SNR reduction of the sequence must be further investigated.

3.4.2 Assessment of Susceptibility and Chemical shift Distortion Correction

In the second assessment, fat-water chemical shift corrected by VAT-PSF-EPI is evaluated with phantom and *in vivo* T_2 images at 7 T. In the phantom evaluation, VAT-PSF-EPI was first qualitatively compared to ss-EPI and TSE with fat suppression RF pulse either on or off. Then, it was numerically evaluated with different phase-encoding directions for its effectiveness. Next, the view angle tilting gradient is set to deviate from its optimal amplitude to evaluate the robustness of VAT-PSF-EPI. Finally, the *in vivo* human brain data scanned by VAT-PSF-EPI was compared to traditional PSF-EPI for evaluating sequence acceleration.

In the phantom evaluations, susceptibility and chemical shift distortion are noticeable in ss-EPI, even with GRAPPA 4. When the fat suppression was on, VAT-PSF-EPI also corrected the susceptibility distortion in the TSE. However, when the fat suppression is switched off, chemical shift distortion is corrected by VAT-PSF-EPI, showing a small displacement in the read-out direction of TSE. It is due to the chemical shift at 7 T ($\approx$ 1000 Hz) being larger than the TSE's maximum read-out bandwidth (789 Hz). In addition, since the distortion shape differs from the phase encoding directions in EPI, image correction with different directions and polarities may be compared to best evaluate the robustness. Because of a slight chemical shift distortion in TSE, the fat-suppressed TSE was assigned to the reference image. In the current study, VAT-PSF-EPI corrects susceptibility and chemical shift distortion equally well with two-phase encoding directions (A/P and R/L) and their opposite polarities (P/A and L/R). However, there are very faint background artifacts mainly associated with oil signals. These artifacts are due to the non-optimal N/2 correction and GRAPPA reconstruction. Since those artifacts are also in the VAT-EPI images, dealing with them is out of the scope of the current study.

VAT gradient amplitude was slightly changed to evaluate the proposed method's correction effectiveness. For gradient amplitude change up to 5 %, both susceptibility and chemical shift are still corrected well. The chemical shift correction starts to degrade from a 9 % gradient amplitude change, and the oil signal shifts partially. For around 20 % of change, the oil signal shifts by around 1/5 of the reduced field of view. Nevertheless, the image correction of susceptibility distortion has only a minor effect. It can be deduced that up to 5 % VAT gradient variation is not affecting the result, and up to 20 % may be acceptable to correct the susceptibility distortion if an ideal fat suppression is applied. This gradient amplitude variation can be either due to localized changes by the field inhomogeneity or set on purpose for reducing VAT gradient amplitude to reduce signal loss.

In comparing the scan time, VAT-PSF-EPI was scanned by five TR (shots) in 31.5 seconds to resolve the image distortion and blurring. For the given slice coverage (31 slices), ss-EPI had a total scan time of 6.3 seconds for a single TR. In TSE, the turbo

factor was limited, and the TR was elongated for the permitted SAR, leading to a long scan time of 1:04 minutes.

For *in vivo* brain imaging, VAT has suppressed distortion largely in VAT-EPI, including the high susceptibility frontal region and fat tissue under the scalp. The distortion is uniformly low for optimized VAT suppression, and the blurring is also uniformly distributed for brain and fat tissues. Even though the blurring increased by 1.8 times more than EPI, the needed number of shots decreased, which is similar to the phantom result for susceptibility correction in the previous section. While the resulting PSF range was dominated by the PSF displacement or EPI image distortion in the traditional PSF-EPI, in the VAT-PSF-EPI, the resulting PSF range was dominated by the PSF width or VAT-EPI image blurring. The proposed method accelerates by 4.7-fold for correcting susceptibility distortion and 14-fold for correcting fat chemical shift compared to PSF-EPI.

To summarize the second assessment, susceptibility and chemical shift distortion correction, VAT-PSF-EPI has demonstrated its robustness and effectiveness in correcting fat-water chemical shift distortion. On the one hand, the proposed method can correct image blurring for VAT-EPI. On the other hand, the method accelerates largely to the original PSF-EPI. To the author's knowledge, no method other than VAT can correct this significant distortion in EPI. Therefore, the method is particularly beneficial for applications where the strong distortion comes from static off-resonance.

3.4.3 Simulation of the Eddy Current from Normal and High Diffusion b-values

In this normal to high diffusion b-values simulation, four different diffusion gradient waveforms, including Stejskal-Tanner, TRSE, single bipolar, and dual bipolar, are simulated to evaluate the diffusion weighting efficiency and the eddy current residual.

The results of the diffusion duration simulation demonstrated that Stejskal-Tanner has the highest efficiency in both b = 1000 s/mm^2 and b = 3000 s/mm^2. If the RF and dead time are ignored, TRSE has comparable efficiency with Stejskal-Tanner, as mentioned in O. Heid [109] and Reese et al. [41]. However, the RF and dead time can play a significant role in building diffusion weighting, as mentioned in Weigel et al. [110]. The schematic diagram (Figure 3.5) shows that single bipolar and dual bipolar have not used the RF time for diffusion weighting. TRSE uses the RF duration to build the diffusion weighting, but it is less efficient than in the Stejskal-Tanner. In addition, TRSE needs additional crusher gradients for every refocusing RF pulse, which has a neglect contribution to the diffusion sensitivity. Therefore, the diffusion efficiency in the Stejskal-Tanner remains the highest, followed by the single bipolar with slightly lower efficiency, followed by the low-efficiency TRSE and very low-efficiency dual bipolar. It must be noted that although there is no specificity of GRE or SE for single bipolar here, the relatively high efficiency is only for GRE. As mentioned in Freidlin et al. [111], the GRE-based diffusion sequence will suffer from field inhomogeneity and T_2* dephasing. If the SE-based is used as the other three

waveforms, the TE will deviate from the total diffusion duration by more than twice. In the simulation of diffusion duration prolonged from b = 1000 s/mm^2 to b = 3000 s/mm^2, TRSE prolongs less than the others. This is mainly because of the duration change of each gradient instead of purely extension, and the calculation is done via analytical instead of numerical means. It also explains a slight change of the null time constant in two b-values.

Recently, Aliotta et al. [112] have proposed a modified dual bipolar waveform with a null time constant, which can reduce residual to a similar level compared to TRSE with a reduced TE. It was demonstrated to have a 19% TE reduction compared to the TRSE. However, the requirement for not using partial Fourier acceleration in the EPI phase encoding is rarely met. Later, Shrestha et al. [113] simulated this waveform detailed in two maximum gradient amplitudes (28 and 34 mT/m), two different resolutions (2.0 and 1.5 mm isotropic), without and with the use of partial Fourier (6/8), and then compared with TRSE. When the partial Fourier was not used in the higher resolution protocol, results were similar to the original literature. In the lower resolution without partial Fourier, TE is comparable to TRSE. While the partial Fourier was used, the results changed utterly. The TE of the modified dual bipolar waveform was about 15 % longer than TRSE in all situations. It is because of the intrinsically low diffusion efficiency in dual bipolar compared to TRSE.

In the eddy current residual plot (Figure 3.16), a very high peak at the beginning is with short time constants. The latest gradient switching dominates the initial eddy current polarity and amplitude in the short decay time constants. Consequently, with the same polarity of the first diffusion gradient switching of all simulated gradient waveforms, Stejskal-Tanner has an inversed polarity of the initial residual than the others. Regarding the amplitude, all waveforms were set to have the same constant gradient amplitude. However, the initial peak amplitude was still very different. It is related to the self-cancelation of the latest gradient; the shorter the duration, the better the cancellation, i.e., Table 2.3. The duration of the last gradient for single bipolar required the longest duration and is around 125 % longer than Stejskal-Tanner and dual bipolar and 190 % longer than TRSE. Thus, the initial amplitude from high to low is one bipolar, Stejskal-Tanner, dual bipolar, and then TRSE.

The joint cancelation from prior gradients becomes apparent when the time constant is longer. As mentioned in Alexander et al. [105], the eddy current built by two gradients in Stejskal-Tanner is around doubled than only one gradient owing to the same polarity of both gradients. For single bipolar and dual bipolar, the cumulative eddy current is dramatically reduced compared to Stejskal-Tanner. A similar level of reduction is due to the longer diffusion duration in single bipolar and the shorter diffusion duration but with the same polarity of bipolar gradient pair in dual bipolar. TRSE has the highest reduction in all the simulated waveforms, and the residual quickly falls to the nulling point, followed by an inversed residual polarity. In the intermediate time constant range, the worst TRSE

residual compared to Stejskal-Tanner is 23 % for b = 1000 s/mm^2 and 33 % for b = 3000 s/mm^2.

As expected, the residual in b = 3000 s/mm^2 is larger than in b = 1000 s/mm^2. All of the increase ratios are larger than 1.0, indicating the residuals were larger in b = 3000 s/mm^2 compared to b = 1000 s/mm^2 for all waveforms. The residual plot in b = 3000 s/mm^2 is like an amplified version of b = 1000 s/mm^2 for all tested waveforms. Since the difference of waveform from b = 1000 s/mm^2 to b = 3000 s/mm^2 is only in the diffusion gradient duration, the amplitude was kept the same. Thus, the change in eddy current is solely caused by the longer duration, which indicates fewer cancelation effects.

To summarize, eddy current residuals of different diffusion gradient waveforms were numerically simulated. The simulation leads to a better understanding of the source of eddy current distortion in diffusion MRI with different b-values. In particular, Stejskal-Tanner remains a simple and highly efficient waveform, which needs only 2/3 diffusion duration compared to the TRSE in both simulated b-values. However, the eddy current residual in Stejskal-Tanner is very high compared to the eddy current nulled waveform TRSE. The TRSE has the worst of 1/3 residual in the intermediate time constant compared to Stejskal-Tanner in b = 3000 s/mm^2. The residual in the Stejskal-Tanner of b = 1000 s/mm^2 is even larger than all other waveforms of b = 3000 s/mm^2 in the intermediate decay time constants. Since the proposed VAT-PSF-EPI is hypothesized to correct the diffusion gradient-dependent eddy current distortion, Stejskal-Tanner is chosen as the waveform throughout this thesis for its high efficiency.

3.4.4 Assessment of Susceptibility and Eddy Current Distortion Correction with Varying Diffusion b-values

In the third assessment, a phantom experiment is conducted to examine the effectiveness of VAT-PSF-EPI in eddy current distortion correction by comparing it with established methods qualitatively and quantitively.

For the qualitative comparison, VAT-PSF-EPI showed the slightest distortion among Stejskal-Tanner and TRSE ss-EPI in Video 1. As described in the previous section, reduced eddy current distortion in TRSE ss-EPI is achieved by reducing the eddy current accumulation. Despite having a significantly smaller amount of residual eddy current compared to Stejskal-Tanner, specifically 33% in the time constant of 10 ms, and less than 20% for intermediate and long-time constants in b = 3000 s/mm^2, the distortion remains noticeable with GRAPPA 4. In comparison, minimal distortion can be observed in VAT-PSF-EPI. All distortions, including shearing, scaling, and shifting, are corrected. Furthermore, although image blurring due to eddy current varying during EPI readout hardly differentiates from the T_2* blurring and VAT blurring, those are corrected in the VAT-PSF-EPI. While the diffusion b-value is kept the same (b = 3000 s/mm^2), the b-vector or direction in q-space changes in each video frame. The b-vector changes via varying

gradient amplitude and linear combinations in three orthogonal gradient directions, i.e. (x, y, z). The eddy current residual linearly increases with the amplitude in the simplest eddy current model. Therefore, eddy current correction consistency is also important when evaluating different gradient amplitude or b-values in the same direction.

For the quantitative comparison in image stacks, VAT-PSF-EPI with b = 3000 s/mm^2 shows lower signal variation across 30 diffusion directions in all acquired b-values and is even smaller than TRSE ss-EPI with b = 500 s/mm^2. The observed distortion patterns in (Stejskal-Tanner) VAT-PSF-EPI are similar to Stejskal-Tanner ss-EPI but very different than TRSE ss-EPI. It is due to the polarity of the last diffusion gradient in the Stejskal-Tanner and TRSE gradient waveform. The CV maps and plots have demonstrated results similar to those of the image stacks. In the CV map of b = 3000 s/mm^2, those with high signal variation area are mainly at boundaries. VAT-PSF-EPI produces only minor signal variation in areas associated with high through-plane inhomogeneity. Although Stejskal-Tanner ss-EPI was acquired with GRAPPA 3, signal variation is still expected to be higher than TRSE ss-EPI with GRAPPA of 4. Nevertheless, CV in VAT-PSF-EPI remains noticeably smaller than others. It is worth noting that the CV slope in VAT-PSF-EPI is less than half to TRSE ss-EPI and a quarter to Stejskal-Tanner ss-EPI with a linear fitting to diffusion gradient amplitude, in which slope of 0 (horizontal line) indicates the perfect correction. The high correction consistency with different b-values in VAT-PSF-EPI also explains its lowest distortion in Video 1.

In the CV plot comparing FSL post-processing methods, it is surprisingly observed that eddy performs less than eddy_correct. While the second-level model optimization option was activated in eddy to remedy the non-optimal b-table (non-whole q-sphere) [114], it had slightly improved compared to being deactivated (data not shown). Compared to the literature, the difference may be due to the non-optimal sampling conditions for eddy, while an optimal phantom for eddy_correct simultaneously. In addition, in the two interpolation options within eddy_correct, trilinear interpolation produces marginally higher performance than spline interpolation. However, trilinear interpolation produces more blurring than spline interpolation, which has a similar blurring level as in eddy, as mentioned in Yamada et al. [115]. Although the amount of blurring is not big, it is on the top of T_2* blurring, and eddy current blurring of those blurring cannot be corrected by those methods so far. Furthermore, the performance of eddy_correct is expected to decrease in the *in vivo* experiment because the contrast differences between b=0 and DWI are huge. In such cases, eddy may perform better. Regarding the post-processing time, eddy took ten minutes on a PC and was ten times longer than the eddy_correct in a single shell. In contrast, VAT-PSF-EPI does not need additional processing for eddy current correction.

In the comprehensive CV comparison, CVs are smaller after performing eddy_correct to all sequences. However, the CV reduction amounts differ. The result demonstrates

that traditionally, seeing the amount of registration to b=0 as the ground truth of eddy current correction needs to be revised. For the VAT-EPI extracted from VAT-PSF-EPI, CVs are between TRSE ss-EPI and VAT-PSF-EPI. The result demonstrates that VAT can also correct the eddy current distortion in EPI, which was not observed before. VAT was mainly used to correct traditional TSE sequences with large static distortion, such as chemical shifts and metal artifacts. The relatively small dynamic distortion does not affect the TSE much and, thus, has not been studied. In the VAT-PSF-EPI, the CV before and after correction is minimal. This result suggests that the dMRI data acquired with VAT-PSF-EPI may not require additional eddy current correction.

Another piece of evidence that VAT can correct eddy current distortion is the measurement of image distortion by the PSF method. Both absolute and relative distortion to b = 0 increase with the b-value. However, even if the distortion value is larger than 1.0 pixels, it is not necessary to have distortion or artifacts in the final distortion-corrected image. With the b-value further increased, the PSF range or the summation of distortion and blurring may be larger than the resolving capacity of the current acceleration factor (R_{PSF} = 32 or 5 shots). Nevertheless, it is easy to remedy it by increasing the number of shots in VAT-PSF-EPI. For example, 5-shots VAT-PSF-EPI can resolve b = 3000 s/mm^2 with a PSF range maximum of 2.5 pixels with 160 matrix size. With an increase of VAT-PSF-EPI from 5 shots to 6 shots, 3.0 pixels of PSF range can be resolved, which is more than b = 7000 s/mm^2 from the linear fitting of measured distortion.

VAT-PSF-EPI can be further compared with other PSF-EPI methods. In a previous study, the measured relative distortion was 7.4 pixels for b = 1000 s/mm^2 at 3 T with an ultra-high slew rate gradient system (700 T/m/s) [116]. The high slew rate gradient renders a short diffusion duration and less EPI echo spacing. As a result, eddy current distortion is largely reduced. However, high distortion values from EPI were still measured. Therefore, eddy current distortion may need to be corrected to reduce the image error in the final susceptibility distortion corrected image. In comparison, a 0.94 pixel of relative distortion for b = 3000 s/mm^2 is measured in the current study with a slew rate 200 s/mm^2 gradient system. Around eight times smaller distortion leads to a potentially higher acceleration to the proposed method; thus, no additional correction is needed. Additional calibration data with complex and heavy computation (e.g., $\tilde{1}$ minutes per slice by 20 cores 2.0 GHz workstation) may be necessary for correcting the eddy current distortion for other PSF-EPI methods.

The proposed method is a new approach that partially belongs to the fourth eddy current reduction category. The principal reduction of distortion is via VAT-EPI. The tilting gradient increases the encoding gradient amplitude during EPI phase encoding, thus reducing the effective echo spacing. The multi-shot characteristic of PSF-EPI is not like other multi-shot sequences to reduce echo spacing, but keeping it the same regardless of the number of shots. Further, PSF-EPI corrects residual distortion and blurring. There

are a few advantages of VAT-PSF-EPI compared to other eddy current correction methods:

1. It does not need individual measurements and assumptions as in the post-processing methods.

2. It has extra flexibility in changing the diffusion gradient waveform than the waveform changing method, which can be designed to have sensitivities with interested microstructures.

3. It is principally compatible with the methods in all categories. These methods will help VAT-PSF-EPI reduce distortion residual and make even higher sequence acceleration and b-value possible.

In the current phantom experiment, although the TE of VAT-PSF-EPI (77 ms) is shorter than TRSE ss-EPI (84 ms), it is still much longer than the Stejskal-Tanner ss-EPI (67 ms). This is because both long RF in VAT-PSF-EPI (excitation/refocusing RF 15 ms/15 ms) are used compared with the product ss-EPI sequences (excitation/refocusing RF 4.2/5.2 ms). An RF duration reduction scheme, which will be used *in vivo* imaging, is introduced in the chapter on RF optimization.

To summarize the third assessment, eddy current distortion correction, 5-shot VAT-PSF-EPI evaluated qualitatively and quantitively the effectiveness of eddy current correction in a phantom experiment. It does not need an additional correction process for the eddy current induced by diffusion gradient up to b = 3000 s/mm^2 in a whole body 7 T human scanner.

3.4.5 High Resolution *in vivo* dMRI

The proposed VAT-PSF-EPI is tested for the high-resolution diffusion MRI *in vivo* and compared with the established distortion correction methods in this section. The results showed good correction of tissue-air susceptibility and eddy current distortion at 7 T.

The post-processing distortion correction methods mainly used the acquired reference data to calculate the uncorrected data. For example, multiple phase-encoding directions are needed as the topup in the susceptibility-induced distortion correction algorithm [92]. These methods are limited when the field deviations are significant due to high resolution, limited in-place parallel imaging factors, or large susceptibility difference areas. Further, with the common registering method for eddy current correction, register the images to either the B_0 or virtual undistorted DWI. The methods, however, are limited due to the contrast change of DWI or require many reference data with different directions (> 30) with whole q-space to make the methods work better. Further, the post-processing methods cannot differentiate the dynamic distortion from motion or phase-encoding artifacts, leading to potential correction errors. In general, the post-processing methods must make the image masking very accurate to reduce the calculation errors and processing times. These methods work better for the off-resonance effects that are small enough.

For distortion reduction sequences like rs-EPI, image distortion is reduced via segmenting

the k-space, thus decreasing the echo spacing. However, the reduction is limited. For example, the rs-EPI can reduce the echo spacing to a minimum of 0.32 ms via an increased number of segments. The echo spacing reduction in the current gradient system is roughly 0.068 ms per segment from two scanned imaging protocols. The echo spacing of rs-EPI was further decreased via in-plane parallel imaging. With the GRAPPA 4, the effective echo spacing is 0.08 ms or phase-encoding bandwidth of 78 Hz/px. As a result, the image displacement is still visible for typically 250 - 300 Hz of high off-resonance regions from susceptibility difference at 7 T. Regarding the eddy current distortion, the signal variation crossing different diffusion directions was visible and not reduced much compared to the ss-EPI (not shown). Further study needs to be done via the phantom study, which differs from the current study's subject.

The proposed VAT-PSF-EPI can also be seen as a multi-shot CSE method. The VAT-EPI data calculated the highly accelerated CSE with the missing data. It enables a higher PSF acceleration factor than PSF-EPI because the VAT-EPI data is more similar to the CSE than EPI. It benefits from the optimal VAT gradient suppressed by the off-resonance effects. In contrast, the acceleration of PSF-EPI can only be greater when the off-resonance effects are reduced. For example, such higher accelerations may be achieved for imaging at lower magnetic fields, using additional eddy current corrections, scanning with higher in-plane parallel imaging, or a higher performance gradient scanner. The first two conditions' benefit to VAT-PSF-EPI is less than PSF-EPI, while the latter can also benefit VAT-PSF-EPI. The acceleration of VAT-PSF-EPI relies on the off-resonance suppression of VAT and the generated image blurring. This study proved that VAT suppresses the in-plane off-resonance well, while the PSF mapping corrects the VAT image blurring well.

The sensitivity of PSF-EPI to the off-resonance effects is between CSE and EPI. This is because the CSE has only the spin-wrap phase encoding gradient, thus insensitive to the off-resonance effects, while the echo train in EPI is very sensitive to the off-resonance effects. Even with manipulating k-space trajectories (k_{y}, k_{y1}), these methods still need extra efforts to correct the eddy current distortion and chemical shift if high acceleration is requested. Thus, the term "distortion-free" may not be proper. In contrast, the VAT-EPI readout, as previously studied, was able to correct the susceptibility and chemical shift at 3 T. However, the study concluded that the method cannot be used for high-resolution imaging due to the image blurring. The current study proves that the lock of resolution is released even at 7 T, which has the scaled higher static off-resonance effects.

The limitations of the current methods are the SNR reduction and through-plane artifacts. The decrease in SNR comes from two factors: high VAT gradient amplitude and longer TE. The magnitude modulation from the high VAT gradient is partially mitigated by cutting low signal data to reduce the EPI phase-encoding resolution. Nevertheless, the SNR is still lower than signal averaged ss-EPI and rs-EPI in a similar scan time. Further,

the long TE is due to using long RF pulses (15 ms) to keep the VAT feasible. In future work applying the multiband method, the RF pulse, primarily refocusing, needs an intrinsically long duration to reduce SAR. The TE difference from ss-EPI to the proposed method will be reduced in such circumstances. The through-plane artifacts are due to the use of lower RF bandwidth. However, the slight through-plane distortion may be confounded with the pathological signal change. These could be mitigated via more sophisticated RF pulses in future work. The current study uses simple Sinc pulses to prove the concept.

3.4.6 Limitation 1 - SNR Reduction in VAT-PSF-EPI

The SNR change with R_{res} (or effectively the EPI phase encoding resolution reduction) in the PSF-EPI sequences is evaluated for the first time. It was used simply for the TE reduction [93, 107]. However, it may not be intuitive that the data SNR is boosting by discarding the data in addition to the TE reduction. This SNR increase happens mainly in the VAT-PSF-EPI and in PSF-EPI only with certain circumstances. However, the R_{res} factor is related to the maximum R_{PSF} because the PSF range increases with R_{res}. It needs to be consciously used.

In PSF-EPI sequences, the SNR change by using different R_{res} factors can be understood from the signal modulation function. In PSF-EPI, the data at boundaries has a relatively low signal due to T_2* decay alone EPI phase encoding. So, a small amount of signal discards leads to the SNR increase in the final image, especially for the lower GRAPPA factors. Also, the signal decreases in GRAPPA 4 from the starting low R_{res} of 2. Both can be explained by the fact that the T_2* decay in high GRAPPA factors is lower than in low GRAPPA factors. At the same time, the noise increases when the data is discarded. Assuming the background noise equally contributes from each EPI phase encoding data (image), the SNR increase due to R_{res} will be balanced when the signal becomes high toward the k-space center.

The same observation can be applied to the VAT-PSF-EPI data. Due to the strong VAT gradient, the signal decay alone EPI phase encoding is much sharper than pure T_2* decay. Therefore, the SNR of the magnitude summed image is lower than PSF-EPI with the same R_{PSF}. In other words, the magnitude summation can be seen as the area under the signal modulation function. Discarding those pure noisy data points at boundaries leads to an increase in the SNR very effectively. The SNR increase stopped immediately when the data signal became high, as in the PSF-EPI data left to the boundaries. Without using the R_{res}, the SNR compared to PSF-EPI is from one-third to half, making the sequence impractical. With the R_{res} factor of 10, the SNR of VAT-PSF-EPI increases by 1.9 to 2.4 folds.

A trade-off when using R_{res} is that the PSF range also increases with the R_{res} factor increase. The current thesis focuses on the acceleration of sequence, which may not be realistic by using a high R_{res} of 10 and making a lower available R_{PSF}. For the optimization

order of R_{PSF} and then R_{res}, the SNR of VAT-PSF-EPI is 61 % compared to the PSF-EPI when R_{PSF} is 1. With the application of maximum R_{PSF}, the SNR efficacy of VAT-PSF-EPI to PSF-EPI is 2.2, 2.1, and 1.4, corresponding to the GRAPPA 1, 2, and 4.

In summary, the SNR reduction of VAT-PSF-EPI is theoretically derived and verified with the phantom data. In addition, the proof of concept of the SNR increase method is demonstrated. Different RF pulse shapes may increase the SNR further in future work, similar to the blurring reduction in VAT-EPI.

3.4.7 Limitation 2 - Artifacts in VAT-PSF-EPI

The current subsection aims to discern the fat and oil ghosting artifacts in the accelerated VAT-PSF-EP images. However, separating these effects from the final VAT-PSF-EP images is challenging because the artifacts from PSF over-accelerating, EPI Nyquist ghost, and motion artifacts are always companions. Whenever the in-plane parallel imaging is used, the Nyquist ghost in the EPI images is no longer at the nominal 1/2 FoV, 1/4 FoV, and so forth, making it even more challenging to recognize. Reconstructing additional VAT-EP images helps differentiate between over-accelerating and Nyquist ghosts. Test with the phantom image further excludes the motion artifact. The results infer that the ghosting came from the Nyquist ghost.

In the conventional usage of VAT, the same RF bandwidth in 90 and 180 is usually used, and the fat signal is completely refocused, making the fat signal extremely high. On the contrary, vendor EPI typically combines multiple fat suppression methods to reduce the fat signal. Therefore, the fat signal in the VAT-PSF-EPI is very bright in the DWI.

So far, there is no method for correcting the Nyquist ghost to the off-resonance chemical shift signal. The most used method to correct the Nyquist ghost is still the three-echo reference data with the EPI phase-encoding gradient off. It is also used in the current study. Advanced reconstruction methods may reduce the on-resonance Nyquist ghost as a future work.

3.4.8 Improved High Resolution *in vivo* dMRI

This subsection demonstrates the limitations and improvement of minor artifacts generated by the high-off resonance fat content in VAT-PSF-EPI. One of the primary limitations of the current proposed VAT-PSF-EPI is the fat artifact from Nyquist ghost and through-plane distortion, as demonstrated in this and previous sections. These artifacts may lead to the pathological confounding in human DWI with the water content. One possible solution is to design a sophisticated RF, which may be complicated for the optimized result. Another possible solution is not to refocus the high off-reference fat content. The method is compatible with the VAT-PSF-EPI to suppress both artifacts, confirming the artifact's sources. In addition, the TE can be reduced to increase the SNR. The TE contribution

from the RF (90°and 180°) by using the differencing RF method has a reduction of 17 % to keep the VAT-PSF-EPI acquisition SNR efficient. In addition, the R_{res} of factors of 1.33, 2, and 2.5 were used to mitigate the SNR reduction from the VAT gradient. According to Chapter 3.5.1, the total SNR is 61 %, 64 %, and 79 % of the PSF-EPI for the same ETL. This is because of the optimization order of the acceleration factor before the SNR. Nevertheless, the SNR efficacy (SNR per shot) is still expected to be higher than PSF-EPI.

Compared to previous PSF-EPI acquisitions at 3 T and 7 T whole-body human scanners in the literature, it was only possible with R_{PSF} 4 to 5, thus easily needing 5 to 6 minutes to acquire a DWI, especially when high-resolution diffusion imaging is desired. In the current approach, the acquisition time can be largely reduced because of the high R_{PSF} of 16 to 32, which leads to a scan time for acquiring one DWI in the 30 seconds to one-minute range.

In comparing the methods of manipulating k-t trajectories in PSF-EPI [117, 118], they demonstrated the high acceleration to correct the susceptibility-induced image distortion for less than 10 shots, mainly at 3 T. However, these methods require additional calibration data and time-consuming reconstruction. Moreover, these methods need extra approaches to correct the distortion sources other than the static susceptibility [81]. For example, distortion from eddy current and chemical shift must be handled carefully.

The current proposed VAT-PSF-EPI can correct the susceptibility distortion, eddy current distortion, and chemical shift without complicated modeling, calibration, or reconstruction, thus making it straightforward to reach high-resolution diffusion imaging. Nevertheless, the extra methods of distortion reduction, which work for the general PSF-EPI methods, will also work for VAT-PSF-EPI. It is because even though the VAT works excellently in correcting the in-plane distortion, there can be a tiny amount of residual, as demonstrated in the previous chapter. In the theory of VAT-PSF-EPI, the maximum acceleration factor is inversely proportional to the PSF range, which is the summation of PSF width and shift. Any method that reduces distortion or blurring in EPI will benefit the available imaging acceleration in VAT-PSF-EPI.

4 Conclusion and Outlook

This thesis addresses one of the most challenging at ultrahigh MRI by amalgamating two seemingly impractical methods— the time-consuming multi-shot PSF-EPI and the severely blurred VAT-EPI— to formulate a novel dMRI sequence, VAT-PSF-EPI. This innovative approach leverages the strengths of both methods, rendering VAT-PSF-EPI a fast, non-distortion, and non-blurring sequence. Compared to PSF-EPI, VAT-PSF-EPI demonstrates a remarkable capacity to achieve fourfold acceleration for correcting air-tissue susceptibility-induced distortion and fourteenfold acceleration for correcting fat-tissue chemical shift at 7 T with the compatible image fidelity to CTI. Compared to VAT-EPI, the severe blurring from the VAT gradient can be corrected for the first time. Notably, the study uncovers VAT's unprecedented capability to correct eddy current distortion induced by the fast switching of diffusion gradient, even at high values of up to 3000 s/mm^2 for EPI, in which the PSF-EPI has been proved to have limited correction capability with lower b-values (b $\leq$ 1000 s/mm^2) recently. It was shown that VAT-PSF-EPI can achieve fast, very high-resolution dMRI of 0.7 mm in 1 minute and very fast of 15 sec (5 shots) for high resolution 1.4 mm dMRI for one DW neuroimaging at the traditional 7 T human whole-body MRI scanner (70 mT/m, 200 T/m/s). The overall acceleration of VAT-PSF-EPI compared to the full sampled PSF-EPI is up to 170 ($R_{PSF} \times R_{PE} \times R_{res} = 32 \times 4 \times 1.33$). Two limitations were found during the study of initially posed challenges: SNR reduction and faint fat artifacts. They were effectively addressed through distinct methods, in which the SNR boosted more than twofold, and the artifacts were effectively suppressed. To date, no other EPI sequence, apart from VAT-PSF-EPI, can correct susceptibility distortion, chemical shift, eddy current, and severe blurring—such as that induced by VAT gradients—at ultrahigh fields without the extra complexity of corrections.

Before this study, ultrahigh field dMRI encountered several limitations, failing to fully harness the advantages of high signal and other benefits inherent in ultrahigh fields compared to most imaging modalities with current whole-body scanners. One of the primary impediments lies in image distortion from various sources, constituting a formidable obstacle. Despite these challenges, dMRI remains indispensable for clinical diagnosis and the investigation of (brain) microstructure, with no alternative modalities capable of replacing diffusion in MRI. The pursuit of high spatiotemporal resolution and elevated b-values in dMRI, though imperative, is hampered by the inherent trade-off wherein any manipulation in dMRI invariably diminishes the SNR, thereby intensifying

the challenges.

One of the most interesting future works is to apply the proposed method to the ultrahigh field scanner equipped with a high-performance gradient system. In the preliminary results, the 7 T scanner with a high-performance gradient (200 mT/m, 900 T/m/s) can reduce the TE by more than 15 ms for the high-resolution imaging (0.8 mm, b_{max} = 1000 s/mm^2) and more than 50 ms for the high b-value imaging (1.5 mm, b_{max} = 10000 s/mm^2). As a result, the SNR was calculated to be 2.76 fold higher than the traditional whole-body 7 T and 1.73 fold to the Connectome 3T scanner (300 mT/m, 200 T/m/s) to be able to acquire high resolution and high b-values dMRI. In addition, due to the higher available slew rate of the gradient system, the Tesp in EPI is expected to be reduced to less than half compared to the current scanner. As derived from the current thesis, the speed of VAT-PSF-EPI is inversely proportional to the Tesp. The proposed sequence will be able to speed up at least twofold by using the high-performance 7 T. As a result, future work should implement the VAT-PSF-EPI to such a scanner.

In order to further improve the proposed method, specific existing methods may be interesting to combine. The multiband MRI can reduce the TR/sec to increase the slice coverage, which was done as the author's preliminary work. To further improve the image resolution, the 3D or hybrid 2D-3D encoding (g-slider) may be interesting to incorporate. The methods that can reduce the PSF range can further accelerate the proposed method. For example, the field probe for measuring and correcting the Eddy current residual can make the proposed method faster because the correcting residual by VAT will be smaller. Alternatively, developing a new RF pulse for VAT (e.g., VERSE) may reduce the TE and VAT blurring to make the VAT-PSF-EPI higher SNR and faster. Last but not least, considering the validated capability of VAT in correcting eddy current-induced distortion, the multi-shot approach for VAT-PSF-EPI may transition to a single-shot multireference approach, eliminating less efficient magnitude summation signals.

Nomenclature

Physics Constants

γ	proton gyromagnetic ratio	2.675×10^{8} s^{-1} T^{-1}
$\hbar$	reduced Planck constant	1.055×10^{-34} J s
k	Boltzmann constant	1.381×10^{-23} J K^{-1}
μ_0	vacuum magnetic permeability	1.256×10^{-6} N A^{-2}
μ_g	Bohr magneton	9.274×10^{-24} J T^{-1}
μ_N	Nuclear magneton	5.051×10^{-27} J T^{-1}

Other Symbols

χ	volume magnetic susceptibility
ϵ	permittivity
μ	permeabilityy
ω	angular frequency
ρ	spin number density
b	diffusion b-value
B_0	amplitude of static field
B_1	amplitude of radio-frequency field
C	Curie constant
D	diffusion coefficient
g	amplitude of gradient field
H	magnetic field strength
J	total angular momentum quantum number
L	orbital angular momentum quantum number

M	magnetization
R	acceleration factor
S	spin quantum number
T	temperature
T_{esp}	echo spacing time

List of Acronyms

NMR nuclear magnetic resonance

MRI magnetic resonance imaging

dMRI diffusion magnetic resonance imaging

UHF ultrahigh fields

EPI echo planar imaging

VAT view-angle tilting

PSF point-spread function mapping

DTI diffusion tensor imaging

SNR signal-to-noise ratio

RF radio-frequency

TSE turbo spin echo

BW bandwidth

$\mathbf{T}_1$ longitudinal relaxation time

$\mathbf{T}_2$ transverse relaxation time

TR repetition time

TE echo time

$\mathbf{T}_2^*$ effective transverse relaxation time

BPP Bloembergen-Purcell-Pound

SBM Solomon-Bloembergen-Morgan

ppm parts per million

TMS Tetramethylsilane

BMS bulk magnetic susceptibility

CTI constant time imaging

SE spin echo

CSE conventional frequency-encoded spin-echo imaging

SPI single-point imaging

PI parallel imaging

FoV field of view

SENSE sensitivity encoding

GRAPPA generalized auto-calibrating partial parallel acquisition

ACS autocalibration signal

DWI diffusion-weighted images

CSF cerebrospinal fluid

ADC apparent diffusion coefficient

TrWI trace weighted image

MD mean diffusivity

FA fractional anisotropic

ETL echo train length

SAR specific absorption rate

ESP echo spacing

fMRI functional magnetic resonance imaging

BOLD blood-oxygen-level-dependent imaging

STE Stimulated echo

MLEV Malcolm-Levitt

TBP time-bandwidth product

FWTM full width at the tenth maximum

TRSE twice refocusing spin echo

Bibliography

[1] F. Bloch. Nuclear induction. *Physical Review*, 70:460–474, 10 1946.

[2] Lars G. Hanson. Is quantum mechanics necessary for understanding magnetic resonance? *Concepts in Magnetic Resonance Part A: Bridging Education and Research*, 32:329–340, 9 2008.

[3] Robert W. Brown, Y C N Cheng, E. Mark. Haacke, Michael R. Thompson, and Ramesh. Venkatesan. *Magnetic Resonance Imaging: Physical Properties and Sequence Design*. Wiley, 2014.

[4] W A Edelstein, G H Glover, C J Hardy, and R W Redington. The intrinsic signal-to-noise ratio in nmr imaging, 1986.

[5] Marinus T. Vlaardingerbroek and Jacques A. den Boer. *Magnetic Resonance Imaging*. Springer Berlin Heidelberg, 2003.

[6] Rolf Pohmann, Oliver Speck, and Klaus Scheffler. Signal-to-noise ratio and mr tissue parameters in human brain imaging at 3, 7, and 9.4 tesla using current receive coil arrays. *Magnetic Resonance in Medicine*, 75:801–809, 2 2016.

[7] Florian Wiesinger, Peter Boesiger, and Klaas P. Pruessmann. Electrodynamics and ultimate snr in parallel mr imaging. *Magnetic Resonance in Medicine*, 52:376–390, 2004.

[8] N. Bloembergen, E. M. Purcell, and R. V. Pound. Relaxation effects in nuclear magnetic resonance absorption. *Physical Review*, 73:679–712, 4 1948.

[9] I. Solomon. Relaxation processes in a system of two spins. *Physical Review*, 99:559–565, 7 1955.

[10] N. Bloembergen and L. O. Morgan. Proton relaxation times in paramagnetic solutions. effects of electron spin relaxation. *The Journal of Chemical Physics*, 34:842–850, 1961.

[11] G. Held, F. Noack, V. Pollak, and B. Melton. Protonenspinrelaxation und wasserbeweglichkeit in muskelgewebe / proton spin relaxation and mobility of water in muscle tissue. *Zeitschrift für Naturforschung C*, 28:59–62, 2 1973.

[12] Robin A. de Graaf. *In Vivo NMR Spectroscopy*. Wiley, 10 2007.

[13] Robin A. De Graaf, Peter B. Brown, Scott McIntyre, Terence W. Nixon, Kevin L. Behar, and Douglas L. Rothman. High magnetic field water and metabolite proton t1 and t 2 relaxation in rat brain in vivo. *Magnetic Resonance in Medicine*, 56:386–394, 2006.

[14] Shalom Michaeli, Michael Garwood, Xiao Hong Zhu, Lance Delabarre, Peter Andersen, Gregor Adriany, Hellmut Merkle, Kamil Ugurbil, and Wei Chen. Proton t2 relaxation study of water, n-acetylaspartate, and creatine in human brain using hahn and carr-purcell spin echoes at 4t and 7t. *Magnetic Resonance in Medicine*, 47:629–633, 2002.

[15] Stanislav Motyka, Philipp Moser, Lukas Hingerl, Gilbert Hangel, Eva Heckova, Bernhard Strasser, Korbinian Eckstein, Simon Daniel Robinson, Benedikt A. Poser, Stephan Gruber, Siegfried Trattnig, and Wolfgang Bogner. The influence of spatial resolution on the spectral quality and quantification accuracy of whole-brain mrsi at 1.5t, 3t, 7t, and 9.4t. *Magnetic Resonance in Medicine*, 82:551–565, 8 2019.

[16] Robert G. Bryant, Keith Marill, Craig Blackmore, and C. Francis. Magnetic relaxation in blood and blood clots. *Magnetic Resonance in Medicine*, 13:133–144, 1 1990.

[17] Jean Pierre Korb and Robert G. Bryant. Magnetic field dependence of proton spin-lattice relaxation times. *Magnetic Resonance in Medicine*, 48:21–26, 2002.

[18] Paul A. Bottomley, Thomas H. Foster, Raymond E. Argersinger, and Leah M. Pfeifer. A review of normal tissue hydrogen nmr relaxation times and relaxation mechanisms from 1-100 mhz: Dependence on tissue type, nmr frequency, temperature, species, excision, and age. *Medical Physics*, 11:425–448, 1984.

[19] William D. Rooney, Glyn Johnson, Xin Li, Eric R. Cohen, Seong Gi Kim, Kamil Ugurbil, and Charles S. Springer. Magnetic field and tissue dependencies of human brain longitudinal 1h2o relaxation in vivo. *Magnetic Resonance in Medicine*, 57:308–318, 2007.

[20] Andreas Deistung, Alexander Rauscher, Jan Sedlacik, Jörg Stadler, Stephan Witoszynskyj, and Jürgen R. Reichenbach. Susceptibility weighted imaging at ultra high magnetic field strengths: Theoretical considerations and experimental results. *Magnetic Resonance in Medicine*, 60:1155–1168, 2008.

[21] Adrienne E. Campbell-Washburn, Rajiv Ramasawmy, Matthew C. Restivo, Ipshita Bhattacharya, Burcu Basar, Daniel A. Herzka, Michael S. Hansen, Toby Rogers, W. Patricia Bandettini, Delaney R. McGuirt, Christine Mancini, David Grodzki, Rainer Schneider, Waqas Majeed, Himanshu Bhat, Hui Xue, Joel Moss, Ashkan A.

Malayeri, Elizabeth C. Jones, Alan P. Koretsky, Peter Kellman, Marcus Y. Chen, Robert J. Lederman, and Robert S. Balaban. Opportunities in interventional and diagnostic imaging by using high-performance low-field-strength mri. *Radiology*, 293:384–393, 2019.

[22] Norman F. Ramsey. Magnetic shielding of nuclei in molecules. *Physical Review*, 78:699–703, 6 1950.

[23] Peter J. Mohr and Barry N. Taylor. Codata recommended values of the fundamental physical constants: 1998. *Reviews of Modern Physics*, 72:351–495, 4 2000.

[24] Xiang Fei, V.W. Hughes, and Ralf Prigl. Precision measurement of the magnetic field in terms of the free-proton nmr frequency. *Nuclear Instruments and Methods in Physics Research Section A: Accelerators, Spectrometers, Detectors and Associated Equipment*, 394:349–356, 7 1997.

[25] Robin K. Harris, Edwin D. Becker, Sonia M. Cabral De Menezes, Pierre Granger, Roy E. Hoffman, and Kurt W. Zilm. Further conventions for nmr shielding and chemical shifts (iupac recommendations 2008), 2008.

[26] George Van Dyke Tiers. Reliable proton nuclear resonance shielding values by "internal referencing" with tetramethyl-silane. *The Journal of Physical Chemistry*, 62:1151–1152, 9 1958.

[27] Rares Salomir, Baudouin Denis De Senneville, and Chrit T.W. Moonen. A fast calculation method for magnetic field inhomogeneity due to an arbitrary distribution of bulk susceptibility. *Concepts in Magnetic Resonance Part B: Magnetic Resonance Engineering*, 19:26–34, 10 2003.

[28] Duane A. Yoder, Yansong Zhao, Cynthia B. Paschal, and J. Michael Fitzpatrick. Mri simulator with object-specific field map calculations. *Magnetic Resonance Imaging*, 22:315–328, 4 2004.

[29] Chunlei Liu. Susceptibility tensor imaging. *Magnetic Resonance in Medicine*, 63:1471–1477, 2010.

[30] N. Li. Magnetic susceptibility quantification for arbitrarily shaped objects in inhomogeneous fields. *Magnetic Resonance in Medicine*, 46:907–916, 2001.

[31] John F. Schenck. The role of magnetic susceptibility in magnetic resonance imaging: Mri magnetic compatibility of the first and second kinds. *Medical Physics*, 23:815–850, 1996.

[32] David P. Jackson. Dancing paperclips and the geometric influence on magnetization: A surprising result. *American Journal of Physics*, 74:272–279, 4 2006.

[33] J. A. Osborn. Demagnetizing factors of the general ellipsoid. *Physical Review*, 67:351–357, 6 1945.

[34] C. J. Durrant, M. P. Hertzberg, and P. W. Kuchel. Magnetic susceptibility: Further insights into macroscopic and microscopic fields and the sphere of lorentz. *Concepts in Magnetic Resonance Part A: Bridging Education and Research*, 18:72–95, 5 2003.

[35] M. Garcia Morin, Grover Paulett, and Marcus E. Hobbs. Nuclear magnetic resonance chemical shift determinations by means of a concentric cylinder sample cell. *The Journal of Physical Chemistry*, 60:1594–1596, 11 1956.

[36] J. R. Zimmerman and M. R. Foster. Standardization of n.m.r. high resolution spectra. *The Journal of Physical Chemistry*, 61:282–289, 3 1957.

[37] Ksimon -.C. Chu, Yan Xu, James A. Balschi, and Charles S. Springer. Bulk magnetic susceptibility shifts in nmr studies of compartmentalized samples: use of paramagnetic reagents. *Magnetic Resonance in Medicine*, 13:239–262, 2 1990.

[38] Charles S. Springer. *Physicochemical Principles Influencing Magnetopharmaceuticals*, pages 75–99. Elsevier, 1994.

[39] T. Albahri, A. Anastasi, K. Badgley, S. Baeßler, I. Bailey, V. A. Baranov, E. Barlas-Yucel, T. Barrett, F. Bedeschi, M. Berz, M. Bhattacharya, H. P. Binney, P. Bloom, J. Bono, E. Bottalico, T. Bowcock, G. Cantatore, R. M. Carey, B. C.K. Casey, D. Cauz, R. Chakraborty, S. P. Chang, A. Chapelain, S. Charity, R. Chislett, J. Choi, Z. Chu, T. E. Chupp, A. Conway, S. Corrodi, L. Cotrozzi, J. D. Crnkovic, S. Dabagov, P. T. Debevec, S. Di Falco, P. Di Meo, G. Di Sciascio, R. Di Stefano, A. Driutti, V. N. Duginov, M. Eads, J. Esquivel, M. Farooq, R. Fatemi, C. Ferrari, M. Fertl, A. T. Fienberg, A. Fioretti, D. Flay, N. S. Froemming, C. Gabbanini, M. D. Galati, S. Ganguly, A. Garcia, J. George, L. K. Gibbons, A. Gioiosa, K. L. Giovanetti, P. Girotti, W. Gohn, T. Gorringe, J. Grange, S. Grant, F. Gray, S. Haciomeroglu, T. Halewood-Leagas, D. Hampai, F. Han, J. Hempstead, A. T. Herrod, D. W. Hertzog, G. Hesketh, A. Hibbert, Z. Hodge, J. L. Holzbauer, K. W. Hong, R. Hong, M. Iacovacci, M. Incagli, P. Kammel, M. Kargiantoulakis, M. Karuza, J. Kaspar, D. Kawall, L. Kelton, A. Keshavarzi, D. Kessler, K. S. Khaw, Z. Khechadoorian, N. V. Khomutov, B. Kiburg, M. Kiburg, O. Kim, Y. I. Kim, B. King, N. Kinnaird, E. Kraegeloh, N. A. Kuchinskiy, K. R. Labe, J. Labounty, M. Lancaster, M. J. Lee, S. Lee, B. Li, D. Li, L. Li, I. Logashenko, A. Lorente Campos, A. Lucà, G. Lukicov, A. Lusiani, A. L. Lyon, B. Maccoy, R. Madrak, K. Makino, F. Marignetti, S. Mastroianni, J. P. Miller, S. Miozzi, W. M. Morse, J. Mott, A. Nath, H. Nguyen, R. Osofsky, S. Park, G. Pauletta, G. M. Piacentino, R. N. Pilato, K. T. Pitts, B. Plaster, D. Počanić, N. Pohlman, C. C. Polly, J. Price, B. Quinn, N. Raha,

S. Ramachandran, E. Ramberg, J. L. Ritchie, B. L. Roberts, D. L. Rubin, L. Santi, C. Schlesier, A. Schreckenberger, Y. K. Semertzidis, D. Shemyakin, M. W. Smith, M. Sorbara, D. Stöckinger, J. Stapleton, C. Stoughton, D. Stratakis, T. Stuttard, H. E. Swanson, G. Sweetmore, D. A. Sweigart, M. J. Syphers, D. A. Tarazona, T. Teubner, A. E. Tewsley-Booth, K. Thomson, V. Tishchenko, N. H. Tran, W. Turner, E. Valetov, D. Vasilkova, G. Venanzoni, T. Walton, A. Weisskopf, L. Welty-Rieger, P. Winter, A. Wolski, and W. Wu. Magnetic-field measurement and analysis for the muon g-2 experiment at fermilab. *Physical Review A*, 103, 4 2021.

[40] Matt A Bernstein, Kevin F King, Xiaohong Joe Zhou, and Amsterdam Boston Heidelberg London New York Oxford Paris San Diego San Francisco Singapore Sydney Tokyo. *Handbook of MRI Pulse Sequences*. Elsevier, 2004.

[41] Timothy G. Reese, O. Heid, R. M. Weisskoff, and V. J. Wedeen. Reduction of eddy-current-induced distortion in diffusion mri using a twice-refocused spin echo. *Magnetic Resonance in Medicine*, 49:177–182, 1 2003.

[42] Nils Kickler, Wietske Van Der Zwaag, Ralf Mekle, Tobias Kober, Jose P. Marques, Gunnar Krueger, and Rolf Gruetter. Eddy current effects on a clinical 7t-68 cm bore scanner. *Magnetic Resonance Materials in Physics, Biology and Medicine*, 23:39–43, 2 2010.

[43] Peter Jezzard, Alan S. Barnett, and Carlo Pierpaoli. Characterization of and correction for eddy current artifacts in echo planar diffusion imaging. *Magnetic Resonance in Medicine*, 39:801–812, 1998.

[44] S. Gravina and D.G. Cory. Sensitivity and resolution of constant-time imaging. *Journal of Magnetic Resonance, Series B*, 104:53–61, 5 1994.

[45] E. L. Hahn. Spin echoes. *Physical Review*, 80:580–594, 11 1950.

[46] Michael K. Stehling, Robert Turner, and Peter Mansfield. Echo-planar imaging: Magnetic resonance imaging in a fraction of a second. *Science*, 254:43–50, 10 1991.

[47] Sankaran Subramanian, Nallathamby Devasahayam, Ramachandran Murugesan, Kenichi Yamada, John Cook, Andrew Taube, James B. Mitchell, Joost A.B. Lohman, and Murali C. Krishna. Single-point (constant-time) imaging in radiofrequency fourier transform electron paramagnetic resonance. *Magnetic Resonance in Medicine*, 48:370–379, 2002.

[48] Klaas P. Pruessmann, Markus Weiger, Markus B. Scheidegger, and Peter Boesiger. Sense: Sensitivity encoding for fast mri. *Magnetic Resonance in Medicine*, 42:952–962, 1999.

[49] Mark A. Griswold, Peter M. Jakob, Robin M. Heidemann, Mathias Nittka, Vladimir Jellus, Jianmin Wang, Berthold Kiefer, and Axel Haase. Generalized autocalibrating partially parallel acquisitions (grappa). *Magnetic Resonance in Medicine*, 47:1202–1210, 2002.

[50] Bastien Guérin, Jorge F. Villena, Athanasios G. Polimeridis, Elfar Adalsteinsson, Luca Daniel, Jacob K. White, and Lawrence L. Wald. The ultimate signal-to-noise ratio in realistic body models. *Magnetic Resonance in Medicine*, 78:1969–1980, 11 2017.

[51] Adolph Fick. V. on liquid diffusion. *The London, Edinburgh, and Dublin Philosophical Magazine and Journal of Science*, 10:30–39, 7 1855.

[52] George Gabriel Stokes. *On the Effect of the Internal Friction of Fluids on the Motion of Pendulums*, volume 3, pages 1–10. Cambridge University Press, 7 1850.

[53] A. Einstein. Über die von der molekularkinetischen theorie der wärme geforderte bewegung von in ruhenden flüssigkeiten suspendierten teilchen. *Annalen der Physik*, 322:549–560, 1905.

[54] M. Holz, S. R. Heil, and A. Sacco. Temperature-dependent self-diffusion coefficients of water and six selected molecular liquids for calibration in accurate 1h nmr pfg measurements. *Physical Chemistry Chemical Physics*, 2:4740–4742, 10 2000.

[55] H. C. Torrey. Bloch equations with diffusion terms. *Physical Review*, 104:563–565, 11 1956.

[56] E. O. Stejskal and J. E. Tanner. Spin diffusion measurements: Spin echoes in the presence of a time-dependent field gradient. *The Journal of Chemical Physics*, 42:288–292, 1965.

[57] D Le Bihan, E Breton, D Lallemand, P Grenier, E Cabanis, and M Laval-Jeantet. Mr imaging of intravoxel incoherent motions: application to diffusion and perfusion in neurologic disorders. *Radiology*, 161:401–407, 11 1986.

[58] Davy Sinnaeve. The stejskal-tanner equation generalized for any gradient shape-an overview of most pulse sequences measuring free diffusion. *Concepts in Magnetic Resonance Part A: Bridging Education and Research*, 40 A:39–65, 3 2012.

[59] Michael A Boss, Kathryn E (orcid)0000 0001-9070-5255 Keenan, Karl F (orcid)0000 0001-8356-1660 Stupic, Nikki S Rentz, Cassandra M Stoffer, Stephen E (orcid)0000 0002-8788-2442 Russek, Amanda A (orcid)0000 0001-9515-0383 Koepke, and Kevin J (orcid)0000 0003-3787-2577 Coakley. Magnetic resonance imaging biomarker calibration service :, 10 2022.

[60] P.J. Basser, J. Mattiello, and D. Lebihan. Estimation of the effective self-diffusion tensor from the nmr spin echo. *Journal of Magnetic Resonance, Series B*, 103:247–254, 3 1994.

[61] Timothy E.J. Behrens, M. W. Woolrich, Mi Jenkinson, H. Johansen-Berg, R. G. Nunes, S. Clare, P. M. Matthews, J. M. Brady, and S. M. Smith. Characterization and propagation of uncertainty in diffusion-weighted mr imaging. *Magnetic Resonance in Medicine*, 50:1077–1088, 2003.

[62] Carlo Pierpaoli and Peter J. Basser. Toward a quantitative assessment of diffusion anisotropy. *Magnetic Resonance in Medicine*, 36:893–906, 1996.

[63] Sinisa Pajevic and Carlo Pierpaoli. Color schemes to represent the orientation of anisotropic tissues from diffusion tensor data: Application to white matter fiber tract mapping in the human brain. *Magnetic Resonance in Medicine*, 42:526–540, 1999.

[64] Jens H. Jensen, Joseph A. Helpern, Anita Ramani, Hanzhang Lu, and Kyle Kaczynski. Diffusional kurtosis imaging: The quantification of non-gaussian water diffusion by means of magnetic resonance imaging. *Magnetic Resonance in Medicine*, 53:1432–1440, 2005.

[65] Mami Iima, Tomomi Nobashi, Hirohiko Imai, Sho Koyasu, Tsuneo Saga, Yuji Nakamoto, Masako Kataoka, Akira Yamamoto, Tetsuya Matsuda, and Kaori Togashi. Effects of diffusion time on non-gaussian diffusion and intravoxel incoherent motion (ivim) mri parameters in breast cancer and hepatocellular carcinoma xenograft models. *Acta Radiologica Open*, 7:205846011775156, 1 2018.

[66] P Mansfield. Multi-planar image formation using nmr spin echoes. *Journal of Physics C: Solid State Physics*, 10:L55–L58, 2 1977.

[67] R Rzedzian, P Mansfield, M Doyle, D Guilfoyle, B Chapman, R.E Coupland, A Chrispin, and P Small. Real-time nuclear magnetic resonance clinical imaging in paediatrics. *The Lancet*, 322:1281–1282, 12 1983.

[68] J. Hennig, A. Nauerth, and H. Friedburg. Rare imaging: A fast imaging method for clinical mr. *Magnetic Resonance in Medicine*, 3:823–833, 12 1986.

[69] H. Y. Carr and E. M. Purcell. Effects of diffusion on free precession in nuclear magnetic resonance experiments. *Physical Review*, 94:630–638, 5 1954.

[70] S. Meiboom and D. Gill. Modified spin-echo method for measuring nuclear relaxation times. *Review of Scientific Instruments*, 29:688–691, 1958.

[71] Juergen Hennig and Klaus Scheffler. Hyperechoes. *Magnetic Resonance in Medicine*, 46:6–12, 2001.

[72] A. Kangarlu, A. M. Abduljalil, C. Schwarzbauer, D. G. Norris, and P. M. L. Robitaille. Human rapid acquisition with relaxation enhancement imaging at 8 t without specific absorption rate violation. *Magma: Magnetic Resonance Materials in Physics, Biology, and Medicine*, 9:81–84, 10 1999.

[73] Ikuhiro Kida, Takashi Ueguchi, Yuichiro Matsuoka, Kun Zhou, Alto Stemmer, and David Porter. Comparison of diffusion-weighted imaging in the human brain using readout-segmented epi and propeller turbo spin echo with single-shot epi at 7 t mri. *Investigative Radiology*, 51:435–439, 7 2016.

[74] P. S. Melki and R. V. Mulkern. Magnetization transfer effects in multislice rare sequences, 1992.

[75] Yongquan Ye, Yan Zhuo, Rong Xue, and Xiaohong Joe Zhou. Bold fmri using a modified haste sequence. *NeuroImage*, 49:457–466, 1 2010.

[76] Eric E. Sigmund and David Gutman. Diffusion-weighted imaging of the brain at 7 t with echo-planar and turbo spin echo sequences: Preliminary results. *Magnetic Resonance Imaging*, 29:752–765, 7 2011.

[77] Fabian Hilbert, Tobias Wech, Henning Neubauer, Simon Veldhoen, Thorsten Alexander Bley, and Herbert Köstler. Vergleich von turbo spin echo und echoplanar bildgebung für intravoxel incoherent motion und diffusionstensorbildgebung der niere bei 3 tesla. *Zeitschrift fur Medizinische Physik*, 27:193–201, 2017.

[78] David C. Alsop. Phase insensitive preparation of single-shot rare: Application to diffusion imaging in humans. *Magnetic Resonance in Medicine*, 38:527–533, 1997.

[79] Fritz Schick. Splice: Sub-second diffusion-sensitive mr imaging using a modified fast spin-echo acquisition mode. *Magnetic Resonance in Medicine*, 38:638–644, 1997.

[80] Patrick Le Roux. Non-cpmg fast spin echo with full signal. *Journal of Magnetic Resonance*, 155:278–292, 2002.

[81] Philip K. Lee and Brian A. Hargreaves. A joint linear reconstruction for multishot diffusion weighted non-carr-purcell-meiboom-gill fast spin echo with full signal. *Magnetic Resonance in Medicine*, 88:2139–2156, 11 2022.

[82] João dos Santos Periquito, Katharina Paul, Till Huelnhagen, Min Chi Ku, Yiyi Ji, Kathleen Cantow, Thomas Gladytz, Dirk Grosenick, Bert Flemming, Erdmann

Seeliger, Sonia Waiczies, Thoralf Niendorf, and Andreas Pohlmann. Diffusion-weighted renal mri at 9.4 tesla using rare to improve anatomical integrity. *Scientific Reports*, 9, 12 2019.

[83] M. Wiesmueller, W. Wuest, M. S. May, S. Ellmann, R. Heiss, M. Saake, R. Janka, M. Uder, and F. B. Laun. Comparison of readout-segmented echo-planar imaging and single-shot tse dwi for cholesteatoma diagnostics, 7 2021.

[84] James G. Pipe. Motion correction with propeller mri: Application to head motion and free-breathing cardiac imaging. *Magnetic Resonance in Medicine*, 42:963–969, 11 1999.

[85] James G. Pipe, Victoria G. Farthing, and Kirsten P. Forbes. Multishot diffusion-weighted fse using propeller mri. *Magnetic Resonance in Medicine*, 47:42–52, 2002.

[86] James G. Pipe and Nicholas Zwart. Turboprop: Improved propeller imaging. *Magnetic Resonance in Medicine*, 55:380–385, 2006.

[87] Zhiqiang Li, James G. Pipe, Chu Yu Lee, Josef P. Debbins, John P. Karis, and Donglai Huo. X-prop: A fast and robust diffusion-weighted propeller technique. *Magnetic Resonance in Medicine*, 66:341–347, 2011.

[88] John C. Gore Matthew D. Robson, Adam W. Anderson. Diffusion-weighted multiple shot echo planar imaging of humans without navigation. *Magnetic Resonance in Medicine*, 12 2005.

[89] Z. H. Cho, D. J. Kim, and Y. K. Kim. Total inhomogeneity correction including chemical shifts and susceptibility by view angle tilting. *Medical Physics*, 15:7–11, 1 1988.

[90] Sinyeob Ahn and Xiaoping P. Hu. View angle tilting echo planar imaging for distortion correction. *Magnetic Resonance in Medicine*, 68:1211–1219, 2012.

[91] Peter Jezzard and Robert S. Balaban. Correction for geometric distortion in echo planar images from b0 field variations. *Magnetic Resonance in Medicine*, 07 1995.

[92] Jesper L.R. Andersson, Stefan Skare, and John Ashburner. How to correct susceptibility distortions in spin-echo echo-planar images: Application to diffusion tensor imaging. *NeuroImage*, 20:870–888, 10 2003.

[93] Huairen Zeng and R. Todd Constable. Image distortion correction in epi: Comparison of field mapping with point spread function mapping. *Magnetic Resonance in Medicine*, 48:137–146, 2002.

[94] Filippo Del Grande, Francesco Santini, Daniel A. Herzka, Michael R. Aro, Cooper W. Dean, Garry E. Gold, and John A. Carrino. Fat-suppression techniques for 3-t mr imaging of the musculoskeletal system. *Radiographics*, 34:217–233, 1 2014.

[95] W T Dixon. Simple proton spectroscopic imaging. *Radiology*, 10 1984.

[96] Scott B. Reeder, Angel R. Pineda, Zhifei Wen, Ann Shimakawa, Huanzhou Yu, Jean H. Brittain, Garry E. Gold, Christopher H. Beaulieu, and Norbert J. Pelc. Iterative decomposition of water and fat with echo asymmetry and least-squares estimation (ideal): Application with fast spin-echo imaging. *Magnetic Resonance in Medicine*, 08 2005.

[97] Dimo Ivanov, Andreas Schäfer, Markus N. Streicher, Robin M. Heidemann, Robert Trampel, and Robert Turner. A simple low-sar technique for chemical-shift selection with high-field spin-echo imaging. *Magnetic Resonance in Medicine*, 64:319–326, 2010.

[98] C B Ahn and Z H Cho. Analysis of the eddy-current induced artifacts and the temporal compensation in nuclear magnetic resonance imaging, 1991.

[99] A. Trakic, F. Liu, H. Sanchez Lopez, H. Wang, and Stuart Crozier. Longitudinal gradient coil optimization in the presence of transient eddy currents. *Magnetic Resonance in Medicine*, 57:1119–1130, 2007.

[100] Dan Xu, Joseph K. Maier, Kevin F. King, Bruce D. Collick, Gaohong Wu, Robert D. Peters, and R. Scott Hinks. Prospective and retrospective high order eddy current mitigation for diffusion weighted echo planar imaging. *Magnetic Resonance in Medicine*, 70:1293–1305, 2013.

[101] Benjamin E. Dietrich, David O. Brunner, Bertram J. Wilm, Christoph BarmeT, Simon Gross, Lars Kasper, Maximilian Haeberlin, Thomas Schmid, S. Johanna Vannesjo, and Klaas P. Pruessmann. A field camera for mr sequence monitoring and system analysis. *Magnetic Resonance in Medicine*, 75:1831–1840, 4 2016.

[102] Matthew D. Robson, John C. Gore, and R. Todd Constable. Measurement of the point spread function in mri using constant time imaging. *Magnetic Resonance in Medicine*, 38:733–740, 1997.

[103] M. Zaitsev, J. Hennig, and O. Speck. Point spread function mapping with parallel imaging techniques and high acceleration factors: Fast, robust, and flexible method for echo-planar imaging distortion correction. *Magnetic Resonance in Medicine*, 52:1156–1166, 2004.

[104] Oliver Speck, J. Stadler, and M. Zaitsev. High resolution single-shot epi at 7t. *Magma: Magnetic Resonance Materials in Physics, Biology, and Medicine*, 11 2007.

[105] Andrew L. Alexander, Jay S. Tsuruda, and Dennis L. Parker. Elimination of eddy current artifacts in diffusion-weighted echo-planar images: The use of bipolar gradients. *Magnetic Resonance in Medicine*, 38:1016–1021, 1997.

[106] Kim Butts, John M. Pauly, and Garry E. Gold. Reduction of blurring in view angle tilting mri. *Magnetic Resonance in Medicine*, 53:418–424, 2005.

[107] Myung Ho In, Oleg Posnansky, and Oliver Speck. High-resolution distortion-free diffusion imaging using hybrid spin-warp and echo-planar psf-encoding approach. *NeuroImage*, 148:20–30, 3 2017.

[108] Myung-Ho In, Zijing Dong, Kawin Setsompop, Daehun Kang, Uten Yarach, Yunhong Shu, Joshua D Trzasko, John Huston, and Matt A Bernstein. An efficient reconstruction by combining tilted-caipi with eddy-current calibration. *Proc. Intl. Soc. Mag. Reson. Med. 27*, 2019.

[109] Oliver Heid. Eddy current-nulled diffusion weighting. *Proc. Intl. Sot. Mag. Reson. Med. 8*, 2000.

[110] M. Weigel, S. Schwenk, V. G. Kiselev, K. Scheffler, and J. Hennig. Extended phase graphs with anisotropic diffusion. *Journal of Magnetic Resonance*, 205:276–285, 2010.

[111] R. Z. Freidlin, J. W. Kakareka, T. J. Pohida, M. E. Komlosh, and P. J. Basser. A spin echo sequence with a single-sided bipolar diffusion gradient pulse to obtain snapshot diffusion weighted images in moving media. *Journal of Magnetic Resonance*, 221:24–31, 8 2012.

[112] Eric Aliotta, Kévin Moulin, and Daniel B. Ennis. Eddy current–nulled convex optimized diffusion encoding (en-code) for distortion-free diffusion tensor imaging with short echo times. *Magnetic Resonance in Medicine*, 79:663–672, 2 2018.

[113] Manoj Shrestha, Pavel Hok, Ulrike Nöth, Bianca Lienerth, and Ralf Deichmann. Optimization of diffusion-weighted single-refocused spin-echo epi by reducing eddy-current artifacts and shortening the echo time. *Magnetic Resonance Materials in Physics, Biology and Medicine*, 31:585–597, 10 2018.

[114] Jesper L.R. Andersson and Stamatios N. Sotiropoulos. An integrated approach to correction for off-resonance effects and subject movement in diffusion mr imaging. *NeuroImage*, 125:1063–1078, 1 2016.

[115] Haruyasu Yamada, Osamu Abe, Takashi Shizukuishi, Junko Kikuta, Takahiro Shinozaki, Ko Dezawa, Akira Nagano, Masayuki Matsuda, Hiroki Haradome, and Yoshiki Imamura. Efficacy of distortion correction on diffusion imaging: Comparison of fsl eddy and eddy-correct using 30 and 60 directions diffusion encoding. *PLoS ONE*, 9, 11 2014.

[116] Myung Ho In, Ek Tsoon Tan, Joshua D. Trzasko, Yunhong Shu, Daehun Kang, Uten Yarach, Shengzhen Tao, Erin M. Gray, John Huston, and Matt A. Bernstein. Distortion-free imaging: A double encoding method (diadem) combined with multiband imaging for rapid distortion-free high-resolution diffusion imaging on a compact 3t with high-performance gradients. *Journal of Magnetic Resonance Imaging*, 51:296–310, 1 2020.

[117] Zijing Dong, Fuyixue Wang, Timothy G. Reese, Mary Katherine Manhard, Berkin Bilgic, Lawrence L. Wald, Hua Guo, and Kawin Setsompop. Tilted-caipi for highly accelerated distortion-free epi with point spread function (psf) encoding. *Magnetic Resonance in Medicine*, 81:377–392, 1 2019.

[118] Fuyixue Wang, Zijing Dong, Timothy G. Reese, Berkin Bilgic, Mary Katherine Manhard, Jingyuan Chen, Jonathan R. Polimeni, Lawrence L. Wald, and Kawin Setsompop. Echo planar time-resolved imaging (epti). *Magnetic Resonance in Medicine*, 81:3599–3615, 6 2019.

A Dirac Delta Function

The Dirac delta function is defined as

$$\delta(x-a) = 0 \qquad \text{when } x \neq a \tag{A.1}$$

$$\int_{-\infty}^{+\infty} \delta(x-a)\,dx = 1 \tag{A.2}$$

Using the fact that the Fourier inversion of 1 is a delta function, together with three delta function properties, to derive the equations in the thesis body. The first property is the even symmetry

$$\delta(-x) = \delta(x) \tag{A.3}$$

The second is the sifting property, which is for any function f(x), the measurement of f(x) at the point a is

$$\int_{-\infty}^{+\infty} f(x)\delta(x-a)\,dx = f(a)\int_{-\infty}^{+\infty} f(x-a)\,dx = f(a) \tag{A.4}$$

The third is the convolution property (shifting property), which states that any function f(x) convolves with a shifted impulse function of the amount a δ(x-a) yields the shifted version of the original function f(x-a)

$$f(a) * \delta(x-a) = \int_{-\infty}^{+\infty} f(x-\lambda)\delta(x-a)\,d\lambda = f(x-a) \tag{A.5}$$

where λ is a dummy variable.